DOI: 10.51975/23380201.som
Journal of the Nigerian Society of Chemical Engineers, 38(2), 2023

PRODUCTION OPTIMIZATION OF A NIGERIAN OIL WELL

***Osunleke, A. S[1], Bamimore, A[1], Chukwunta, F[1], Sanni, N[1], Badmus, I.A.[2]**

[1]*Department of Chemical Engineering, Obafemi Awolowo University, Ile-Ife, Nigeria*
[2]*Department of Process and Operations, Dangote Petroleum Refinery and Petrochemicals FZE, Lagos*

[1 *]aosunlek@oauife.edu.ng, [1]abamimore@oauife.edu.ng, [1]cu9francis@gmail.com, [1]nafeesolaitan@gmail.com, [2]ibrahimabiolabadmus@yahoo.com
*Corresponding Author: aosunlek@oauife.edu.ng

ABSTRACT

There has been a constant growing demand for oil and gas over the last decades. However, there is a reduction in the discovery of large oil reservoir. Hence, the need to efficiently exploit existing ones. This study applied an optimization method to control undesired fluid production, increase the potential for greater oil recovery and predicting field performance, thus, enhancing reservoir profitability. An open-source reservoir simulator (MATLAB Reservoir Simulator Toolbox, MRST) was used to simulate and run production optimization for a real reservoir model considering different well placements. Three different well placement scenarios were considered with each scenario having multiple producer wells and either single or multiple injector wells. The performance criterion used for this work is water cut. For all scenarios considered, the well performance over a 10-year period was analysed. The profitability of each producer well in all the scenarios was found to depend on both its well placement and that of the injector wells. The volume and number of injector wells was also found to affect the volume of oil produced, and the profitability length. Scenario 1 with 1 injector well produced less oil but of greater profitability length. Scenarios 2 and 3 with three injector wells each had less profitability length but produced more oil than scenario 1 in 10 years.

Keywords: *Reservoir management; production optimization; Reservoir Simulation; well placement*

1. INTRODUCTION

Energy is playing a pivotal role in the prosperity of mankind and will in all probability continue to do so into the distant future. Worldwide economic growth is expected to be about 3% per year through 2030, a pace similar to the last 20 years and it is estimated that the energy demand will increase by 50% by the year 2030 (ExxonMobil Corporation, 2004). This undiminished growth in energy demand due to population growth, and increasing personal income, notably in developing countries, will accelerate the global demand for energy. The sustainability of our modern society depends crucially on a secure and accessible supply of energy, thus, the importance of energy to our modern world cannot be overemphasized.

Interestingly, oil and gas has been the predominant source satisfying almost 60% of the current energy demand worldwide. This percentage is expected to stay relatively stable in the future, at least to 2030 (ExxonMobil Corporation, 2004). Also, oil and gas have the advantages of being relatively more available, better performance, cheaper, and more convenient than any other sources. Hence, the need to maximally utilize this source of energy.

Unfortunately, most of the existing major oilfields are already at a mature stage, and the number of new significant discoveries per year is decreasing (Brouwer, 2004) and since oil is non-renewable, it will become increasingly harder to meet this ever-increasing demand for oil and gas. Although, smaller fields are still regularly found, but at the current oil price, it is often not economical to exploit them. As a direct result it becomes more and more difficult to maintain economic reserves at a desirable level. In order to satisfy the growing worldwide demand for oil and gas, it is becoming increasingly important to produce existing fields and new fields as efficiently as possible, while simultaneously decreasing development and operating costs (Najafiazar, 2014).

The current industry average for the recovery factor from an oil well is a meagre 35%, which is for reservoirs with favourable production conditions (Rossi, 2002). One possible way of improving production rate is through a wide array of techniques collectively termed “Production Optimization”.

The production optimization process is based on a sequence of activities that transform measured or collected data into optimal field management decisions. It is achieved by comparing measured data with predicted performance and executing a sequence of activities as iterative loops to ensure that the reservoir delivers to its maximum potential. Production optimization includes controlling wells in order to maximize (or minimize) some performance criteria. The ability to control wells provides the ability to control fluid flow behaviour within the reservoir, thereby enabling maximization or minimization of any criteria by which production performance can be measured.

This work seeks to determine the optimal reservoir production rate by optimising the net present value (NPV) of the reservoir. To achieve this, a water flooding method is used to control undesired fluid production and increase the potential for greater oil recovery thus enhance reservoir management and profitability. This is done by observing the profitability of different production wells at different locations in a field using water cut as the performance criterion.

2. RESERVOIR MODEL

The physical system to be modelled must be expressed in terms of appropriate mathematical equations. This process almost always involves assumptions. The assumptions are necessary from a practical standpoint in order to make the problem tractable (Najafiazar, 2014). In this work, the following simplifying assumptions are made in modelling the reservoir;

i. the flow of oil and water only through a heterogeneous porous medium is considered
ii. the reservoir is horizontal and of constant thickness
iii. the gravity and capillary forces are negligible.
iv. the reservoir is in its secondary recovery phase
v. the pressures are above the bubble point pressure of the oil phase.
vi. the fluids and rocks are incompressible, with no-flow boundaries, and are at isothermal conditions

Hence, there are two-phase immiscible flow (that is, no mass transfer between the two liquid phases).

The focus here is on water – flooding cases for a two-phase (oil and water) reservoir. To implement the reservoir model, MATLAB Reservoir Simulation Toolbox (MRST) was used.

MRST is developed by *SINTEF Applied Mathematics* and is a result of their research on the development of new (multiscale) computational methodologies. Version 2015a which was used in this study, is available online for free download under the terms of the GNU General Public License (GPL) (Lie *et al.,* 2012). The toolbox consists of two main parts: a core offering basic functionality and single and two-phase solvers, and a set of add-on modules offering more advanced models, viewers and solvers.

2.1 Reservoir Optimization

Reservoir production optimization is a complete or partial automation process for maximizing the development effect within the lifecycle of a reservoir by optimizing operational parameters (Hou *et al.,* 2015). Production optimization aims at achieving the best development performance for a given reservoir by optimizing well controls. In order to evaluate the performance of different development programs, various objectives have been proposed during the long research into production optimization. For example, Rosenwald & Green (1974) minimized the difference between the production-demand curve and the flow curve actually attained, Babayev (1975) provided minimum total cost per unit output; while Ladson *et al.* (1986)

i. maximized the deliverability of a gas reservoir at a specified time,
ii. minimized the total gas withdrawal shortfall between the demand schedule and the amount of gas that can actually be delivered in each month, and
iii. optimized the weighted combinations of the above two objectives.

When optimizing production strategies, one often encounters multiple local maxima. This phenomenon may be a good thing sometimes because it means that there are extra degrees of freedom in the optimization problem, which can be used to accomplish other optimization objectives. For instance, Van Essen *et al.* (2011) incorporated short-term goals into the life-cycle optimization problem and proposed a hierarchical production optimization structure with multiple objectives. Chen *et al.* (2012) also optimized both long-term and short-term net present value. As more and more oilfields enter the high water cut period, the production costs increase gradually. Therefore, the net present value is commonly selected as the objective function for production optimization.

According to Hou *et al.,* (2015), in order to find out under which operational parameters at current reservoir

conditions the oil production might be most efficient and profitable, automatic history matching and reservoir production optimization should be combined together.

3. MODEL DEVELOPMENT

To optimize a reservoir, a reservoir model needs to be developed. The system (reservoir) to be modelled must be expressed in terms of appropriate mathematical equations. This process almost always involves assumptions. The assumptions are necessary from a practical standpoint in order to make the problem tractable (Najafiazar, 2014). This follows two approaches: Subsurface flow modelling and then optimization of the process.

3.1 Subsurface Flow Modelling Through Porous Media

The mass balance for a porous medium domain of volume V with boundary $\partial\Omega$ of area s, for the conservation of some quantity c can be formulated as

$$\frac{\partial}{\partial t}\int c\, dV + \oint F.n\, ds = \int q\, dV \tag{1}$$

The continuity equation is obtained using the Gauss' divergence theorem

$$\frac{\partial c}{\partial t} + \nabla.F = q \tag{2}$$

Expressing Equation (2) in Darcy's law considering a two – phase (oil and water) fluid flow, the following were obtained

$$\frac{\partial(\rho_\alpha \phi S_\alpha)}{\partial t} + \nabla.(\rho_\alpha v_\alpha) = \widetilde{q_\alpha} \tag{3a}$$

$$v_\alpha = -\frac{k_{r\alpha}}{\mu_\alpha} K(\nabla p_\alpha - p_\alpha g \nabla d) \tag{3b}$$

Where K is the permeability tensor, μ is the fluid viscosity, k_r is the relative permeability, ρ is pressure, g is the acceleration of gravity and d is the depth. The ratio $\frac{k_{r\alpha}}{\mu_\alpha}$ is called the phase mobility represented as λ_α. Since, no gravity assumption was employed, Darcy's law becomes

$$v_\alpha = -\lambda_\alpha K \nabla p_\alpha \tag{4}$$

For two – phase flow, there are unknowns (*pw, po, Sw, So*), four equations are required to complete the system description and solve Equations (3a) and (3b). The two additional equations are given by a closure equation which states that the sum of all fractional saturations must always be equal to one, and the oil-water capillary pressure equation, which gives a relation between phase pressures as function of water saturation. They are respectively given as:

$$S_w + S_o = 1 \tag{5a}$$

$$p_o - p_w = p_c(S_w) \tag{5b}$$

Equations (1) to (5) can be rearranged in such a way that the two-phase equations are formulated in terms of two state variables: *po*, the oil pressure, and *Sw* the water saturation.

In order to do that, one can apply the chain rule differentiation and the definitions of oil, water and rock compressibility yielding

$$\phi \frac{\partial S}{\partial t} + \nabla. f_w(S) v = q_w \tag{6}$$

Equations (4) and (5) are called the pressure and saturation equations respectively. The pressure and saturation equations are referred to as the state equations. It is impossible to find an analytical solution of the state equations for typical reservoir models. Hence, one approximates the solutions by some numerical method (Aarnes *et al.*, 2007).

MRST applies a spatial discretization scheme based on finite differences using upstream weighting in the convection dominant terms. After discretization in space, each grid block is related to two states of the reservoir, that is oil pressures and water saturations. MRST implements an adjoint model consisting of a multi-scale pressure solver and a saturation solver which works on flow-adapted grids (Lie *et al.,* 2012). Each step of the discretized state equations can be written in a compact form as $F(x,u)$ as

$$F^n(x^n, x^{n-1}, u^n) \tag{7}$$

Introducing an auxiliary function J_α as

$$J_\alpha(x,u) = J(x,u) + \alpha^T F(x,u) \tag{8}$$

Where $J(x,u)$ is the objective function, $\nabla_u J$ the gradient of J with respect to u, $\alpha = \alpha(\alpha_v, \alpha_p, \alpha_s, \alpha_\pi)$ is a vector of Lagrange multipliers and the gradient $\nabla_u J_\alpha$ is given by

$$\nabla_u J_\alpha^T = \frac{\partial J}{\partial u} + \frac{\partial J}{\partial x}\frac{\partial x}{\partial u} + \alpha^T \frac{\partial F}{\partial u} + \alpha^T \frac{\partial F}{\partial x}\frac{\partial x}{\partial u} + F^T \frac{\partial \alpha}{\partial u} \tag{9a}$$

$$\nabla_u J_\alpha^T = \frac{\partial J}{\partial u} + \alpha^T \frac{\partial F}{\partial u} \tag{9b}$$

While α satisfies the adjoint equation

$$\frac{\partial F^T}{\partial x}\alpha = -\frac{\partial J^T}{\partial x} \tag{10}$$

From Equations (9a), (9b) and (10), the gradient with respect to time step n is computed from Equation (11)

$$\nabla_{u^n} J_\alpha = \frac{\partial J^T}{\partial u} + \frac{\partial F^{nT}}{\partial u^n}\alpha^n \tag{11}$$

The adjoint equations for time step n are obtained as Equations (12) and (13)

$$\left[I - \frac{\partial g(v^n, s^n)}{\partial s^n}\right]^T \alpha_s^n = \alpha_s^{n+1} - \frac{\partial J^{nT}}{\partial s^n} - \left[\frac{\partial B(s^n)v^{n+1}}{\partial s^n}\right]^T \alpha_v^{n+1} \tag{12}$$

$$\begin{bmatrix} B(s^{n-1}) & C & D \\ C^T & 0 & 0 \\ D^T & 0 & o \end{bmatrix} \begin{bmatrix} \alpha_v^n \\ \alpha_p^n \\ \alpha_\pi^n \end{bmatrix} = \begin{bmatrix} -\frac{\partial J^{nT}}{\partial v^n} + \frac{\partial g(v^n, s^n)^T}{\partial v^n}\alpha_s^n \\ 0 \\ 0 \end{bmatrix} \tag{13}$$

Solving the adjoint equations, the gradient of the objective function J at a time step n is given by equation 14

$$\nabla_{u^n} J = \frac{\partial J^T}{\partial u^n} - A_D^{nT}\alpha_v^n - A_N^{nT}\alpha_\pi^n \tag{14}$$

The gradient Equation (14) can be used in any gradient-based methods.

3.2 Optimization Method

The goal of production optimization problem is finding the right combination of well settings, i.e., the bottom-hole pressure (BHP) and the flow rates, to maximize an economic objective function, namely the net present value (NPV) (Najafiazar, 2014).

For a given configuration of wells as in particular for a flooding scenario involving multiple injectors and producers, the well rates or pressures is used to optimize the flooding process over the life of the reservoir (Jansen, *et al*., 2008).

MRST uses the ***OptimizeObjective*** function under its ***adjoint*** module which uses an aggressive line search based on the given gradient. The algorithm handles box constraints, and linear equality and inequality constraints. It performs on an iterative scheme, applying the constraints to the gradient until convergence is achieved. The algorithm makes use of the *gradient projection method.*

4. RESULTS AND DISCUSSION

In this work, water flooding scenarios were assessed for three test cases for the same well using real reservoir data from a field in the Niger Delta region of Nigeria.

4.1 The reservoir model

The reservoir model setup consists of a two-phase oil/water model with some compressibility through a heterogeneous porous medium. A reservoir of constant thickness is assumed with gravity and capillary forces neglected. For the different flooding scenarios of multiple injectors and producers, well rates and bottom – hole pressures (BHP) are used to optimize the flooding process over the entire life of the reservoir respectively. The reservoir area is about 12,500 m×20,000 m and a thickness of approximately 5 m and modelled as 50×50×5 m. Typical pressure and saturation distribution in the well before simulation are shown in Figures 1 and 2.

In Figure 1, the injector wells are seen as the deep red colouration at different positions while the producer wells are seen as the deep blue colourations. In Figure 2, the colour scale corresponds to injection rates of the segments, with blue being lowest rates (almost closed) and brown being highest (fully open).

Different scenarios of well placements at different positions were considered and the results were compared. The reservoir was modelled using the reservoir properties of the field. Each test scenario has injector wells and three producer wells.

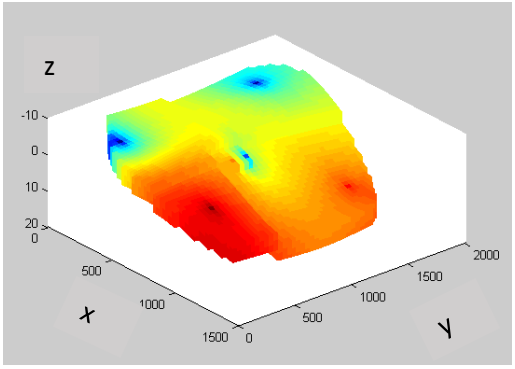

Figure 1: Pressure distribution in the modelled reservoir before simulation.

A simple NPV as economic objective function was desired to be maximized; the oil revenue was set to $50 per barrel and the water injection and production cost at $10 per barrel. The water cut in the producer was set to be profitable at or below 70% (that is, the well is no longer profitable as the water cut in the producer

exceeds about 0.70). Three different scenarios considered with well placement positions as follows:

1) The wells and simulation schedule are defined by three producer wells operating at the fixed bottom hole pressure and perforated throughout all layers of the model along with a single injector injecting one pore volume over 10 years (the total simulation length).

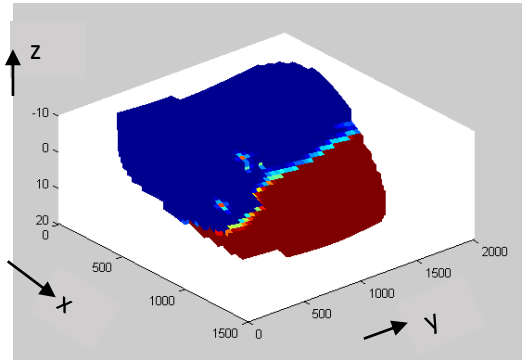

Figure 2: Saturation distribution in the modelled reservoir before simulation.

2) The wells and simulation schedule are defined by three producer wells operating at the fixed bottom hole pressure and three injector wells each injecting one pore volume over the total simulation length (10 years).

3) Three producer wells operating at the fixed bottom hole pressure and three injector wells each injecting one pore volume over the total simulation length (10 years) with different injector and producer wells as scenario (b).

The reference case is a constant rate/BHP case, with the all-producer BHPs at 250 bar (≈3700 psia). The injection rate is constrained at a maximum rate of 3000 STBD per injector and the producer BHPs at a minimum of 200 bar (≈2910 psia) and a maximum of 350 bar (≈5080 psia). The initial simulation input is constant and equal rate for the all injectors and constant BHP for the producer. The initial simulation time is set to 3650 days (10 years). Figures 3, 4 and 5 show the accumulated water cut for the three production scenarios. For Scenario 1, The producer well, P1 was profitable for about 3500 days and produced about equal amount of oil and water between 2,300 to 2,400 days. The producer well, P2 was at no time profitable. From day 1 to 1000th day, only water was being produced. The producer well, P3 was profitable for the first 10 years (3650 days) of production and produced only oil for about the first 1,400 days (3.8 years). For Scenario 2, the producer well, P1 was profitable for about 1300 days and produced only oil for about the first 400 days. It produced about 50% oil and water after 1000 days. The producer well, P2 was also profitable for about 1300 and produced only oil for about the first 250 days. The producer well, P3 was only profitable for less than about 100 days. For Scenario 3, the producer well, P1 was profitable for about 1100 days and produced only oil for about the first 400 days. The producer well, P2 was at no time profitable. From day 1 to the 250th day, only water was being produced. The producer well, P3 was only profitable for about 1600 days and P2 produced only oil for about the first 400 days. The profitability days result for all the scenarios is given in Table 1.

Table 1: Producer wells profitability days for the different scenarios

Scenario	Profitability of Producer Wells (Days)		
	P1	P2	P3
1	3500	None	>3500
2	1300	1300	100
3	1100	None	1700

were compared. The reservoir was modelled using the reservoir properties of the field. Each test scenario has injector wells and three producer wells. A simple NPV as economic object function was desired to be maximized; the oil revenue was set to $50 per barrel and the water injection and production cost at $10 per barrel. The water cut in the producer was set to be profitable at or below 70% (that is, the well is no longer profitable as the water cut in the producer exceeds about 0.70). Three different scenarios considered with well placement positions are:

1) The wells and simulation schedule are defined by three producer wells operating at the fixed bottom hole pressure and perforated throughout all layers of the model along with a single injector injecting one pore volume over 10 years (the total simulation length).
2) The wells and simulation schedule are defined by three producer wells operating at the fixed bottom hole pressure and three injector wells each injecting one pore volume over the total simulation length (10 years).
3) Three producer wells operating at the fixed bottom hole pressure and three injector wells each injecting one pore volume over the total simulation

length (10 years) with different injector and producer wells as scenario 2.

The reference case is a constant rate/BHP case, with the oil producer BHPs at 250 bar ($\approx 3700\,psia$). The injection rate is constrained at a maximum rate of 3000 STBD per injector and the producer BHPs at a minimum of 200 bar ($\approx 2910\,psia$) and a maximum of 350 bar ($\approx 5080\,psia$). The initial simulation input is constant and equal rate for the all injectors and constant BHP for the producer. The initial simulation time is set to 3650 days (10 years). Figures 4, 5 and 6 show the accumulated water cut for the three production scenarios. For Scenario 1, The producer well, P1 was profitable.

From the water cut performance criterion, the optimal well placement positions for this reservoir can be chosen. For an optimal production for a period of 10 years, the production wells with the profitability over a 10-year period are chosen.

For an optimal production less than 10 years, the production wells with profitability less than 10 years are chosen. Some wells that are not profitable at any point in time should not even be developed at all.

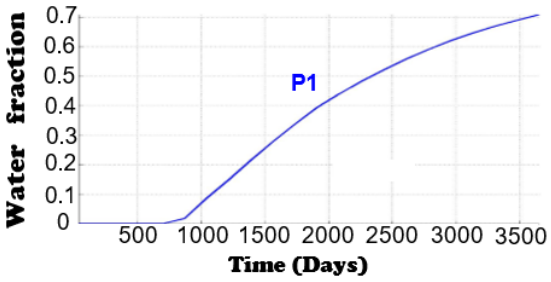

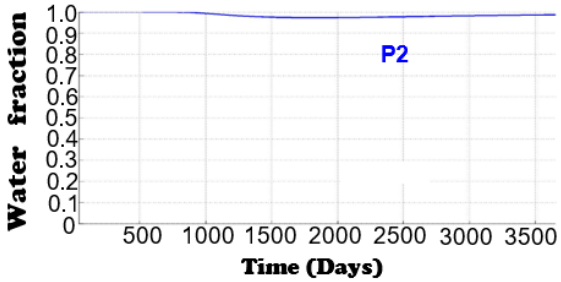

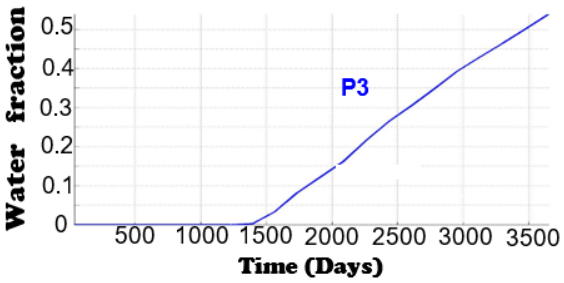

Figure 3: Accumulated water cut at reservoir conditions for Scenario 1

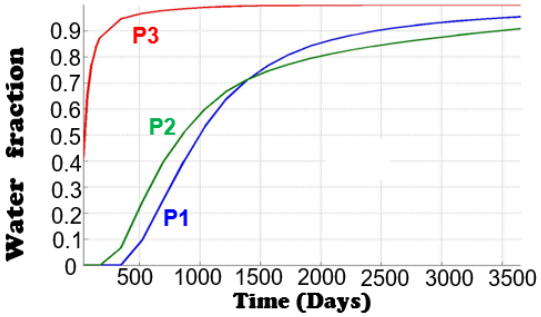

Figure 4: Accumulated water cut at reservoir conditions for scenario 2

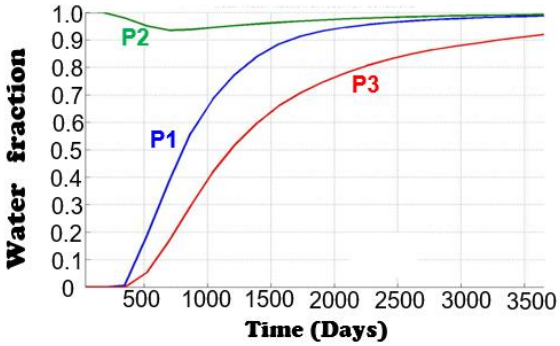

Figure 5: Accumulated water cut at reservoir conditions for scenario 3

5.0 CONCLUSION AND RECOMMENDATIONS

This work employed an open-source simulator MRST as an efficient technique for reservoir production optimization. The effect of well placement on the NPV of a reservoir was investigated and it can be seen that Well placement (injector and producer wells) affects well productivity and profitability.

ACKNOWLEDGEMENTS

Special appreciation to the important contributors to this work, including late Prof. A. A. Adepelumi and Dr. Oladele Bello for providing us with the required data for this work.

REFERENCES

Aarnes, J.E., Gimse, T. and Lie, K.A. (2007). An introduction to the numerics of flow in porous media using Matlab. In *Geometric modelling, numerical simulation, and optimization* (pp. 265-306). Springer, Berlin, Heidelberg.

Babayev, D. A. (1975). Mathematical models for optimal timing of drilling on multilayer oil and gas fields. *Manage Science*, 12(21), pp. 1361-1369.

Najafiazar, B. (2014) *Mathematical Optimization in Reservoir Management*, Master's thesis, Institutt for petroleumsteknologi og anvendt geofysikk.

Brouwer, D.R. and Jansen, J.D. (2002) October. Dynamic optimization of water flooding with smart wells using optimal control theory. In European petroleum conference. OnePetro.

Brouwer, D R; Naevdal, G; Jansen, J D; Vefring, E H; van Kruijsdijk, C P. (2004). *Improved reservoir management through optimal control and continuous model updating.* Houston, Texas, s.n.

Chen, C., Li, G. and Reynolds, A.C. (2012) Robust constrained optimization of short-and long-term net present value for closed-loop reservoir management. *SPE Journal*, *17*(03), pp.849-864.

ExxonMobil Corporation (2004). *ExxonMobil Corporation, Energy Outlook to 2030, technical report.* [Online] Available at: www.exxonmobil.com/energyoutlook [Accessed 15 September 2015].

Heijn, T., Markovinovic, R. and Jansen, J.D (2004) Generation of low-order reservoir models using system-theoretical concepts. *SPE Journal*, *9*(02), pp.202-218.

Hou, J., Zhou, K., Zhang, X.S., Kang, X.D. and Xie, H. (2015). A review of closed-loop reservoir management. *Petroleum Science*, *12*(1), pp.114-128.

Jansen, J., Bosgra, O. H. & den Hof, P. M. V. (2008). Model-based control of multiphase flow in subsurface oil reservoirs. *Journal of Process Control*, Volume 18, pp. 846 - 855.

Lasdon, L., Coffman Jr, P.E., MacDonald, R., McFarland, J.W. and Sepehrnoori, K. (1986) Optimal hydrocarbon reservoir production policies. *Operations Research*, *34*(1), pp.40-54.

Lie, K A; Krogstad, S; Ligaarden, I S; Natvig, J R; Nilsen, H M; Skaflestad, B (2012). Open source matlab implementation of consistent discretisations on complex grids. *Computer Geosciences*, 16(2), pp. 297 - 322.

Rosenwald, G. W. & Green, D. W. (1974). A method for determining the optimum location of wells in a reservoir using mixed-integer programming. *SPE Journal*, 1(14), pp. 44-54.

Rossi, D. C. M. K. J. L. D. M. S. (2002). *Reservoir and Production Optimization, white paper.* [Online] Available at: www.slb.com [Accessed 8 September 2015].

Van den Hof, P.M., Jansen, J.D. and Heemink, A., (2012) Recent developments in model-based optimization and control of subsurface flow in oil reservoirs. *IFAC Proceedings Volumes*, *45*(8), pp.189-200.

Van Essen, G. M., Van den Hof, P. M. & Jansen, J. D. (2011). Hierarchical long-term and short-term production optimization. *SPE Journal*, 1(16), pp. 191-199.

DOI: 10.51975/23380202.som
Journal of the Nigerian Society of Chemical Engineers, 38(2), 2023

EFFECT OF MICROWAVE SPRAY DRYING ON PINEAPPLE JUICE POWDER MOISTURE CONTENT, SOLUBILITY AND BULK DENSITY

***Aliyu, A. B. [1,2], Arshad, A. [2], Adnan, R[2] and Bemgba B. N.[2]**

[1]Department of Chemical Engineering, University of Maiduguri, Bama Road, P.M.B 1069, Maiduguri, Borno State, Nigeria.

[2]Faculty of Chemical and Energy Engineering, Universiti Teknologi Malaysia, 81310 UTM Skudai, Johor Bahru, Malaysia.

*Corresponding Author: aliyub@unimaid.edu.ng

ABSTRACT

Microwave spray drying (MWSD) innovatively couples Microwave (MW) with Spray Drying (SD) to intensify energy transfer and evaporation to dry droplets and produce dry particles. The application of MWSD to produce pineapple juice powder was studied, and powder quality for product powders at 0.2 kW MW power intensity were compared with those for conventional SD for 20%, 30% and 40% feed solids contents. The moisture content of MWSD juice powders ranges from 2.31% to 5.78%, compared to 2.62% to 6.33% for conventional SD. Bulk density variations span from 210 kg/m³ to 337.69 kg/m³ for MWSD and 243.44 kg/m³ to 390.05 kg/m³ for conventional SD. Solubility values for MWSD juice powders range from 245 s to 392 s, while conventional SD powders range from 243 s to 422 s. The results reveal that MWSD produces powders with a lower moisture content, comparable or lower bulk density, and higher solubility than conventional SD. MWSD uses milder inlet air temperature ranges of 105 ^{o}C to 115 ^{o}C, compared to 130 ^{o}C to 150 ^{o}C for conventional SD, to produce pineapple juice powders with better quality, underscoring its potential for enhancing product quality and manufacturing efficiency.

***Keywords**: Pineapple juice; Microwave spray drying; Moisture content; Bulk density; Solubility; Powder quality*

1. INTRODUCTION

Spray drying (SD) is a continuous operation involving the thermal dehydration of atomized sprays of fluid feed droplets in a hot drying medium to generate dried particles (Filková and Mujumdar, 2020). The product particulate powder has low moisture content, suffers little or no thermal degradation and almost retains the quality of the original feed when reconstituted. Spray dried powders have advantages of reduced weight and bulk volume, extended shelf life, minimal storage, transport and handling requirements, and most importantly, resistance to physicochemical and microbial degradation (Filkova et al., 2014; Sobulska and Zbicinski, 2021). Modern diet habits and the appeal for wholesome functional foods that nourish and retain their natural flavours have driven innovations for spray dried foods such as pineapple juice powder, which can be reconstituted, with the addition of water (Betoret et al., 2011; Etzbach et al., 2020). Pineapple (*Ananas sp.*), is a good source of dietary nutrients with salubrious effects on human health. It is a natural source of dietary bromelain in addition to bioactive compounds such as magnesium, potassium, calcium, vitamins A, and C, as well as monosaccharides such as fructose and sucrose (FoodData Central, 2019).

Advances in spray drying operations are expected to address the growing demand for high-quality products and improved energy efficiencies to reduce costs. One attribute of such new innovation is envisaged to involve a hybrid or different heat source (Mujumdar and Huang, 2007). A recent innovative approach incorporates microwave (MW) with existing spray drying technology to create an intensified microwave spray drying (MWSD) process (Vogt and Unruh, 1992). Microwaves are a form of electromagnetic energy with frequencies in the range of 300 MHz to 300 GHz, over a wavelength range of 1 m to 1 mm (Schiffmann, 2014). Incident microwaves in lossy dielectric materials are partially dissipated into heat energy within the material through molecular interactions with the MW electromagnetic field (Sun et al., 2016). The alternating MW electromagnetic field causes molecular motion through the migration of ionic species and/or rotation of dipolar species; rotation is dominant for materials with high free water (Schiffmann, 2014; Sun et al., 2016). The

molecular motion reverses in synchronicity with the MW frequency, causing increase in temperature throughout the material, and is known as volumetric (dielectric) heating (Chandrasekaran et al., 2013; Sun et al., 2016). High dielectric lossy materials, such as water, dissipate higher electromagnetic energy in relative magnitude to the electromagnetic intensity, leading to potential temperature levelling and self-regulating process. This unique ability of microwaves to transfer energy throughout the volume of the material, has led to faster heating rates and increased energy efficiency, thus distinguishing it from other energy transfer processes (Venkatesh and Raghavan, 2004; Sun et al., 2016). MWSD integrates MW into the spray drying process by irradiating drying droplets inside the SD chamber. The liquid or wet droplets absorb the MW and undergo volumetric heating and evaporation of moisture to form dry particles. The process is self-regulating as the rate of heating depends on the droplet moisture content which decreases as drying proceeds (Vogt and Unruh, 1992; Sun et al., 2016).

MW has been applied for drying products such as seeds (Hemis et al., 2015), vegetables (Liu et al., 2012; Malafronte et al., 2012), fruits (Li et al., 2011; Motavali et al., 2013), and honey (Cui et al., 2008; Guo et al., 2011). While microwave drying has been applied to various products, the concept of MWSD is still in its exploratory stage, with limited published information thus, there is a need for further research. The objective of this study was to produce pineapple juice powders, using a MW power intensity level of 0.2 kW, and to evaluate the product MWSD powder properties of moisture content, solubility, bulk and tapped densities. The MWSD powder properties are further compared with SD powder properties to assess their quality.

2. MATERIAL AND METHODS

2.1. Juice feed preparation

Freshly harvested ripe pineapples (*josapine cultivar*), with pronounced yellowing (indicative of ripeness) were procured. These were washed, skinned, diced into rectangular pieces and then juiced using a domestic juicer. The extracted juice was filtered through a 35-mesh kitchen sieve and analysed for moisture content and specific gravity respectively; using a moisture analyser (Ohaus model MB25) and specific gravity glass bottles. Averaged triplicate measurements of the extracted juice moisture content were used to prepare desired feed solids of 20% and 30% by adding precise calculated masses of maltodextrin.

2.2. Spray drying and microwave spray drying

A fabricated dual mode laboratory scale spray dryer (Dawnyx Technology Sdn. Bhd), shown schematically in **Figure 1**, was used for conventional and microwave spray drying. The spray dryer design functions as a conventional spray dryer when the microwave generator is in OFF mode. The drying configuration is concurrent with atomised feed and drying air flowing from top to bottom in the conventional mode but are simultaneously irradiated with microwaves under MWSD mode. During operation, the compressed air supply passes through a filter to remove suspended particles before being supplied to the atomiser and drying air heater. The single source compressed air supply to the atomiser is controlled while the drying air flowrate is fully opened due to limitations of supply. The pineapple-maltodextrin feed was constantly stirred using a magnetic stirrer and dozed, using a hygienic pump (Masterflex model 7518-10) at a constant rate of 20 mL/min, to the twin-fluid atomiser where it was atomised into a spray of droplets inside the drying chamber. The operating conditions for the reported results are presented in **Table 1**. The resulting product powder under both SD and MWSD drying conditions was collected from a flask at the base of the cyclone and immediately transferred into airtight glass containers for further analysis.

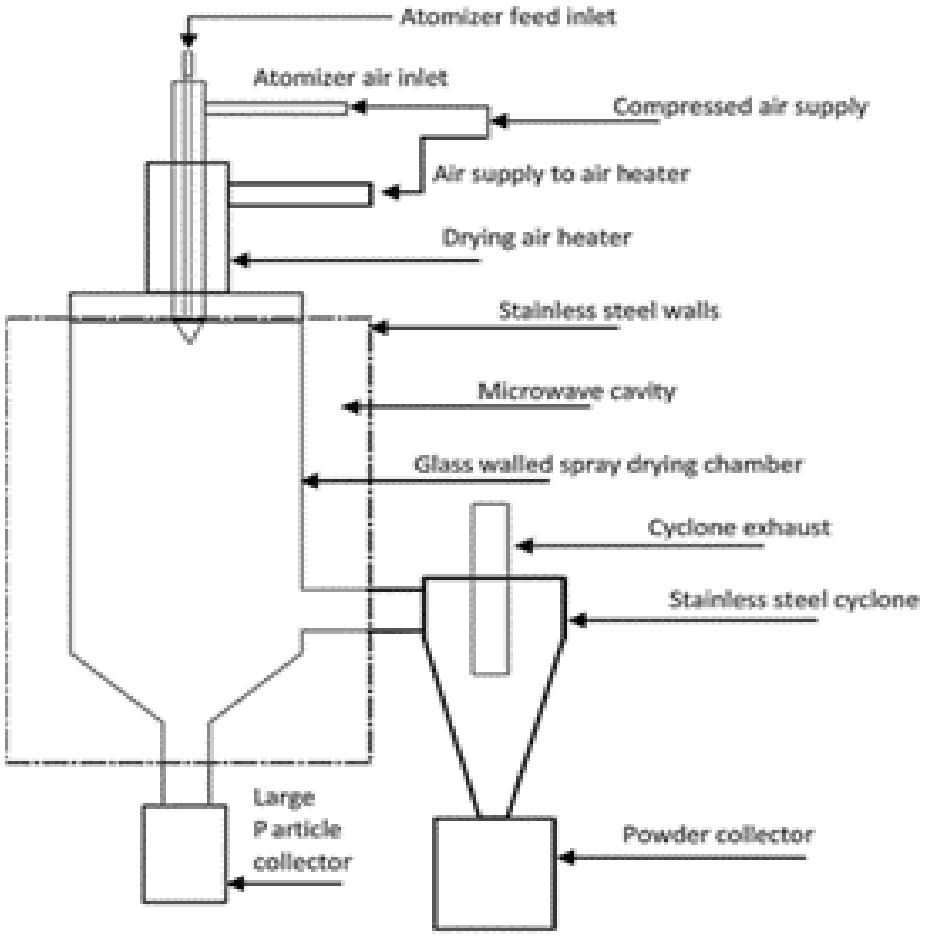

Figure 1: Microwave spray dryer schematic
(Source: Author)

Table 1: Spray drying experiments operating conditions

Feed solids fraction	Conventional spray drying			Microwave spray drying			
	Air temperature (^oC)	Air Flowrate (m^3/s)	Air absolute humidity (kg H_2O/kg dry air)	MW power (kW)	Air temperature (^oC)	Air Flowrate (m^3/s)	Air absolute humidity (kg H_2O/kg dry air)
0.2	130	0.00567	0.005064	0.2	105	0.00564	0.005549
0.2	140	0.006	0.005338	0.2	110	0.00598	0.004839
0.2	150	0.006	0.005034	0.2	115	0.00565	0.004904
0.3	130	0.0057	0.004958	0.2	105	0.00598	0.004467
0.3	140	0.00597	0.004958	0.2	110	0.00575	0.004904
0.3	150	0.00567	0.004388	0.2	115	0.00583	0.004467
0.4	130	0.00567	0.005123	0.2	105	0.00567	0.004471
0.4	140	0.0057	0.005324	0.2	110	0.00565	0.004471
0.4	150	0.00568	0.005324	0.2	115	0.00567	0.004791

2.2. Powder analysis

Moisture content: The moisture contents of the product powders were determined as weight percent of the wet

material, using a moisture analyser (Ohaus model MB25), at a temperature of 75 ^{o}C. Average values of the moisture content were calculated from triplicate sample measurements and expressed in % kg H_2O/kg sample (wet basis).

Bulk density and tapped density: The powder bulk density was determined by gently and rapidly transferring 2 grammes of powder into a clean, dry, empty 10 mL cylinder with 0.1 mL graduations and reading off the volume occupied by the powder (Goula and Adamopoulos, 2005; Jain and Singh, 2021). The average value of triplicate measurements of sample powder mass to its occupied volume in the cylinder were taken as its bulk density and expressed in kg/m^3.

The tapped powder density was subsequently determined by manually tapping the cylinder via the repeated dropping of the cylinder through a vertical distance of about 15 mm until the dried juice powder attains a constant volume. The average value of triplicate measurements of sample powder mass to its final constant volume in the cylinder were taken as its tapped density and expressed in kg/m^3 (Saikia et al., 2015).

Solubility: Powder solubility was analysed by adding 2 grammes of the sample powder to 50 mL of distilled water at 25 ^{o}C inside a 100 mL beaker (Goula and Adamopoulos, 2005). Care was taken to avoid powder contact with the beaker walls. A magnetic stirrer (Sybron Thermolyne Nuova II) set at 900 rpm was used to stir the contents in the beaker using a 14.9 mm by 6.5 mm plastic coated magnetized stirring bar. The complete dissolution of the powder was ensured by passing a bright light beam through the stirred beaker contents. The average value of triplicate measurements of the time taken for the sample powder particles to dissolve completely was taken as the solubility and expressed in seconds.

3. RESULTS AND DISCUSSION

3.1. Moisture content analysis

The moisture content of spray dried powders is an important indicator of powder quality and spray drying performance (Tan et al., 2011). **Figure 2** gives the variation of powder moisture contents, grouped by feed solids compositions, for product juice powders obtained from MWSD and conventional SD. From the data presented MWSD juice powders exhibit moisture contents ranging from 2.31% to 5.78%, while conventional SD powders fall within a slightly broader range of 2.62% to 6.33%. These moisture values align with findings from previous studies on spray-dried pineapple juice powders by Jittanit et al. (2010), Saikia et al. (2015) and Wong et al. (2015), which collectively support the observed moisture content trends.

The MWSD powders generally exhibit much lower powder moisture contents with increase in inlet drying air temperature compared to the conventional SD powders. Under conventional SD conditions, As the drying air temperature rises, the droplets experience elevated heating and evaporation rates. However, heat loss to the drying air and evaporation effects act in opposition to these rates, effectively cooling the droplets and reducing the temperature gradient cross the droplet surface. The mechanism differs for the MWSD process whereby, an increase in the drying air temperature, decreases the heat loss effects from the dielectrically heated droplets and more energy is internally available for moisture evaporation to produce drier juice powders. This phenomenon is in line with the findings of Vogt and Unruh (1992), who observed a similar effect in aqueous and ethanol sprays under MWSD conditions. The increase in droplet solids (feed composition) also plays a role in reducing moisture content, as it implies a lower initial moisture content in the atomized feed sprays. Consequently, more energy becomes available for evaporation, contributing to the production of drier powders. This finding aligns with the general understanding that higher feed solids lead to less moisture in the final product (Daza et al., 2016; Emam-Djomeh et al., 2016; Duangchuen et al., 2021).

Comparing the moisture contents of MWSD product powders to those from conventional SD reveals some important distinctions. While the trends in moisture content changes with temperature are similar in both methods, MWSD powders consistently exhibit lower moisture contents. This difference can be attributed to the fundamental distinction in how heat is transferred to the atomized feeds in these two drying processes. In MWSD, the dielectric heating of the droplets predominately provides the energy for droplet heating and moisture evaporation, which is more sensitive to moisture content and less sensitive to changes in drying air temperature. In contrast, conventional SD relies on the interfacial transfer of heat across the atomized droplet surface from the drying air, which becomes more efficient with higher inlet drying air temperatures. This heightened interfacial heat transfer in conventional SD results in increased moisture evaporation, leading to the

production of drier powders (Daza et al., 2016; Emam-Djomeh et al., 2016; Duangchuen et al., 2021). Several studies focusing on pineapple juice powders (Wong et al., 2015; Jittanit et al., 2010) and other fruit juices (Vivek et al., 2020; Karaca et al., 2016; Daza et al., 2016; Saikia et al., 2015; Santhalakshmy et al., 2015; Emam-Djomeh et al., 2016) have reported similar trends of moisture content decrease with increasing temperature, corroborating the observations in this study.

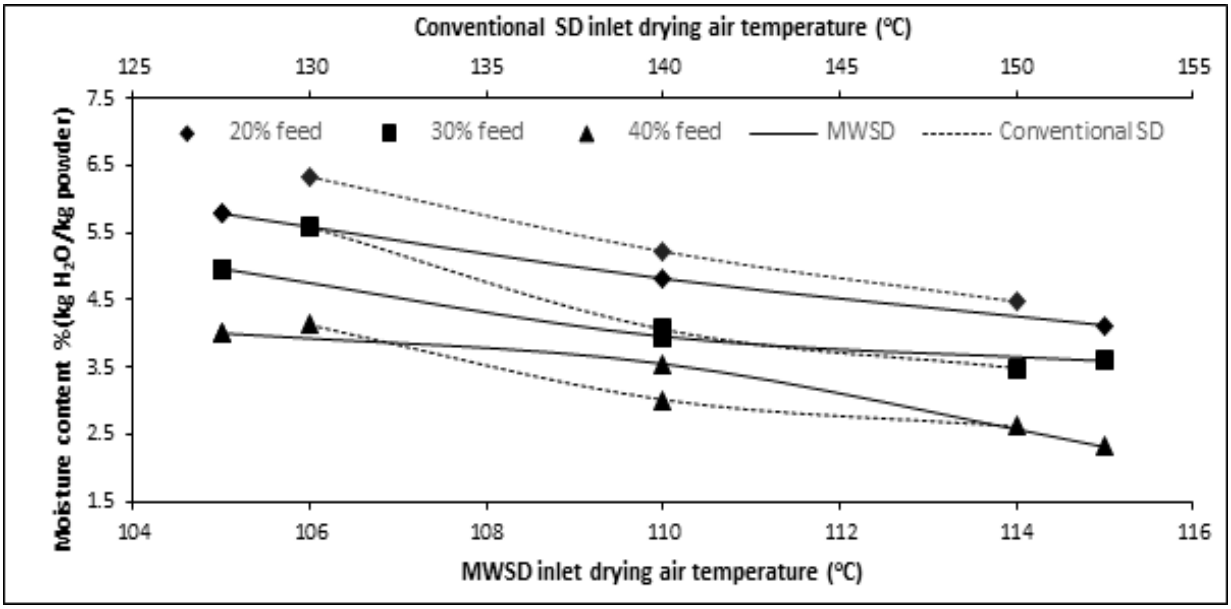

Figure 2. Powder moisture content against inlet drying air temperature for conventional and microwave spray drying for the different pineapple juice feed compositions

3.2. Juice powder bulk and tapped bulk densities

Bulk density is a vital specification for powders in the industry with wide applicability in assessing powder storage, processing, packaging and transport requirements (Barbosa-C´anovas et al., 2006). Several classes of bulk density are often used to define powders. The most often reported, in order of frequency, for food powders are respectively 'tapped' and 'loose' (also termed poured) bulk density (Abdullah and Geldart, 1999). The measured 'loose' powder bulk densities for MWSD and conventional SD, grouped by the respective feed solids contents, are shown in **Figure 3**.

The bulk density of juice powders generated through MWSD are observed to vary from 210 kg/m^3 to 337.69 kg/m^3, compared to the conventional spray dried powders which, range from 243.44 kg/m^3 to 390.05 kg/m^3. These findings align with previous studies on pineapple juice powder and comply with established range values for food powders, as documented by various researchers (Barbosa-C´anovas et al., 2006; Jittanit et al., 2010; Wong et al., 2015; Jimenez-Sánchez et al., 2020).

The variability in bulk density can be attributed to several factors. Bulk density is intricately linked to powder moisture content, particle size, and the distribution of particle sizes within the powder. Smaller particle sizes result in greater compaction and, consequently, higher bulk density values. Furthermore, an increased composition of feed solids tends to enhance material density (Abdullah and Geldart, 1999; Barbosa-C´anovas et al., 2006). It is important to note that volumetric heating, a unique feature of MWSD, appears to offer advantages by facilitating rapid moisture evaporation rates. This can help mitigate the formation of impermeable films on and occluded voids inside the particles. Consequently, this can favour the production of drier, smaller powder particles with higher bulk density values (Schulze, 2008; Sokhansanj and Jayas, 2014; Jimenez-Sánchez et al., 2020). When examining the influence of feed solids composition, it becomes evident that changes in bulk density are minimal at lower compositions, but a pronounced increase occurs as the feed solids composition exceeds 20%. The rise in bulk density at higher feed solids compositions can be attributed to the observed formation of powder clumps. These clumps introduce voids within the product powders, resulting in larger measured powder bulk

volumes and subsequently reduced bulk densities (Nishad et al., 2017; García-Lucas et al., 2016; Abdullah and Geldart, 1999).

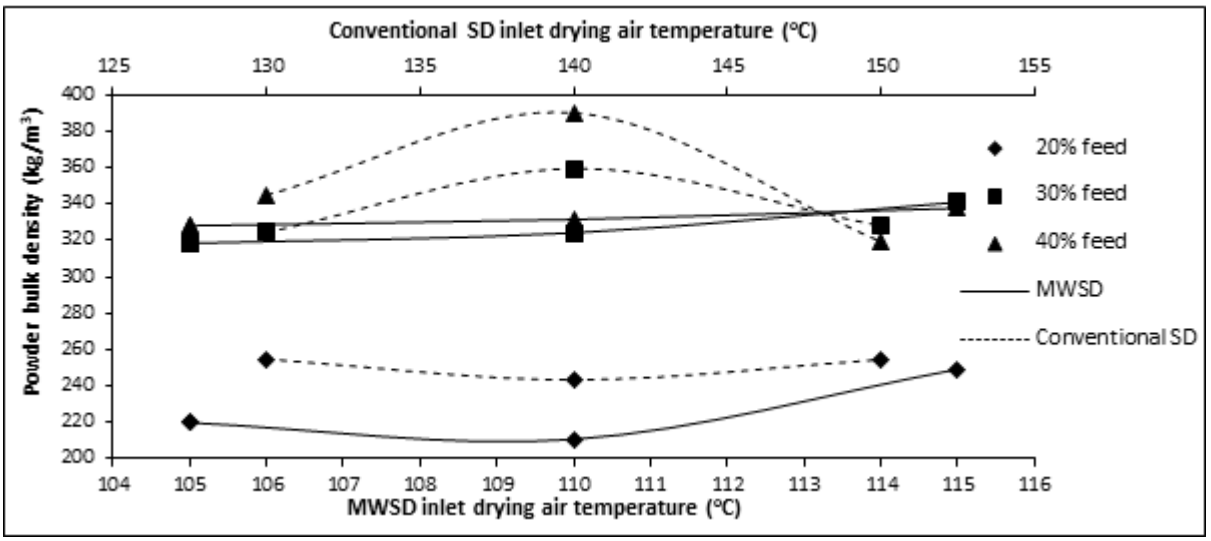

Figure 3. Powder bulk density against inlet drying air temperature for conventional and microwave spray drying for the different pineapple juice feed compositions

Comparing the bulk density values between MWSD and conventional spray-dried pineapple juice powders in **Figure 3**, it is evident that MWSD powders exhibit lower bulk densities. This implies that MWSD powders comprise larger particles, are lighter and less compact, necessitating larger storage spaces compared to their conventional counterparts. In the case of conventional spray-dried powders, bulk density values display a convex-like pattern, with a rise and fall observed for feed solids compositions of 30% and higher. In contrast, the 20% feed compositions show a slight decrease in bulk density as the inlet drying air temperature increases. This trend can be attributed to the interplay of moisture content and the occurrence of powder stickiness and clumping during measurements, as discussed in previous studies (Barbosa-C´anovas et al., 2006; Khalilian Movahhed and Mohebbi, 2016; Goula et al., 2004).

Tapped bulk densities for MWSD and conventional SD, grouped by the respective feed solids compositions, are shown in **Figure 4**. The MWSD product powders exhibit tapped bulk densities ranging from 370.46 kg/m^3 to 723.1 kg/m^3 whereas the conventional spray-dried powders display a slightly narrower range of 527.29 kg/m^3 to 723.71 kg/m^3. The values are averagely higher compared to the reported tapped bulk density values by Wong et al. (2015).

It was observed that the MWSD product powders exhibit slight increases in bulk density with temperature, with the exception being at 115 °C for the 40% feed composition. This temperature-dependent behaviour can be attributed to the complex interplay between heat loss and moisture evaporation, as previously discussed. It is noteworthy that, for a specified feed composition, bulk density tends to increase as the inlet drying air temperature rises. This trend aligns with findings reported for spray-dried pineapple juice powders by Wong et al. (2015), indicating the sensitivity of bulk density to drying conditions. The convex-like trend observed in the bulk densities of conventional SD product powders, previously discussed for loose bulk density, is also discernible in the tapped bulk density results. It was observed that even after consecutive tapping during the determination of tapped bulk density, some voids were still visible to the unaided eye. This indicates that the powder particles in the conventional SD product powders retain a degree of inter-particle void spaces.

Comparing the tapped bulk density values to the loose bulk density values presented in **Figure 3** reveals a substantial difference, with tapped values being significantly higher. This phenomenon, characterized by higher ‘tapped’ bulk densities compared to ‘loose’ ones, has been previously documented by Saikia et al. (2015), Nishad et al. (2017) and, Abdullah and Geldart (1999). The underlying reason for this is attributed to the

compaction of the powder particles during tapping, leading to reduced inter-particle void spaces. For the MWSD product juice powders, they tend to exhibit lower tapped bulk densities compared to their conventional spray-dried counterparts. **Figure 4** highlights a substantial difference in values, particularly for the 20% feed solids composition. The higher bulk densities observed for conventional SD powders are attributed to their either smaller particle sizes or stickier nature, which promotes increased particle adhesion and compaction during tapping. Conversely, MWSD product powders display less stickiness, resulting in lower tapped bulk densities.

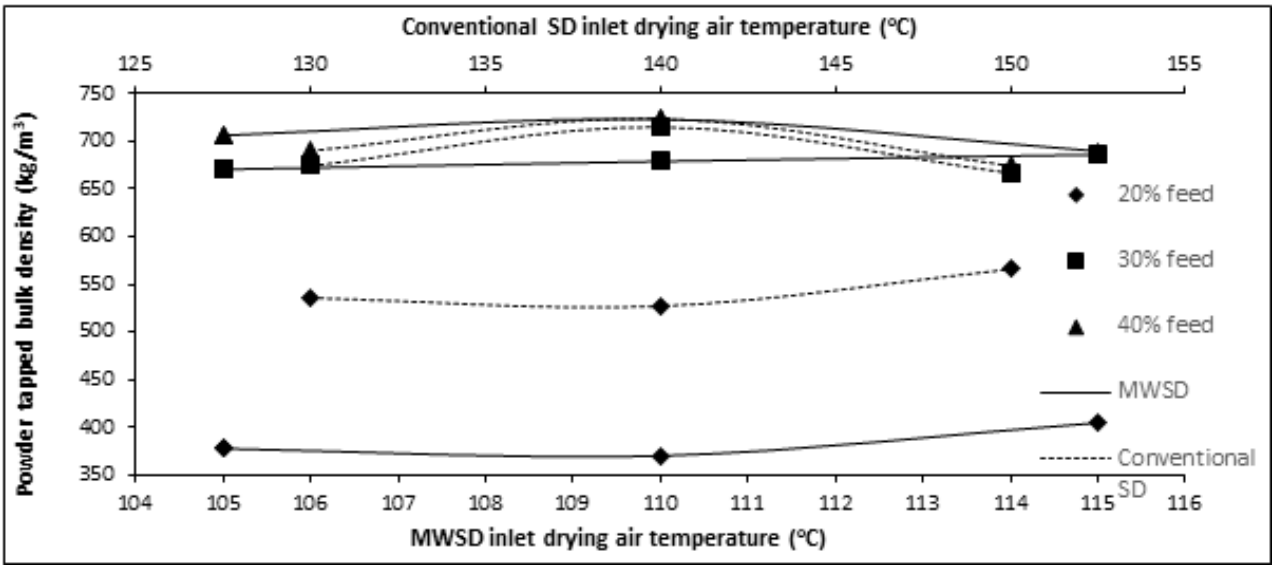

Figure 4. Powder tapped bulk density against inlet drying air temperature for conventional and microwave spray drying for the different pineapple juice feed compositions.

3.3. Juice powder

The solubility of water-soluble food powders greatly influences their functionality and quality in industry (Barbosa-C´anovas et al., 2006). **Figure 5** shows the variation of powder solubility with inlet drying air temperature for MWSD and conventional SD product pineapple juice powders.

The MWSD juice powders solubility varied from 245 s to 392 s compared to 243 s to 422 s for the conventional spray dried powders. These variations in solubility align with the changes in inlet drying air temperature, as well as the moisture content profiles depicted in **Figure 2**. An increase in the inlet drying air temperature has several favourable effects, including reduced droplet heat loss, enhanced volumetric heating, and more efficient internal moisture evaporation. These factors collectively contribute to the production of drier particles with increased solubility. Thus, the MWSD product juice powders display an increase in solubility as the inlet drying air temperature rises. Also, a decrease in solubility at 115 °C for the 40% feed solids composition was observed, which can be attributed to the occurrence of powder flotation. The relationship between MWSD product powder solubilities and feed solids content shows an interesting pattern. Solubilities tend to increase in correspondence with the increase in "tapped" bulk densities. In practical terms, this means that denser product powders, such as those resulting from the 40% solids feed, tend to sink more quickly, while lighter powders, like those from the 30% solids feed, tend to float and take longer to sink and dissolve. Faster submergence of powder particles is influenced by various factors, including porosity, crust moisture permeability, and overall moisture affinity, which collectively affect moisture penetration and particle dissolution.

Comparing the solubility of powders between the MWSD and conventional spray drying operations reveals differences. MWSD powders consistently exhibit higher solubility compared to their conventionally spray-dried powders. This is attributed to the dryness of MWSD powders and the absence of a hardened crust. In contrast, conventional SD product powders show increases in solubility with an increase in inlet drying air temperature. However, during the dissolution process, multiple small sticky agglomerates are observed, which take longer to dissolve as powder moisture content decreases. This effect can be associated with the

hardening of the particle crust layer due to higher drying air temperatures, which reduces the permeability of powder particles to moisture. Furthermore, the trend of increasing solubility with higher "tapped" bulk density, which was noted for MWSD product juice powders, is also discerned for conventional SD product juice powders. A higher bulk density implies faster powder submergence to balance static forces, facilitating faster wetting and eventual dissolution of powder particles.

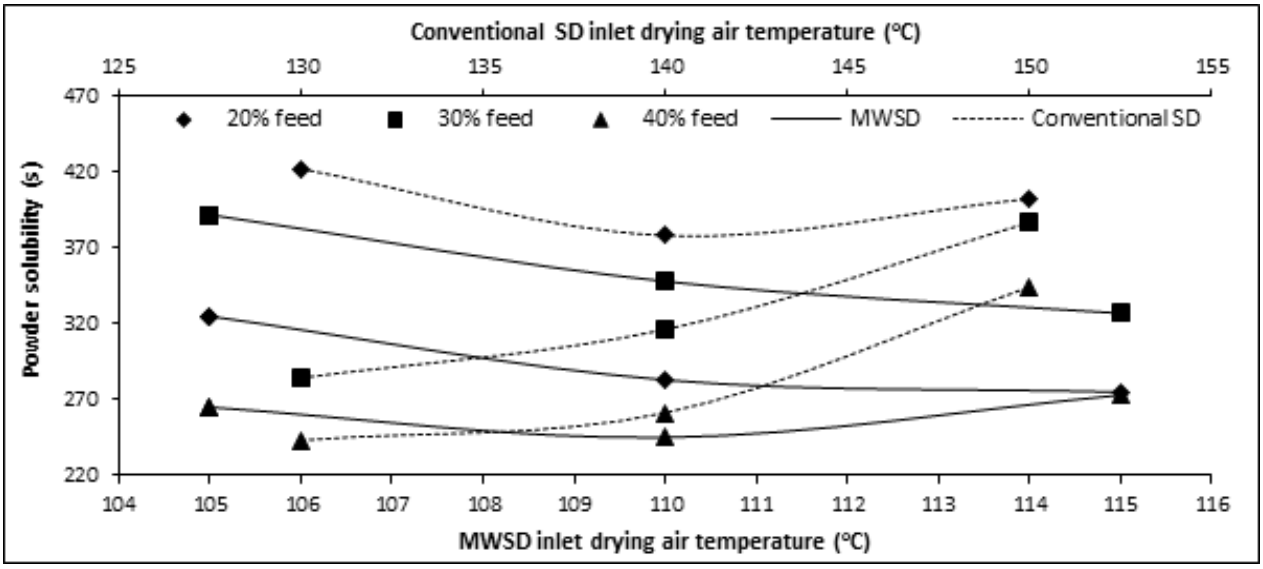

Figure 5. Powder solubility against inlet drying air temperature for conventional and microwave spray drying for the different pineapple juice feed compositions.

4. CONCLUSION

The application of MW to intensify the spray drying of pineapple juice to produce dry juice powder was studied. MWSD of pineapple juice feeds to produce dry powder was successful under the studied conditions of MW power intensity of 0.2 kW. Inlet drying air temperatures of 105 ^{o}C were the lowest reached for powder production from the 20% feed solids composition, and represents a threshold below which sticky deposits rather than powders were produced. For the 40% feed solids composition, powder production increased at Inlet drying air temperatures above 70 ^{o}C, while increased powder stickiness and reduced powder production was favoured as the drying air temperature decreased to 60 ^{o}C. For the study conditions, wall deposits were light and easily cleaned for favourable MWSD conditions, but heavy, sticky, and difficult to wash off under unfavourable MWSD conditions.

The study examined the juice powders properties of moisture content, bulk densities, and solubility for powders produced under MWSD and conventional SD conditions. MWSD juice powders consistently exhibited a lower moisture content compared to conventional spray dried powders. This can be attributed to the distinct mechanisms of heat transfer in the two drying processes. MWSD relies on dielectric heating, which is more sensitive to moisture content, resulting in drier powders with increasing inlet drying air temperature. Conversely, conventional spray drying relies on interfacial heat transfer, which is more efficient at higher temperatures, also leading to drier powders. These findings are consistent with previous studies on pineapple juice powders and other fruit juices. MWSD powders exhibited lower bulk densities compared to conventional SD powders. The differences in bulk density were attributed to particle size, moisture content, and feed solids composition. MWSD's unique volumetric heating mechanism was found to facilitate rapid moisture evaporation and inflation, resulting in drier, bigger particles with smaller bulk density values. Conversely, conventional SD powders displayed a convex-like trend in bulk density with changes in feed solids composition and drying air temperature. The study highlighted the difference between ‘tapped’ and ‘loose’ bulk density values, with ‘tapped’ values consistently higher due to particle compaction during tapping. This observation aligns with previous research and underscores the importance of considering the compaction state when assessing the bulk density. MWSD powders consistently exhibited higher solubility compared to conventional SD powders. This difference

was attributed to the absence of a hardened crust in the MWSD powders, which facilitates quicker dissolution. The study also noted that solubility increased with higher 'tapped' bulk density, indicating that denser powders tend to dissolve more rapidly.

The study provides valuable information on the effect of 0.2 kW MWSD on the production of pineapple juice powders and with desirable quality characteristics such as moisture content, bulk density, and solubility. The study potentially demonstrates a spray drying intensification approach using microwave and has implications for product quality, spray drying performance and similar approaches to intensify spray drying processes in the industry.

ACKNOWLEDGEMENT

The authors acknowledge the technical assistance of Mohammad Rafiza Bin Othman and Mohd Nur Shairray Bin Jais.

Funding: The support of UTM, Ministry of Higher Education (MOHE), Research University Grant (RUG) and Vot No. 02H90 are acknowledged for providing funding for the research.

REFERENCES

Abdullah, E. C. and Geldart, D. (1999). The Use of Bulk Density Measurements as Flowability Indicators. Powder Technology, 102: 151-165.

Barbosa-C´Anovas, G. V.; E. Ortega-Rivas; P. Juliano and H. Yan (2006). Food Powders: Physical Properties, Processing and Functionality. NewYork: Springer Science & Business Media.

Betoret, E.; Betoret, N.; Vidal, D. and Fito, P. (2011). Functional Foods Development: Trends and Technologies. Trends in Food Science & Technology, 22: 498-508.

Chandrasekaran, S.; Ramanathan, S. and Basak, Tanmay (2013). Microwave Food Processing—a Review. Food Research International, 52: 243-261.

Cui, Zheng-Wei; Sun, Li-Juan; Chen, Wei and Sun, Da-Wen (2008). Preparation of Dry Honey by Microwave–Vacuum Drying. Journal of Food Engineering, 84: 582-590.

Daza, L. D.; Fujita, A.; Favaro-Trindade, C. S.; Rodrigues-Ract, J. N.; Granato, D. and Genovese, M. I. (2016). Effect of Spray Drying Conditions on the Physical Properties of Cagaita (Eugenia Dysenterica Dc.) Fruit Extracts. Food and Bioproducts Processing, 97: 20-29.

Duangchuen, Jaruwan; Pathaveerat, Siwalak; Noypitak, Sirinad and Jermwongruttanachai, Phiraiwan (2021). Effect of Spray Drying Air Temperature to the Changes of Properties of Skimmed Coconut Milk Powder. Applied Science and Engineering Progress, 14: 187-195.

Emam-Djomeh, Zahra; Seddighi, Ameneh and Askari, Golamreza (2016). Influence of Process Conditions on the Functional Properties of Spray-Dried Seedless Black Barberry (Berberis Vulgaris) Juice Powder. Journal of Food Processing and Preservation: n/a-n/a.

Etzbach, Lara; Meinert, Messina; Faber, Thilo; Klein, Carolin; Schieber, Andreas and Weber, Fabian (2020). Effects of Carrier Agents on Powder Properties, Stability of Carotenoids, and Encapsulation Efficiency of Goldenberry (Physalis Peruviana L.) Powder Produced by Co-Current Spray Drying. Current Research in Food Science, 3: 73-81.

Filkova, I.; L. X. Huang and A. S. Mujumdar (2014). Industrial Spray Drying Systems. Handbook of Industrial Drying. 4th ed.: CRC Press.

Filková, Iva and Mujumdar, Arun S (2020). Industrial Spray Drying Systems. Handbook of Industrial Drying. CRC Press.

Fooddata Central. 2019. *Pineapple Juice, Canned or Bottled, Unsweetened, without Added Ascorbic Acid* [Online]. USDA. Available: https://fdc.nal.usda.gov/fdc-app.html#/food-details/169947/nutrients [Accessed 24/03/2023 2023].

García-Lucas, Karina A.; Méndez-Lagunas, Lilia L.; Rodríguez-Ramírez, Juan; Campanella, Osvaldo H.; Patel, Bhavesh K. and Barriada-Bernal, Luis Gerardo (2016). Physical Properties of Spray Dryed Stenocereus Griseus Pitaya Juice Powder. Journal of Food Process Engineering: n/a-n/a.

Goula, Athanasia M. and Adamopoulos, Konstantinos G. (2005). Spray Drying of Tomato Pulp in Dehumidified Air: Ii. The Effect on Powder Properties. Journal of Food Engineering, 66: 35-42.

Goula, Athanasia M.; Adamopoulos, Konstantinos G. and Kazakis, Nikolaos A. (2004). Influence of Spray Drying Conditions on Tomato Powder Properties. Drying Technology, 22: 1129-1151.

Guo, Wenchuan; Liu, Yi; Zhu, Xinhua and Wang, Shaojin (2011). Temperature-Dependent Dielectric Properties of Honey Associated with Dielectric Heating. Journal of Food Engineering, 102: 209-216.

Hemis, M.; Choudhary, R.; Gariepy, Y. and Raghavan, V. G. S. (2015). Experiments and Modelling of the Microwave Assisted Convective Drying of Canola Seeds. Biosystems Engineering, 139: 121-127.

Jain, Priti and Singh, Mohan (2021). Spray Drying of Rose Petal Juice: Effect of Air Temperature and Feed Flow Rate on Physical Attributes.

Jimenez-Sánchez, Darvin Ervey; Calderón-Santoyo, Montserrat; Herman-Lara, Erasmo; Gaston-Peña, Cristina; Luna-Solano, Guadalupe and Ragazzo-Sánchez, Juan Arturo (2020). Use of Native Agave Fructans as Stabilizers on Physicochemical Properties of Spray-Dried Pineapple Juice. Drying Technology, 38: 293-303.

Jittanit, Weerachet; Niti-Att, Siriwan and Techanuntachaikul, Onuma (2010). Study of Spray Drying of Pineapple Juice Using Maltodextrin as an Adjunct. Chiang Mai Journal of Science, 37: 9.

Karaca, A. C.; Guzel, O. and Ak, M. M. (2016). Effects of Processing Conditions and Formulation on Spray Drying of Sour Cherry Juice Concentrate. Journal of the Science of Food and Agriculture, 96: 449-455.

Khalilian Movahhed, Mohammad and Mohebbi, Mohebbat (2016). Spray Drying and Process Optimization of Carrot-Celery Juice. Journal of Food Processing and Preservation, 40: 212-225.

Li, Zhenfeng; Raghavan, G. S. V.; Wang, Ning and Vigneault, Clément (2011). Drying Rate Control in the Middle Stage of Microwave Drying. Journal of Food Engineering, 104: 234-238.

Liu, Peng; Zhang, Min and Mujumdar, Arun S. (2012). Comparison of Three Microwave-Assisted Drying Methods on the Physiochemical, Nutritional and Sensory Qualities of Re-Structured Purple-Fleshed Sweet Potato Granules. International Journal of Food Science & Technology, 47: 141-147.

Malafronte, Loredana; Lamberti, Gaetano; Barba, Anna Angela; Raaholt, Birgitta; Holtz, Emma and Ahrné, Lilia (2012). Combined Convective and Microwave Assisted Drying: Experiments and Modeling. Journal of Food Engineering, 112: 304-312.

Motavali, A.; Najafi, G. H.; Abbasi, S.; Minaei, S. and Ghaderi, A. (2013). Microwave-Vacuum Drying of Sour Cherry: Comparison of Mathematical Models and Artificial Neural Networks. J Food Sci Technol, 50: 714-22.

Mujumdar, A. S. and Huang, L. X. (2007). Global R&D Needs in Drying. Drying Technology, 25: 647-658.

Nishad, J.; Selvan, C. J.; Mir, S. A. and Bosco, S. J. D. (2017). Effect of Spray Drying on Physical Properties of Sugarcane Juice Powder (Saccharum Officinarum L.). J Food Sci Technol, 54: 687-697.

Saikia, Sangeeta; Mahnot, Nikhil Kumar and Mahanta, Charu Lata (2015). Effect of Spray Drying of Four Fruit Juices on Physicochemical, Phytochemical and Antioxidant Properties. Journal of Food Processing and Preservation, 39: 1656-1664.

Santhalakshmy, Swaminathan; Don Bosco, Sowriappan John; Francis, Sneha and Sabeena, Mallela (2015). Effect of Inlet Temperature on Physicochemical Properties of Spray-Dried Jamun Fruit Juice Powder. Powder Technology, 274: 37-43.

Schiffmann, Robert F. (2014). Microwave and Dielectric Drying. Handbook of Industrial Drying, Fourth Edition. 4th ed.: CRC Press.

Schulze, Dietmar (2008). Powders and Bulk Solids: Behaviour, Characterization, Storage and Flow, Springer.

Sobulska, Mariia and Zbicinski, Ireneusz (2021). Advances in Spray Drying of Sugar-Rich Products. Drying Technology, 39: 1774-1799.

Sokhansanj, Shahab and Jayas, Digvirs (2014). Drying of Foodstuffs. Handbook of Industrial Drying, Fourth Edition. CRC Press.

Sun, J.; Wang, W. L. and Yue, Q. Y. (2016). Review on Microwave-Matter Interaction Fundamentals and Efficient Microwave-Associated Heating Strategies. Materials, 9: 231.

Tan, L. W.; Ibrahim, M. N.; Kamil, R. and Taip, F. S. (2011). Empirical Modeling for Spray Drying Process of Sticky and Non-Sticky Products. 11th International Congress on Engineering and Food (Icef11), 1: 690-697.

Venkatesh, M. S. and Raghavan, G. S. V. (2004). An Overview of Microwave Processing and Dielectric Properties of Agri-Food Materials. Biosystems Engineering, 88: 1-18.

Vivek, Kambhampati; Mishra, Sabyasachi and Pradhan, Rama Chandra (2020). Characterization of Spray Dried Probiotic Sohiong Fruit Powder with Lactobacillus Plantarum. Lwt, 117: 108699.

Vogt, Gerald J and Unruh, Wesley P. Processing Aerosols and Filaments in a Tm010 Microwave Cavity at 2.45 Ghz. Microwave processing of materials III: symposium held April 27-May 1, 1992, 1992 San Francisco, California, USA. Materials Research Society, 245.

Wong, C. W.; Pui, L. P. and Ng, J. M. L. (2015). Production of Spray-Dried Sarawak Pineapple (Ananas Comosus) Powder from Enzyme Liquefied Puree. International Food Research Journal, 22: 6.

DOI: 10.51975/23380203som
Journal of the Nigerian Society of Chemical Engineers, 38(2), 2023

CHARACTERIZATION OF ZINC CHLORIDE MODIFIED ACTIVATED CARBON AND OTHER DERIVATIVE ADSORBENTS SYNTHESIZED FROM *VITEX DONIANA* SEED

***Francis, A. O.[1] and Otoikhian, S. K[2]**
[1, 2]*Department of Chemical Engineering, Edo State University, Uzairue, Nigeria*
[*]Email: francis.asokogene@edouniversity.edu.ng

ABSTRACT

This study evaluated the characteristics and adsorption performance of zinc chloride modified activated carbon ($VDZnCl_2$), its precursor (VDC), and sodium hydroxide (VDNaOH), hydrochloric acid (VDHCl) and thermally (VDT) modified adsorbents from vitex doniana. The adsorption performance of the adsorbents for methylene blue was in this order: $VDZnCl_2$ < VDNaOH < VDC < VDT < VDHCl. The $VDZnCl_2$ was characterized by Fourier transform infrared (FTIR), Brunauer-Emmett-Teller (BET), scanning electron microscope (SEM), energy-dispersive X-ray (EDAX) and thermal gravimetric analysis (TGA). The FTIR spectrum showed the presence of O—H group and characteristics C=C group generally found in carbonaceous materials. The BET surface area remarkably increased from 14.02 m^2/g to 933.25 m^2/g and pore size from 0.92 to 18.9 Å which reflected enhanced specific surface area and porous nature of the adsorbent, and its ability to facilitate pore fillings of many molecules inside its carbon matrix during adsorption. The SEM micrograph showed varieties of pores with widened cavities Therefore, $VDZnCl_2$ is a potential adsorbent substitute for wastewater treatment.

Key words: *Vitex doniana, characteristics, activated carbon, adsorption, carbonaceous materials*

1. INTRODUCTION

The growing trend of water contaminations resulting from growing population and industrialization are of great concern because they contaminate surface and ground water, and also render them unfit for drinking and irrigation when they are discharged into streams, oceans and lakes by chemical, textile and other allied industries (Piriya et al. 2021). These contaminants such as heavy metals, dyes etc. in water limit sunlight penetration into water and aeration of water body which impact negatively on photosynthesis and subsequently reduce the amount of dissolved oxygen in water (Piriya et al. 2021; Imran et al 2019). They also inject chemicals which leads to the death of most aquatic life, contamination of soils, poisoning of drinking water which results in numerous health issues like dyscrasia, leukocytosis, anemia, eye burn, damage to the liver, heart, spleen, kidney, lungs, bones and teratogenic effects (Alipour et al. 2019; Piriya et al. 2021).

Several treatment methods adopted for the removal of contaminants from wastewater include extraction, membrane separation, coagulation, ozonation, flocculation and adsorption (Asokogene et al. 2019; Aslam et al. 2017; Luo et al. 2017; Wang et al. 2017). Adsorption holds special place in the treatment of wastewater because of its low cost, effectiveness and ability to selectively enrich certain compounds (Asokogene et al. 2019; Pandey et al. 2020; Piriya et al. 2021). This has led researchers to develop low cost and readily available adsorbents from several synthetic and natural biomass.

Activated carbon has gained wide attention as brilliant adsorbent for the removal of aquatic pollutants due to its high surface area, stability, array of functional groups and excellent pore structures (Afshin et al. 2019). It is produced from several agricultural wastes such as empty fruit bunch (Zaini et al., 2016), woods (Nowicki, 2016) bamboo (Zhao et al. 2017), palm shells (Zhao et al. 2018), coconut shell (Singh et al. 2017), rich husk (Li et al. 2015), sawdust (Zhu et al. 2014), apricot stones (Djilani et al. 2015) and grape seeds (Okman et al. 2014) etc. by chemical or physical activation. Chemical activation enhances its specific surface area and porosity (Piriya et al. 2021). Zinc chloride has proven to be a better activating agent for most activated carbon adsorbent as it produces higher specific surface area and better adsorption results. For instance, $ZnCl_2$ activated carbon from sterculia gulata shells had adsorption capacity of 90.90 mg/g as against the precursor (sterculia gulata shells) of 45.45 mg/g (Rangabhashiyam and Selvaraju, 2015). Similarly, Zhang et al. 2020 also reported that $ZnCl_2$ impregnated activated carbon from rice husk at impregnation ratio of 1:1 had higher surface area than its precursor.

Consequently, *vitex doniana* seed, which are frequent waste in Nigeria (Ameh et al. 2012; Kapooria and Aime, 2005) and obtained from commonly grown *vitex doniana* tree has been limitedly synthesized as activated carbon adsorbent for Zn (II) and Pb (II) removal (Ameh et al. 2012) and as acid modified activated carbon for Cr (II) removal (Yusuf et al., 2020) from wastewater, but no study has been done on the synthesis of $ZnCl_2$ modified activated carbon from *vitex doniana* seed and its adsorption potential for dye (methylene blue) from wastewater. Therefore, this study was a first-time attempt of the synthesis of zinc chloride ($ZnCl_2$) modified activated carbon adsorbent from *vitex doniana*, removal of methylene blue dye from wastewater and comparing its adsorption performance its precursor, sodium hydroxide (NaOH), hydrochloric acid (HCl) and thermally modified ones, with the view to encourage its use as indigenous adsorbent for wastewater treatment, thus contributing to sustainable development goals. BET, SEM, EDX, FTIR and TGA were used to determine the properties of the adsorbent and its adsorption potential in batch mode was carried out on methylene blue removal from wastewater within a working concentration of 10 mg/L.

2. MATERIALS AND METHODS

2.1 Materials, reagent and instrument

Vitex doniana seeds were collected from Auchi Polytechnic community in Edo State. The chemicals used were of analytical grade: hydrochloric acid (37 %, Fisher Scientific, USA), methylene blue powder (98.5 %, BDH, England), Zinc chloride pellet (99%, Merck, Germany) and distilled water (Chemical Engineering laboratory, Auchi). Instruments used are analytical balance (Scout Pro, Ohaus, London, UK), pH meter (pH ep® pocket-sized pH meter, Hanna Instruments, Inc., USA), grinding mill (Biocotek, China), shaker (Ro-tap, England), stop watch (Quartz, China), Thermometer (Pyrex Technico, England), Fourier transform infrared (FTIR) spectrometer (Thermo Scientific, Nicolet ISI 10, USA), scanning electron microscope (SEM)/ energy dispersive analysis of x-ray (EDX) spectrophotometer (Karl Zeiss, Germany), Brunauer-Emmett-Teller (BET) surfer machine (Thermo Scientific, USA), thermogravimetric analyzer (Orton Simultaneous DTG/TGA, USA), UV-Vis spectrophotometer (Angstrom Advanced Inc, model 752, Massachusetts, USA) and muffle furnace (TT-EF-12, Techmel, USA).

2.2 Pre-treatment and synthesis of *vitex doniana* adsorbent

The exocarp and impurities of *vitex doniana* seed were washed off with running water. The seed was sun-dried for seven days, crushed, ground, and sieved to a size of 355 µm (Ameh et al. 2012). A 100 g each of the pulverized *vitex doniana* was treated thermally at 800 ^oC (Mistar et al. 2020), and chemically modified using $ZnCl_2$, sodium hydroxide (NaOH) and hydrochloric acid (HCl) by adding 0.5 M solution of each chemical to the pulverized samples in the ratio of 1:1 to form homogenize paste-like mixtures which were allowed to stay for 24 h for adequate impregnation. The mixtures were activated at 800 ^oC for 2 h in a TT-EF-12 muffle furnace (Techmel, USA). The resultant activated carbon samples were allowed to cool, washed with distilled water to a pH of 7, dried in the oven at 105^oC for 3 h and kept in a desiccator, except for $ZnCl_2$ modified sample which was soaked in HCl (3 wt%) for 12 h to remove surface ash before washing (Mkungunugwa et al. 2021; Mistar et al. 2020; Jaria et al. 2015; Khadiran et al., 2015). These adsorbents were designated as VDC, VDT, $VDZnCl_2$, VDNaOH and VDHCl for precursor, thermally treated, $ZnCl_2$ modified, NaOH modified and HCl modified *vitex doniana*, respectively.

2.3 Characterization of *vitex doniana* adsorbent

The surface functional groups of $VDZnCl_2$ and VDC (precursor) adsorbent samples were determined using FTIR analyzer (Thermo Scientific Nicolet ISI 10, USA) at wavenumber range of 4000-500 cm^{-1}. The textural properties were measured using a Thermo Scientific (USA) surface area analyzer. The SEM image of the adsorbent surface and texture was obtained by a Karl Zeiss (Germany) instrument. The thermal decomposition of the adsorbent sample was determined using the standard Orton simultaneous DTG/TGA analyzer, USA by recording the differential thermal couple output and balance output signal over temperature range of 30–1000^oC. The elemental composition of the adsorbent was also obtained using EDX as individual fluorescent energies detected were specific to the elements that were present in the sample.

2.4 Experimental procedure

For batch adsorption study, 1 g of methylene blue powder was dissolved in 1000 mL of distilled water to make stock solution and working concentration of 10 mg/L was prepared by dilution. In Beatson bottles, 50 mL of the concentration was added to 50 mg of the adsorbents. Next, the bottles were sealed, shaken, and

kept at 28°C for 72 h. The contact time was assumed to be long enough to achieve equilibrium adsorption (Asokogene et al. 2019). The residual concentrations were calculated by measuring absorbance at 620 nm with an Angstrom Advanced Inc. (model 752) scientific ultra violet-visible (UV-Vis) spectrophotometer. The pH of the methylene blue solution was kept at 4.8±0.3, as it should be. The adsorption capacity, q_e (mg/g), was determined from a mass balance equation,

$$q_e = \left(\frac{C_o - C_e}{m}\right) \times V \quad (1)$$

where $C_o$and C_e (mg/L) are the initial and equilibrium concentrations, respectively, V (L) is the volume of solution, and m (g) is the mass of the adsorbent.

3. RESULTS AND DISCUSSION

The batch adsorption plots to determine the best among the series of prepared adsorbents from *vitex doniana* (VDNaOH, $VDZnCl_2$, VDHCl, VDT and VDC) is presented in Figure 1. The result revealed that VDNaOH, $VDZnCl_2$, VDHCl, VDT and VDC adsorbents had adsorption capacities of 8.57 mg/g, 9.08 mg/g, 5.01 mg/g, 5.40 mg/g and 7.98 mg/g, respectively. In other words, the adsorption capacities were of this order: $VDZnCl_2$ < VDNaOH < VDC < VDT < VDHCl. This better adsorption performance demonstrated by $VDZnCl_2$ can be attributed to the creation of better active reaction sites for adsorption of methylene blue in $VDZnCl_2$ than VDNaOH, VDC, VDT and VDHCl (Ademiluyi and David-West, 2012).

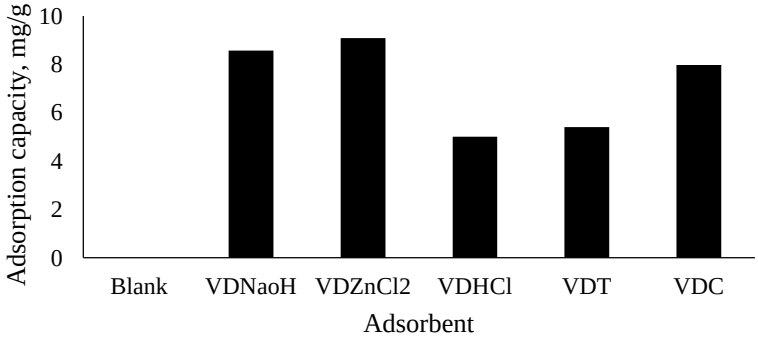

Figure 1: Vitex doniana adsorbents performance

The FTIR spectrum which gave insight into the surface functional groups and structure of $VDZnCl_2$ and VDC adsorbents over frequency range of 4000-500 cm^{-1} are presented in Figures 2 and 3. The signal at 3625–3605 cm^{-1} in the FTIR spectrum corresponds to intermolecular hydrogen bonding of polymeric compounds such as alcohols, phenols, and carboxylic acids, showing the presence of free hydroxyl groups on the adsorbent surface of $VDZnCl_2$ and VDC. Asymmetric and symmetric C—H bending vibrations of the —CH_2 and —CH_3 (alkanes) are associated with a peak at 3300 cm^{-1} of $VDZnCl_2$ while the peak at 2410.16 cm^{-1} corresponds to the CH_2 (alkanes) group of C—H symmetric stretching vibration for VDC. Furthermore, the C=C stretching vibration of alkenyl is the characteristic of a peak at 2611 cm^{-1} for $VDZnCl_2$. Meanwhile, C=O stretching vibration in aldehydes, ester or ketones, and carboxyl groups are indicated by the peaks at 1877 $cm^{-1}$and 1903.27 cm^{-1}, respectively of $VDZnCl_2$ and VDC.

Because of the carboxyl group, the peak at 1710.75 cm^{-1} corresponds to C—O stretching vibrations, while the C—O stretching vibrations in alcohol, ether, or hydroxyl groups correlate to the peak at 1150.28 cm^{-1} for VDC. The peak at 1551 cm^{-1} of $VDZnCl_2$ corresponds to C=C

stretching vibrations in the aromatic ring of alkenes, which are common in carbonaceous materials like activated carbon (Mkungunugwa et al. 2021). Finally, the peak at 1298 cm^{-1} of $VDZnCl_2$ belongs to C—H bending vibrations found in alkyl groups like CH_3, which are lignin-like.

The functional groups contained in $VDZnCl_2$ and VDC revealed that majority of the peaks in both adsorbent materials were comparable, with the exception of a peak at 1551.37 cm^{-1}, which corresponds to C=C stretching vibrations in the aromatic ring of alkenes and is commonly detected in carbonaceous materials like activated carbon (Mkungunugwa et al. 2021).

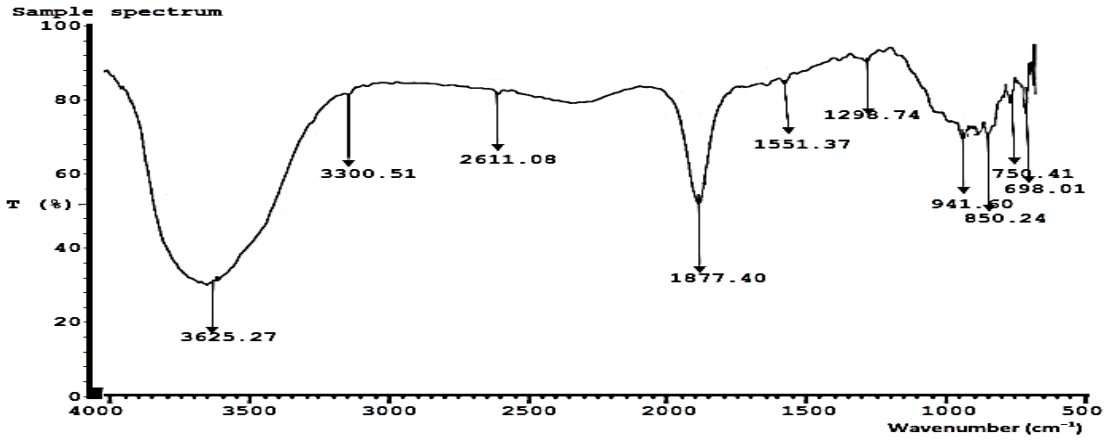

Figure 2: FTIR spectrum of zinc chloride modified vitex doniana activated carbon ($VDZnCl_2$)

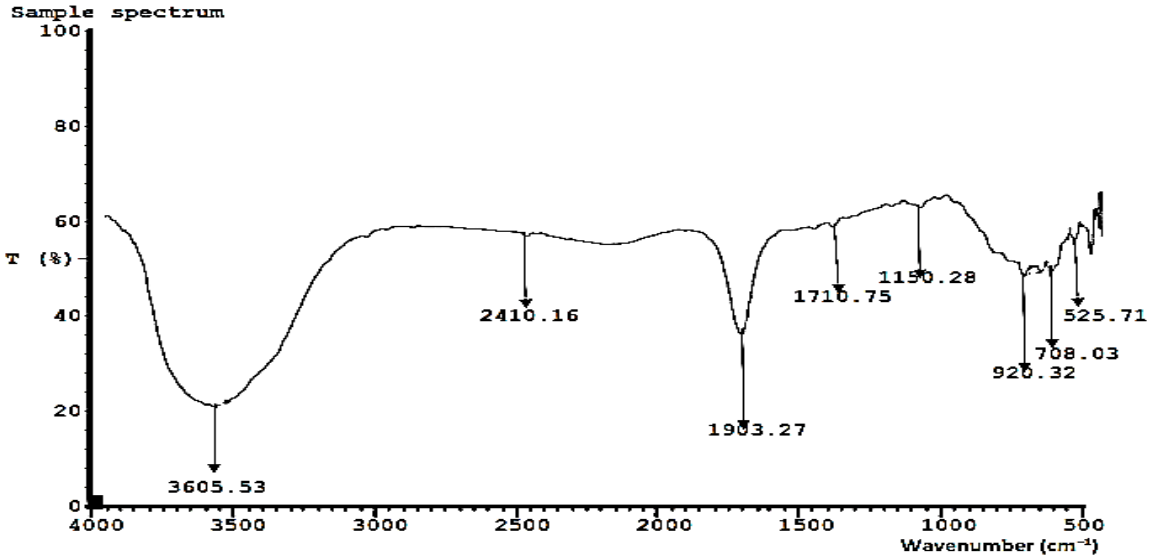

Figure 3: FTIR spectrum of vitex doniana precursor (VDC)

Table 1 summarizes the textural properties of $VDZnCl_2$ and VDC. The surface area of $VDZnCl_2$ increased dramatically from 14.0 to 933 m^2/g. The pattern is consistent with other raw materials upon activation (Mistar et al. 2020; Gonzalez, 2018). Accordingly, the pore volume increased by about three times, from 0.07 to 0.21 cm^3/g (Mistar et al. 2020; Sethia and Sayari, 2016). After activation, the pore size increased from 0.92 to 18.9 Å. Therefore, $VDZnCl_2$ will allow for pore fillings of numerous molecules inside its carbon matrix during adsorption ((Thommes et al. 2015; Mistar et al. 2020).

Table 1: Surface Textural Properties of $VDZnCl_2$ and VDC

BET Parameters	Samples	
	VDC	$VDZnCl_2$
Surface area ($m^2\ g^{-1}$)	14.02	933.25
Pore volume ($cm^3\ g^{-1}$)	0.0683	0.207
Pore size (A)	0.917	18.92

The SEM result of $VDZnCl_2$ adsorbent material which was characteristics of its surface morphology and texture at ×500 magnification is shown in Figure 4 and the EDX results of $VDZnCl_2$ and VDC are shown in Figures 5 (a) and (b), respectively.

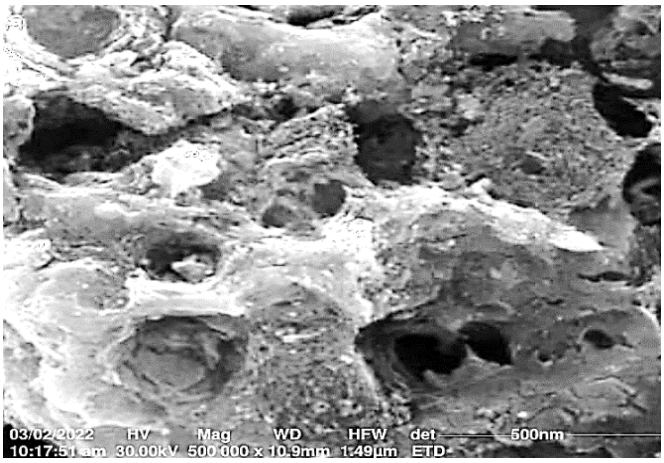

Figure 4: SEM micrograph of $VDZnCl_2$ adsorbent

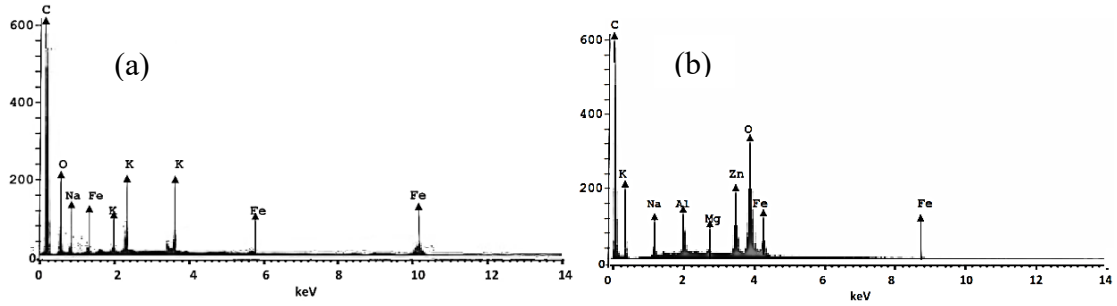

Figures 5: EDX analysis of (a) $VDZnCl_2$ adsorbent and (b) VDC adsorbent

The SEM micrograph of $VDZnCl_2$ adsorbent showed thin plant boundary walls due to modification and the presence of varieties of pores with widened cavities which could be due to the removal of volatile matter and production of fixed carbon after activation (Ohimor et al. 2021).

The EDX result revealed dominance of C and O in the precursor (VDC) and activated carbon adsorbent ($VDZnCl_2$). However, in VDC small proportion of Mg, Al, Ca and Zn were observed which were not present in $VDZnCl_2$. These elements would have been removed along with other volatile materials during activation at 800°C. Alam et al. 2017 reported similar result for activated carbon synthesized from *Eucalyptus lenceolata.*

The TGA/DTA result for $ZnCl_2$ based *vitex doniana* activated carbon, which was characteristics of its thermal behavior at regulated temperature is shown in Figure 6.

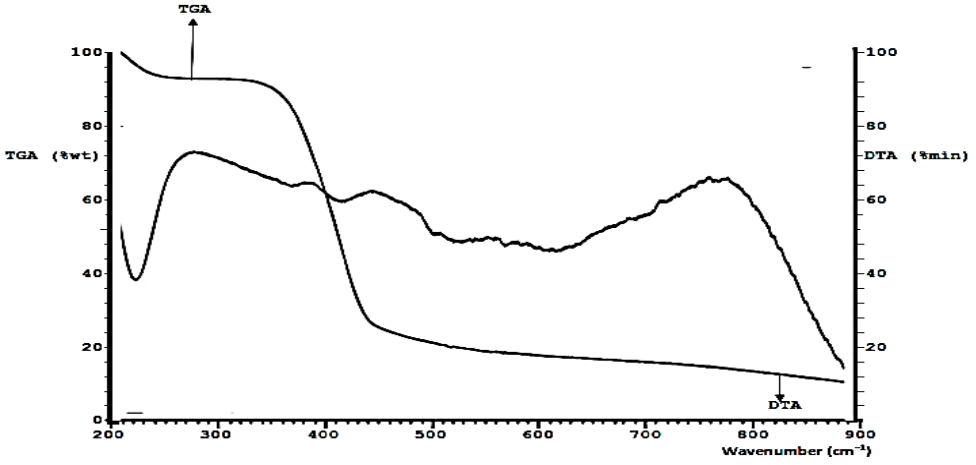

Figure 6: Thermal gravimetric profile of $VDZnCl_2$

The curves showed three steps weight loss (Figure 6) from 200 to 900^{o}C and 48.90 to 68%. The first weight loss within temperature range of 200-250^{o}C could be due to the eradication of water vapour and light volatile matter (Piriya et al. 2021). The second weight loss within temperature range of 350 to 500^{o}C could be as a result of liberation of organic constituents and other functional groups in the adsorbent. Finally, the less pronounced third weight loss within temperature range of 650 to 700^{o}C was probably due to heavy volatile matter eradication or disintegration of high strength configuration (Piriya et al. 2021). Nevertheless, decomposition of the adsorbent material occurred slowly from 200 to 900^{o}C with most of its fraction been lignin and residual traces of possibly cellulose and hemicellulose (Piriya et al. 2021; Cazetta et al. 2011).

4. CONCLUSION

Zinc chloride modified activated carbon adsorbent ($VDZnCl_2$) and other derivative adsorbents (VDC, VDT, VDNaOH and VDHCl) were synthesized from *vitex doniana* seeds which are common waste around Auchi Polytechnic community in Edo State. The adsorption performance of the adsorbents for methylene blue was in this order: $VDZnCl_2$ < VDNaOH < VDC < VDT < VDHCl. Therefore, $VDZnCl_2$ was characterized for its physicochemical properties. The presence of O—H group, characteristics C=C group generally found in carbonaceous materials, improved surface area and pores with widened cavities reflected its potential as adsorbent for methylene blue. The textural properties showed tremendous increase after modification from 14.0 to 933 m^2/g, the pore volume increased by about three times, from 0.07 to 0.21 cm^3/g and the pore size increased from 0.92 to 18.9 Å.

5. ACKNOWLEDGEMENT

We wish to acknowledge the scientific and financial support made by our 2022 project students and the department of Chemical Engineering laboratory of Auchi Polytechnic.

REFERENCES

Ademiluyi, F. T. and David-West, E. O. (2012). Effect of chemical activation on the adsorption of heavy metals using activated carbons from waste materials. *International Scholarly Research Network ISRN Chemical Engineering*, 674209, 1-6.

Afshin, S., Rashtbari, Y., Shirmardi, M., Vosoughi, M. and Hamzehzadeh, A. (2019). Adsorption of basic violet 16 dye from aqueous solution onto mucilaginous seeds of Salvia sclarea: kinetics and isotherms studies. *Desalination and Water Treatment* 161, 365–375.

Alam, S., Rehman, N., Amin, N., Shah, L. A., Mian, I. and Ullah, H. (2017). Removal of basic green 5 by carbonaceous adsorbent: adsorption kinetics. *Bulletin of Chemical Society Ethiopia,* 31(3), 411-422.

Alipour, M., Vosoughi, M., Mokhtari, S. A., Sadeghi, H., Rashtbari, Y., Shirmardi, M. and Azad, R. (2019). Optimising the basic violet 16 adsorption from aqueous solutions by magnetic graphene oxide using the response surface model based on the Box–Behnken design. *International Journal of Environmental Analytical Chemistry.*

Ameh, P. O., Odoh, R. and Oluwaseye, A. (2012). Equilibrium study on the adsorption of Zn (II) and Pb (II) ions from aqueous solution onto *vitex doniana* nut. *International Journal of Modern Chemistry*, 3(2): 82-97

Aslam, S., Zeng, J., Subhan, F., Li, M., Lyu, F., Li, Y. and Yan, Z. (2017). In-situ one-step synthesis of Fe_3O_4 @ MIL-100 (Fe) core-shells for adsorption of methylene blue from water. *Journal of Colloid and Interface Science* 505, 186–95.

Asokogene, F. O., Muhammad, A. A. Z., Misau, M. I., Surajudeen, A. and El-Nafaty, A. U. (2019). Methylene blue adsorption onto neem leave/chitosan aggregates: isotherm, kinetics and thermodynamics studies. *International Journal of Chemical Reactor Engineering.* pp 1-16.

Cazetta, A. L., Vargas, A. M. M., Nogami, E. M., Kunita, M. H., Guilherme, M. R., Martins, A. C., Silva, T. L., Moraes, J. C. G. and Almeida, V. C. (2011). NaOH-activated carbon of high surface area produced from coconut shell: kinetics and equilibrium studies from the methylene blue adsorption. *Chemical Engineering Journal* 174 (1), 117–125.

Djilani, C., Zaghdoudi, R., Djazi, F., Bouchekima, B., Lallam, A., Modarressi, A. and Rogalski, M. (2015). Adsorption of dyes on activated carbon prepared from apricot stones and commercial activated carbon. *Journal of Taiwan Institute of Chemical Engineering* 53, 112–121.

Kapooria, R. G. and Aime, M. C. (2005). Report of oliver scitula on *vitex doniana* in Zambia. *Africa Journal of Science and Technology,* 3: 57-60.

González P. G. (2018). Activated carbon from lignocellulosics precursors: a review of the synthesis methods, characterization techniques and applications. *Renewable and Sustainable Energy Rev.*, 82(1), 1393–1414.

Imran, M., Islam, A. U., Tariq, M. A., Siddique, M. H., Shah, N. S., Khan, Z. U. H., Amjad, M., Din, S. U., Shah, G. M., Naeem, M. A., Nadeem, M., Nawaz, M. and Rizwan, M. (2019). Synthesis of magnetite-based nanocomposites for effective removal of brilliant green dye from wastewater. *Environmental Science and Pollution Research* 26 (24), 24489–24502.

Jaria, G., Calisto, V., Gil, M. V., Otero, M. and Esteves, V. I. (2015). Removal of fluoxetine from water by adsorbent materials produced from paper mill sludge. *Journal of Colloid and Interface Science* 448, 32–40.

Khadiran, T., Hussein, M. Z., Zainal, Z. and Rusli, R. (2015). Textural and chemical properties of activated carbon prepared from tropical peat soil by chemical activation method. *Bioresources* 10 (1), 986–1007.

Li, W., Ma, T., Zhang, R., Tian, Y. and Qiao, Y. (2015). Preparation of porous carbons with high and low pressure CO_2 uptake by KOH activation of rice husk char. *Fuel* 139, 68–70.

Luo, L., Wu, X., Li, Z., Zhou, Y., Chen, T., Fan, M. and Zhao, W. (2019). Synthesis of activated carbon from biowaste of fir bark for methylene blue removal. *Royal Society Open Science* 6(190523), 1-14

Luo, X. P., Fu, S. Y., Du, Y. M., Guo, J. Z. and Li, B. (2017). Adsorption of methylene blue and malachite green from aqueous solution by sulfonic acid group modified MIL-101. *Microporous and Mesoporous Materials* 237, 268–274.

Mistar, E. M., Alfatah, T. and Supardan, M. D. (2020). Synthesis and characterization of activated carbon from bambusa vulgaris striata using two-step KOH activation. *Journal of Materials Research and Technology*, 9 (3), 6278-6286.

Mkungunugwa, T., Manhokwe, S., Chawafambira, A. and Shumba, M. (2021). Synthesis and characterization of activated carbon obtained from marula (sclerocarya birrea) nutshell. *Journal of Chemistry* https://doi.org/10.1155/2021/5552224

Nowicki, P. (2016). Effect of heat treatment on the physicochemical properties of nitrogen enriched activated carbons. *Journal of Thermal Analysis and Calorimetry* 125 (3), 1017-1024.

Ohimor, E. O., Temisa, D. O. and Ononiwu, P. I. (2021). Production of activated carbon from carbonaceous agricultural waste material: coconut fibres. *Nigerian Journal of Technology*, 40 (1), 19-24.

Okman, I., Selhan, K., Tay, T. and Erdem, M. (2014). Activated carbons from grape seeds by chemical activation with potassium carbonate and potassium hydroxide. *Applied Surface Science* 293, 138-142.

Pandey, S., Do, J. Y., Kim, J. and Kang, M. (2020). Fast and highly efficient catalytic degradation of dyes using κ-carrageenan stabilized silver nanoparticles nanocatalyst. *Carbohydrate Polymers* 230, 115597.

Piriya, R. S., Jayabalakrishnan, R. M., Maheswari, M., Boomiraj, K. and Oumabady, S. (2021). Coconut shell derived $ZnCl_2$ activated carbon for malachite green dye removal. *Water Science & Technology* in press. pp. 1-16

Rangabhashiyam, S. and Selvaraju, N. (2015). Adsorptive remediation of hexavalent chromium from synthetic wastewater by a natural and $ZnCl_2$ activated Sterculia guttata shell. *Journal of Molecular Liquids*, 207, 39-49.

Sethia, G. and Sayari A. (2021). Activated carbon with optimum pore size distribution for hydrogen storage. *Nigerian Journal of Technology* 40 (1),19–24.

Singh, G., Kim, I. Y., Lakhi, K. S, Srivastava, P., Naidu, R. and Vinu, A. (2017). Single step synthesis of activated bio-carbons with a high surface area and their excellent CO_2 adsorption capacity. *Carbon* 116, 448–455.

Thommes, M., Kaneko, K., Neimark, A. V., Olivier, J. P., Reinoso, F. R., Rouquerol, J. et al. (2015). Physisorption of gases, with special reference to the evaluation of surface area and pore size distribution (IUPAC Technical Report). *Pure and Applied Chemistry*, 87:1051–1069.

Wang, F., Zhang, L., Wang, Y., Liu, X., Rohani, S. and Lu, J. (2017). Fe_3O_4 @ SiO_2 @ CS-TETA functionalized graphene oxide for the adsorption of methylene blue (MB) and Cu (II). *Applied Surface Science,* 420, 970–981.

Zaini, M. A. A., Shu-Hui, T., Lin-Zhi, L. and Alias, N. (2016). Fate of chemical activators in the aqueous environment: What should we do

about it? *Aceh International Journal of Science and Technology* 5(1), 18-20.

Zhang, S., Zhu, S., Zhang, H., Liu, X. and Xiong, Y. (2020). Synthesis and characterization of rice husk-based magnetic porous carbon by pyrolysis of pretreated rice husk with $FeCl_3$ and $ZnCl_2$. *Journal of Analytical and Applied Pyrolysis* 147, 104806.

Zhao, H., Zhong, H., Jiang, Y., Li, H., Tang, P., Li, D. and Feng, Y. (2022). Porous $ZnCl_2$-activated carbon from Shaddock peel: methylene blue adsorption behavior. *Materials*, 15(895), 1-16

Zhao, W., Luo, Lu., Wang, H. and Fan, M. (2017). Synthesis of bamboo-based activated carbons with super-high specific surface area for hydrogen storage. *Bioresources* 12, 1246–1262.

Zhao, W., Luo, L., Chen, T., Li, Z., Zhang, Z. and Fan, M. (2018). Activated carbons from oil palm shell for hydrogen storage. *Material Science Engineering*, 368, 012031.

Zhu, X., Wang, P., Peng, C., Yang, J. and Yan, X. (2014). Activated carbon produced from paulownia sawdust for high-performance CO_2 sorbents. *Chin. Chem. Lett.* 25, 929–932.

DOI: 10.51975/23380204som
Journal of the Nigerian Society of Chemical Engineers, 38(2), 2023

EXTRACTION OF KERATIN PROTEIN FROM CHICKEN FEATHERS: AN OPTIMIZATION STUDY

Kayode, F. O.[1], Aderemi, B.[2], and **[*]Falowo, O. A.**[3]
[1,2,3]*Department of Chemical Engineering, Landmark University Omu-Aran, Nigeria.*
[1]kayode.favour@lmu.edu.ng, [2]aderemi.benjamin@lmu.edu.ng, [3] falowo.olayomi@lmu.edu.ng
[*]Corresponding author: falowo.olayomi@lmu.edu.ng

ABSTRACT

Box-Behnken design was used to model, optimize and examine the interplay of the process variables affecting the extraction of keratin protein. The variables used in the experimental design were temperature (70°C - 90°C), extraction time (2-8 hrs), liquid-solid ratio (5-20 ml/g), and concentration of sodium sulfide (8-50 g/l). A biuret test was carried out on extracted keratin and Fourier Transform Infrared Spectroscopy (FTIR) and Scanning Electron Microscopy (SEM) were used to characterize the extracted keratin. The extraction was done and the biuret test confirmed that the extract was indeed protein. From the FTIR analysis, the presence of functional groups such as amino and carbonyl groups confirmed the presence of a protein backbone in the extracted keratin. The micrograph from the SEM analysis compared the appearance of keratin and the feather residue after keratin extraction. The optimal process conditions established for the keratin protein extraction are a temperature of 72℃, an extraction time of 2 hrs, a liquid-solid ratio of 5 ml/g, and a sodium sulfide concentration of 20.614 g/l. These conditions generated a protein yield of 86.92 wt.%.

Keywords: *Optimization, Keratin protein, Chicken feathers, Characterization, Extraction.*

1. INTRODUCTION

One of the most abundant proteins in the bodies of mammals, birds, and reptiles is keratin. It is found in feathers, wool, horn, and nails and gives the body its strength. All keratins have an underlying structure made up of α-helices and β-pleated sheets, and the cysteine in their backbones promotes the production of robust disulfide bonds that facilitate the construction of the helix and pleated sheets as well as the coiled-coil structure (Khan et al., 2017). It was eventually determined that keratin comes in two varieties, type I and type II, which can be differentiated by their variations in secondary structures (Rouse & Van Dyke, 2010). The richest source of keratin is found in the skin and its appendages, including nails, hair, feathers, wool, hooves, scales, and stratum corneum (Shah et al., 2019). Keratin, a filamentous protein, can be used for a variety of purposes as a result of its good biodegradability, biocompatibility, cell adhesion performance, strong polarity, and high chemical activity, among other properties (Shavandi et al., 2017). Nowadays, the most popular and desirable usage of this protein is in hair cosmetics, for example, keratin serum, shampoos, and conditioners are now being utilized extensively to restore hair damage. Due to its filamentous shape, keratin is used in tissue engineering and controlled-release applications as a source of natural and synthetic biomaterial (Rajabi et al., 2020). Also, keratin is more stable and less soluble than the majority of other proteins (Donato & Mija, 2019). This characteristic makes the dissolution and extraction of keratin a difficult process compared to other natural polymers. Feather keratin is a potential source of cheap, eco-friendly, and commercial biomaterial (Anbesaw, 2022). The processing of chicken meat for human consumption produces approximately 5 million tons of feathers per year as a waste stream (Šafarič et al., 2020). Chicken feathers consist of about 90% keratin and can be utilized for industrial applications (Kumawat et al., 2018). Recently, industrial applications of keratin led to the development of several means of keratin extraction as well as its modification for improved performance. The major methods used to isolate keratin from keratin-rich materials are alkali extraction, chemical hydrolysis, microwave irradiation, steam explosion, sulfitolysis, reduction, oxidation, and ionic liquids (Reddy et al., 2021). The reduction of disulfide bonds using mercaptoethanol (MEC) has been the standard method for keratin extraction with a good yield of keratin (Vineis et al., 2019). However, MEC is a toxic chemical and is undesirable commercially and environmentally due to its high cost and issues related to its toxicity to the environment, as such, it is rarely used. Sodium sulfide can be a good alternative to break down the

sulfide bonds and extract keratin. This method of sulfitolysis has major industrial and analytical impacts on chicken feather processing as it prevents complete liquefaction of the substrate as well as pollutant reduction (Laba and Szczekala, 2013). Therefore, knowing the optimum sodium sulfide concentration and other process variables impacting keratin extraction is vital.

Optimization of the process variables influencing keratin extraction will aid keratin protein production by establishing optimum conditions for large-scale application. The extraction of keratin protein from chicken feathers could be a strategic method to convert waste to wealth. Harnessing chicken feathers technologically solves its waste disposal problem and offers the possibility of novel products from chicken feathers. There is a need to improve the extraction process at higher reducing agent concentrations with the inclusion of liquid-solid ratios with the aim of increasing the keratin yield. This research is in tandem with the Sustainable Development Goal (SDG) 9, which is to build resilient infrastructure, promote inclusive and sustainable industrialization and foster innovation.

2. MATERIALS AND METHODS

2.1. Materials

The Chicken Feathers used in this study were obtained from a poultry farm in Omu-Aran and conveyed to the Chemical Engineering Laboratory, Landmark University, Omu-Aran, Kwara State. The chemicals and reagents used were all of the analytical grade (AG).

2.2. Methods

2.2.1. Chicken Feather Pre-treatment *(Oluba et al., 2021)*

The feathers were pre-treated following a modification of the method proposed by Oluba *et al*. (2021). The feathers were cleaned by washing with warm water and were disinfected by soaking in sodium hypochlorite, rinsed, and then air dried for 36 hrs. Then, the feathers were soaked in ethanol for 24 hrs, washed with detergent, and rinsed thoroughly with water. The washed feathers were oven dried at 60℃ for 24 hrs. Thereafter, the dried feathers were grounded into fine particles and stored for further use.

2.2.2. Experimental Design and Optimization of Keratin Protein Extraction Process

Optimization of keratin extraction was done using design expert software (version 12), and the Box-Behnken design model was used for the optimization of the extraction of the keratin process. The four independent variables and the ranges investigated are presented in Table 1.

Table 1: Variables for the experimental design

Factors (Independent variable)	Factors level		
	-1	0	1
Time (h)	2	5	8
Temperature (℃)	70	80	90
Concentration (g/l)	8	29	50
Liquid-Solid ratio	5	12.5	20

Twenty-nine experimental runs were generated with the keratin protein amount as the response. The experimental data were fitted into a polynomial quadratic model equation.

2.2.3. Keratin Protein Extraction Process

The extraction process was carried out according to the experimental run generated. A known amount of the milled feather was weighed and added to a known volume of Na_2S solution to form the liquid-solid ratio. The pH of the solution ranged between 12 and 13. The mixture was placed in 250 ml beakers with a foil seal on the top and then mechanically shaken on a desktop shaker for homogeneous mixing. Thereafter, it was placed in a water bath set to the appropriate temperature. The reaction time was imputed and varied according to the values generated by the experimental design. After cooling, the turbid solution was filtered using a muslin cloth to obtain the filtrate. The filtrate obtained was precipitated with 10% trichloroacetic acid (Sigma-Aldrich, UK). The precipitate was filtered out with a muslin cloth and washed under water. The precipitated keratin was oven-dried at 40^{o}C for 15 hrs. The dried keratin was pulverized using a mortar and pestle and then stored for further analysis.

The yield of Keratin obtained was calculated using

$$Keratin\ yield = \frac{Wi}{Wo} \times 100 \quad (1)$$

Where, Wi is the weight of the initial feather used as calculated from the liquid-solid ratio and Wo is the weight of recovered keratin.

2.2.4. Biuret Test for Extracted Keratin Protein

The extracted keratin underwent a Biuret test. The resulting solution from the biuret test was analyzed under UV-vis to obtain its absorbance at a wavelength of 540 nm.

2.2.5. Characterization of Extracted Keratin and Feather Residue

The extracted keratin collected after purification was analyzed using the FTIR to examine the functional groups present in the extract. Also, extracted keratin and the feather residue left after the extraction were analyzed using the scanning electron microscope to evaluate their surface structures (Oluba *et al., 2021*).

3. RESULTS AND DISCUSSIONS

3.1. Pre-treatment of Waste Chicken Feathers

The feathers which were initially brown in color and produced an offensive odor became white and odorless upon pre-treatment. The addition of sodium hypochlorite for cleaning made the feathers white and upon ethanol addition, made them even whiter.

3.2. ANOVA Results of the keratin Extraction from Feathers

The results obtained from the conduction of keratin extraction from chicken feathers was presented in Table 2. Run 27 has the highest keratin recovery from the chicken feather while the lowest keratin protein was obtained in run 10.

Table 2: Box Behnken design of process variables and keratin yield

Run	Temp (°C)	Conc (g/l)	Time (h)	Liquid/Solid ratio	Keratin Yield (%)
1	70.00	50.00	5.00	12.5	24.875
2	90.00	29.00	2.00	12.5	53.125
3	80.00	8.00	8.00	12.5	35.750
4	80.00	29.00	5.00	12.5	41.500
5	80.00	8.00	2.00	12.5	68.130
6	80.00	29.00	8.00	5.00	56.800
7	90.00	29.00	8.00	12.5	19.250
8	80.00	50.00	8.00	12.5	16.125
9	80.00	29.00	5.00	12.5	41.500
10	80.00	50.00	5.00	20.00	3.400
11	80.00	50.00	5.00	5.00	45.800
12	80.00	29.00	5.00	12.5	41.500
13	70.00	8.00	5.00	12.5	60.250
14	80.00	50.00	2.00	12.5	52.875
15	80.00	8.00	5.00	20.00	47.200
16	80.00	8.00	5.00	5.00	26.500
17	90.00	29.00	5.00	5.00	62.850
18	70.00	29.00	2.00	12.50	61.625
19	80.00	29.00	2.00	5.00	72.400
20	80.00	29.00	2.00	20.00	50.000
21	70.00	29.00	8.00	12.50	40.500
22	80.00	29.00	5.00	12.50	41.500
23	90.00	8.00	5.00	12.50	38.125
24	80.00	29.00	8.00	20.00	21.400
25	90.00	50.00	5.00	12.50	13.000
26	80.00	29.00	5.00	12.50	41.500
27	70.00	29.00	5.00	5.00	73.450
28	90.00	29.00	5.00	20.00	20.200
29	70.00	29.00	5.00	20.00	42.600

The analysis of variance (ANOVA) shows that the model as well as the process variables (Liquid solid ratio, temperature, time, and solvent concentration) were significant. Any model term having a p-value ≤ 0.05 indicates that the parameter is significant (Table 3). The **Model also has an F-value** of 21.88 which implies that there is only a 0.01% chance that an F-value this large could occur due to noise. Hence, this model's F-value further showed its significance. In this case, A, B, C, D, BD, and B^2 are significant model terms.

Table 3: Analysis of Variance for Reduced Quadratic model of Keratin Extraction

Source	Sum of Squares	df	Mean Square	F-value	p-value	
Model	7985.48	6	1330.91	21.88	< 0.0001	significant
A-Temp	780.05	1	780.05	12.82	0.0017	
B-Conc	1197.50	1	1197.50	19.69	0.0002	
C-Time	2361.11	1	2361.11	38.82	< 0.0001	
D-L/S ratio	1950.75	1	1950.75	32.07	< 0.0001	
BD	995.40	1	995.40	16.36	0.0005	
B^2	700.68	1	700.68	11.52	0.0026	
Residual	1338.23	22	60.83			
Lack of Fit	1338.23	18	74.35			
Pure Error	0.0000	4	0.0000			
Cor Total	9323.72	28				

Table 4 shows the adequate precision measure of 19.644. **Adequate Precision** measures the signal-to-noise ratio. A ratio greater than 4 is desirable. This means that the model had a strong signal to be used for optimization. The **Predicted R^2** of 0.6651 is in reasonable agreement with the **Adjusted R^2** of 0.8173; i.e. the difference is less than 0.2.

Table 4: Fits Statistics

Fits	Values
Std. Dev.	7.80
Mean	41.85
C.V. %	18.64
R^2	0.8565
Adjusted R^2	0.8173
Predicted R^2	0.6651
Adeq Precision	19.6439

3.3. Final Equation in Terms of Coded Factors

The coefficient estimates were used to formulate the model equation

$$\text{Keratin yield}(\%) = 45.98 - 8.06A - 9.99B - 14.03C - 12.75D - 15.78BD - 9.98B^2 \quad (2)$$

Where A, B, C, and D are temperature concentration, time, and liquid-solid ratio, respectively. The equation in terms of coded factors can be used to make predictions about the response for given levels of each factor. By default, the high levels of the factors are coded as +1 and the low levels are coded as -1. The coded equation is useful for identifying the relative impact of the factors by comparing the factor coefficients.

3.4 Graphical Plots

A normal probability plot of the residuals is a scatter plot with the theoretical percentiles of the normal distribution on the x-axis and the sample percentiles of the residuals on the y-axis. The normal plot of residuals (Figure 1) and the plot of predicted vs. actual (Figure 4) both indicated a straight line. This means there is a close agreement between the actual and predicted response.

DOI: 10.51975/23380204som
Journal of the Nigerian Society of Chemical Engineers, 38(2), 2023

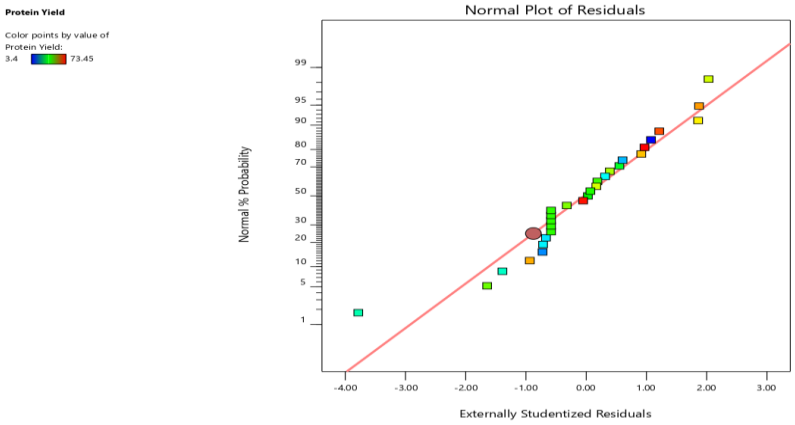

Figure 1: Normal Plot of Residuals Against Studentized residuals

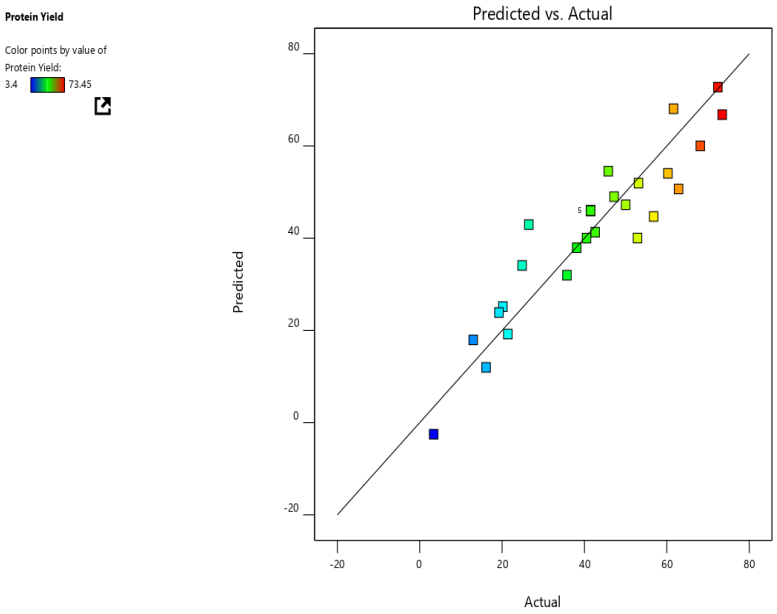

Figure 2: A Plot of Predicted against Actual keratin protein

The interactive effects of the process variables on the keratin yield (%) were examined using a three-dimensional surface curve (3D) against any two-independent variable while keeping the other variable constant. The 3D- graphs represent the effects of the independent variables and their interactions on the keratin yield. Where Figure 3 shows the effect of the concentration of sodium sulfide and reaction temperature on the amount of keratin extracted. This plot shows that an increase in concentration along with increasing temperature initially leads to an increase in the keratin yield but after a certain point, further increase of concentration and temperature to the highest level resulted in a decrease in protein yield. Figure 4 represents the effects of Sodium sulfide's concentration and liquid-solid ratio on keratin yield. The plot shows that the keratin yield is majorly influenced by the changes in sulfide concentration, though a marginal increase was observed with an increase in Liquid -solid

ratio. Interaction between these two variables clearly shows that concentration has a more domineering effect on the protein yield compared to the Liquid-solid ratio.

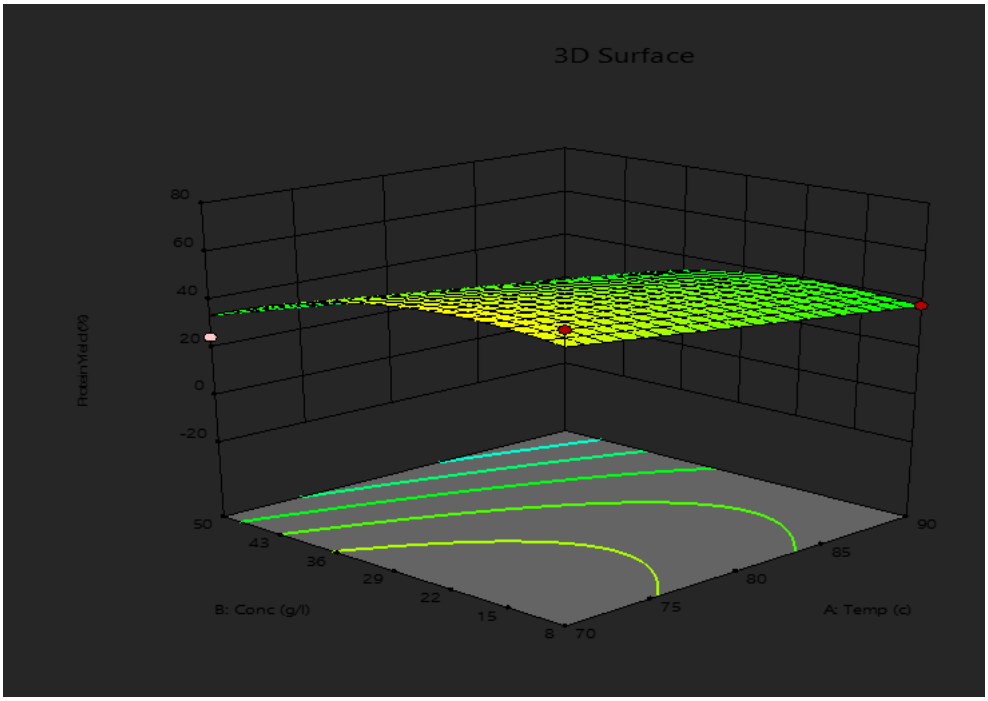

Figure 3: 3-D Response Surface Plot for the interaction of Temp and Concentration

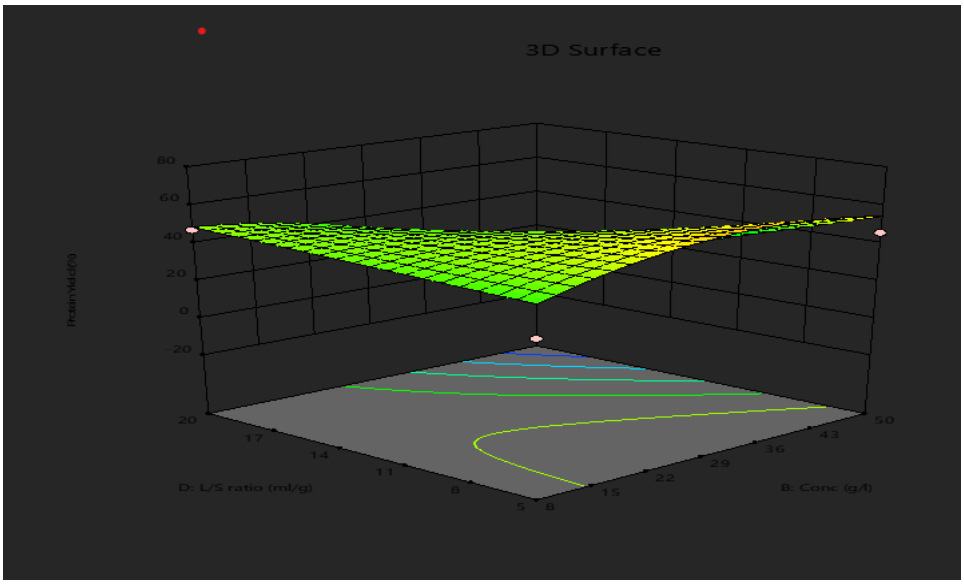

Figure 4: 3-D Response Surface Plot for the interaction of Concentration and L/S Ratio

3.4. Validation of Experiment

The optimal conditions predicted from the optimization of keratin protein extraction were a temperature of 72 ^{o}C, Time of 2 h, L/S ratio of 5 ml/g, and Concentration of 20.614 g/l. The experiment was carried out at these optimal conditions to validate the predicted optimal values. At these optimum conditions, the keratin yield was 86.92 w% which was higher than the highest keratin yield from the experimental runs.

3.5. Protein Characterization

The biuret test conducted on the extract from all 29 experimental runs indicates a purple color change in the final sample which confirmed the presence of protein in all the samples. The protein amount of each sample was obtained using a UV spectrophotometer following the method developed by Reinhold in 1953.

3.6. Structural Analysis of the Extract by FTIR

Figure 5 shows the results from the FTIR analysis. The FTIR characterization of keratin extracts has characteristic peaks corresponding to important functional groups like -CO-NH-, -NH_2, -CNH, -C-H. The relatively broad peak in the region of 3314.552 cm^{-1} corresponds to hydrogen-bonded -N-H and -O-H stretching motion out of amide functionality and absorbed water. The less intense peak in the region of 2900-3100 cm^{-1} signifies -C-H and -N-H groups stretching vibrations. The carbonyl group of amide functionality occurs in the region of 1600-1700 cm^{-1}. An observed peak at 1675.355 cm^{-1} is assigned to amide carbonyl (-C=O) functional group stretching vibration. The observed peak at 1334.499 cm-1 corresponds to the -CNH group comprising -C-N- and -C-C- groups stretching vibrations and -N-H group bending vibration. The bending vibration of the -CH_2 group occurred at 1452.65 cm^{-1}. The intense sharp peak at 1532.649 cm-1 corresponds to the -C-N-H group bending vibration. These results showed the presence of characteristic peaks like amide -N-H, -C=O, -C-N- and -CNH functionalities which confirm building block amino acids forming peptide groups of keratin protein.

3.8. SEM Analysis

The SEM micrograph shown in Figure 6 indicated a compact porous-like structure for the extracted keratin (Figure 6a and Figure 6b) compared to the feather residue which showed a thread-like microstructure (Figure 7a and Figure 7b). The feather residue void of keratin did not indicate any form of porosity in its structure.

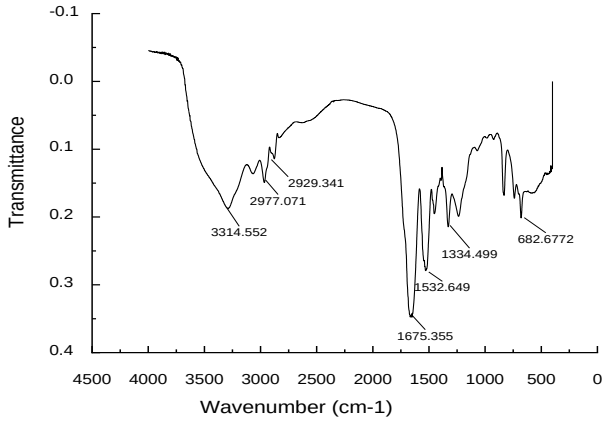

Figure 5: FTIR Analysis of extracted Keratin protein

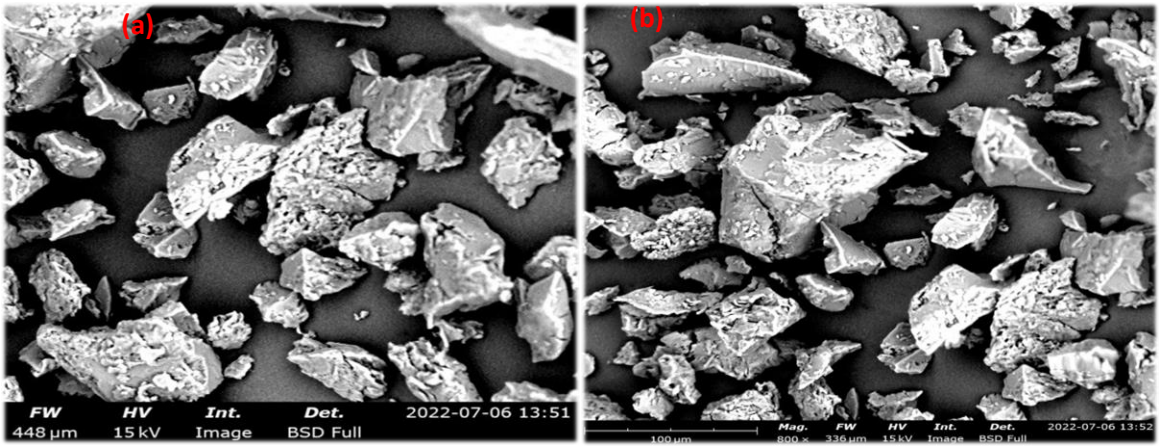

Figure 6: SEM Micrograph for (a) keratin 600x (b) Keratin 800x

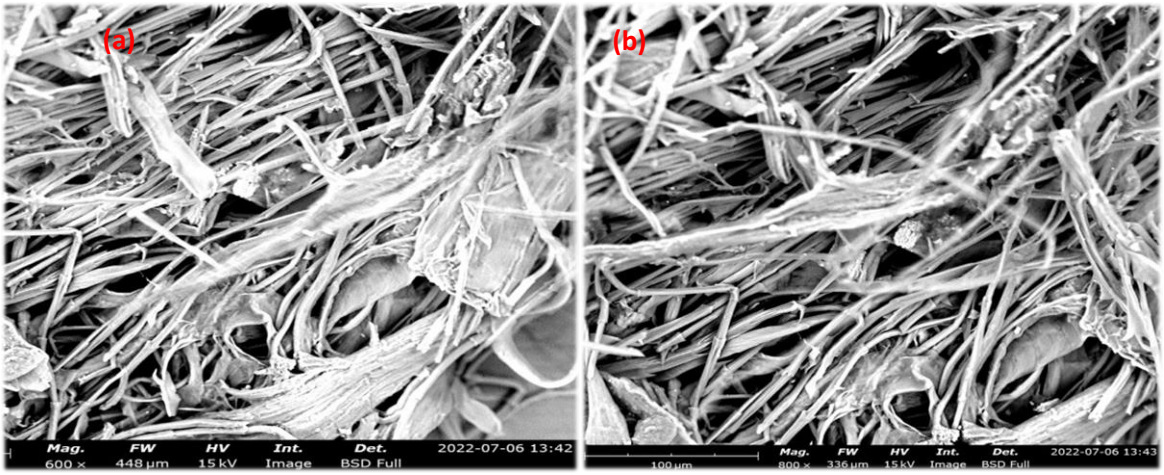

Figure 7: SEM Micrograph for (a) Feather Residue 600x (b) Feather Residue 800x

4. CONCLUSION

The optimal process conditions established for keratin extraction were time: 2 hrs, temperature: 72^{o}C, liquid-ratio: 5 ml/g, and sodium sulfide concentration: 20.614 g/l respectively with a corresponding yield of 86.92 wt% of keratin protein. The results of the FT-IR analysis revealed that amino and carbonyl groups were the active functional groups present, which further confirmed that the extract obtained was made up of protein. The SEM micrograph indicated a compact microstructure for keratin while the feather residue showed a thread-like microstructure. The establishment of optimal process parameters could facilitate large-scale extraction of keratin for industrial applications.

ACKNOWLEDGEMENTS

The authors appreciate the contribution of Prof Olarewaju Oluba of the Department of Biochemistry and the technologists in the Department of Chemical Engineering, Landmark University for their technical assistance.

REFERENCES

Anbesaw, M. S. (2022). Bioconversion of Keratin Wastes Using Keratinolytic Microorganisms to Generate Value-Added Products. *International Journal of Biomaterials*, *2022*.

Donato, R. K., & Mija, A. (2019). Keratin associations with synthetic, biosynthetic and natural polymers: An extensive review. *Polymers*, *12*(1), 32.

Khan, R. H., Siddiqi, M. K., & Salahuddin, P. (2017). Protein structure and function. *Basic biochemistry*, *5*, 1-39.

Kumawat, T. K., Sharma, A., Sharma, V., & Chandra, S. (2018). Keratin waste: the biodegradable polymers. In *Keratin*. IntechOpen.

Łaba, W., & Szczekała K. B., (2013). Keratinolytic Proteases in Biodegradation of Pretreated Feathers. *Pol. Journal. Environ. Stud.*, 22, (4), 1101-1109

Oluba, O. M., Osayame, E., & Shoyombo, A. O. (2021). Production and characterization of keratin-starch bio-composite film from chicken feather waste and turmeric starch. *Biocatalysis and Agricultural Biotechnology*, *33*, 101996.

Rajabi, M., Ali, A., McConnell, M., & Cabral, J. (2020). Keratinous materials: Structures and functions in biomedical applications. *Materials Science and Engineering: C*, *110*, 110612.

Reddy, C. C., Khilji, I. A., Gupta, A., Bhuyar, P., Mahmood, S., AL-Japairai, K. A. S., & Chua, G. K. (2021). Valorization of keratin waste biomass and its potential applications. *Journal of Water Process Engineering*, *40*, 101707.

Rouse, J. G., & Van Dyke, M. E. (2010). A review of keratin-based biomaterials for biomedical applications. *Materials*, *3*(2), 999-1014.

Šafarič, R., Fras Zemljič, L., Novak, M., Dugonik, B., Bratina, B., Gubeljak, N., Bolka, S., & Strnad, S. (2020). Preparation and characterisation of waste poultry feathers composite fibreboards. *Materials*, *13*(21), 4964.

Shah, A., Tyagi, S., Bharagava, R. N., Belhaj, D., Kumar, A., Saxena, G., Saratale, G. D., & Mulla, S. I. (2019). Keratin production and its applications: a current and future perspective. *Keratin as a protein biopolymer*, 19-34.

Shavandi, A., Silva, T. H., Bekhit, A. A., & Bekhit, A. E.-D. A. (2017). Keratin: dissolution, extraction and biomedical application. *Biomaterials science*, *5*(9), 1699-1735.

Vineis, C., Varesano, A., Varchi, G., & Aluigi, A. (2019). Extraction and characterization of keratin from different biomasses. In *Keratin as a protein biopolymer* (pp. 35-76). Springer.

DOI: 10.51975/23380205som
Journal of the Nigerian Society of Chemical Engineers, 38(2), 2023

FLOW AND COMPACTION PROPERTIES OF EXCIPIENTS DEVELOPED FROM BIOPOLYMER WASTE SNAIL SHELL AND INFLUENCING FACTORS

[*]Adeoye, B. K.[1], Aransiola, E. F[2], Alebiowu, G.[3] and Osungunna, M. O.[3]

[1]*Department of Food Science and Technology, Federal University of Technology, Akure, Nigeria.*
[2]*Department of Chemical Engineering, Obafemi Awolowo University, Ile-Ife, Nigeria*
[3]*Department of Pharmaceutics, Faculty of Pharmacy, Obafemi Awolowo University. Ile-Ife, Nigeria*
[1*]bkadeoye@futa.edu.ng, [2]aransiolaef@gmail.com, [3]galebiowu@gmail.com, [3]mowole@oauife.edu.ng

[*]Corresponding author

ABSTRACT

This study developed functional excipients from biopolymer materials and evaluated their flow and compaction properties for preparation of tablet. Chitosan, a based excipient was extracted from snail shell and a compositional experimental design under the pharmaceutical dosage framework with corn-starch and lactose was used to study the singular and interaction effects of influencing parameters on the co-processed excipients, as well as, individual excipients. X-ray diffraction profiles showed that the chitosan produced was rich in or mostly made up of calcium silicate ($CaSiO_3$). The novel functional excipients developed had substantially better flow with Hausner's ratio ranging from 1.254 to 1.327, Carr's index from 20.272 to 24.627, angle of repose from 26.06 to 36.32° and angle of internal friction from 38.84 to 44.82°. The novel excipients also had improved compaction properties with compressibility values ranging from 0.390 to 0.537, consolidation rate from 0.559 to 0.675 and consolidation index from -1.466 to -1.268, which were advantageous in tableting. The role of pressure as the most significant parameters influencing the compaction and consolidation rate was also established. The results suggest that the better rate of flow and compaction propeties of co-process excipients can be achieved with high volume of chitosan at moderate mixing ratio.

Keywords: *Excipients, biopolymer, flow, compaction, chitosan, consolidation.*

1. INTRODUCTION

Excipients are components other than the active substances intentionally added to formulation of a dosage form in drug production (Goh *et al*., 2018). However, compacting composite excipients into tablets, on the other hand, is difficult because powder flow involves frictional contact of individual particles, which often lead to structural changes and densification during compression. A wide range of studies have been conducted world-wide to investigate the complex interaction of crystal structure, particle shape, particle size distribution, and single and multi-forces within the particles of single and composite excipients. Limited number of these studies were conducted in Africa (Builders and Arhewoh, 2016).

Development of excipients from biopolymer materials available in Africa may generate many arguments than the developed world due to characteristics of powders (largely unrefined), different production techniques and weak regulation on the qualities of other binder, diluents and lubricant combinations imported into the continent. Also, the method of production is mostly uncontrolled as most people still use uncleaned production apparatus (i.e. mortal, pistle, firewood for cooking), mostly in poor ventilated space, which in turns give structural damage and contamination to the produced excipients. The extent to which these features alter powder flowability is still a difficult task.

This study aimed at investigating the combined effect of different proportion of naturally extracted chitosan from snail shell, industrial grade corn-starch and lactose for probiotics excipient development. Also, the singular and interaction effects of influencing parameters (Density; Hausner's ratio; Carr's index; angle of repose; angle of internal friction; The Kawakita model; Consolidation index and Rate of consolidation) on the flow and compaction properties of excipients' formulations were investigated. The result of this study could serve as eye-opener to the relevant stakeholders and enhance further research on untapped natural biopolymer materials available for excipients development.

2. MATERIALS AND METHODS

2.1 Source of Materials

The snail shells used were obtained from Oja Tuntun, Ile-Ife, Osun State, Nigeria. Lyophilized *Lactobacillus delbruikii* (10^8 - 10^{10}CFU/g) isolated from fermented Bambara groundnut (*Vigna subterranea* (L.) Verdc.) was used as the model bacterial in this experiment. All other chemicals utilized were of analytical grade.

2.2 Methods

2.2.1. Extraction and characterization of chitosan

Chitosan was extracted from snail shell. The basic processes involved were pulverization using a Rocklabs mill, deproteinization using 0.1 M sodium hydroxide, decolourization in pure acetone, demineralization using 0.5 M hydrochloric acid and deacetylation by boiling in 0.2 M sodium hydroxide. Characterization of the extracted chitosan was carried out using Fourier Transform Infrared Spectroscopy (FTIR).

2.2.2. Determination of density attributes and flow characteristics

The particle density was measured using a solvent pycnometry technique as described by Adeoye and Alebiowu, 2013. The average of three determinations was used to arrive at the final outcome. The angle of repose, Hausner's ratio (HR), and compressibility index were used to evaluate the excipients' flow properties. Equation 1 was used to compute the angle of repose, which is the best angle that can be achieved between the self-supporting cone of the powder heap and the flat plain.

$$\theta = \tan^{-1}\frac{h}{r} \quad (1)$$

where h is the powder pile's or cone's height in cm, r is the radius of the cone's base in cm, and θ is the angle of repose. The Hausner's ratio (HR) was calculated from the bulk and tapped densities using Equation 2, whereas the compressibility index was calculated using Equation 3.

$$Haustner's\ ratio = \frac{Tapped\ density}{Bulk\ density} \quad (2)$$

$$Carr's\ index = \frac{Tapped\ density - Bulk\ density}{Tapped\ density} \times 100 \quad (3)$$

2.2.3. Evaluation of Compaction Properties

The packing and cohesive qualities of the excipients were measured by Kawakita equation shown in Equation 4.

$$\frac{N}{C} = \frac{N}{a} + \frac{1}{ab} \quad (4)$$

where N is the number of taps, and a and b denote the compressibility and cohesiveness of powders (1/b), respectively. Term C was calculated using equation 5 to describe the volume loss during tapping.

$$C = \frac{V_O - V_N}{V_O} \quad (5)$$

Where V_o is the powder's loose volume before tapping and V_N is the powder's volume after set numbers of taps

2.2.4. Estimation of consolidation index and rate

The consolidation behaviour of the co-excipients and their constituent excipients was investigated adopting the approach outlined by Neumann *et al*. (1967) in equation 6, by measuring the proportionate decline in powder volume and density as a response to applied load.

$$\frac{\log(\rho_T - \rho_B)}{\rho_T} = K \log N + C \quad (6)$$

where, ρ_T and ρ_B are the tapped and bulk densities, respectively, N is the number of taps, C is the consolidation index, and K is the consolidation rate.

2.2.5. Angle of internal friction measurement (AIF)

By graphing the porosity factor, $\varepsilon^2 N/1-\varepsilon$ in (Equation 7) versus N, The AIF was calculated using the relationship between porosity and the number of taps (N) used to induce powder bed consolidation. The AIF was computed by determining the angle created between the straight path and the abscissa when K - K_o was re-plotted against N (Adeoye and Alebiowu, 2013)

$$k = \varepsilon^2 N/1-\varepsilon \quad (7)$$

N is the number of taps, and Ko will represent the intercept of the plot of K versus N.

2.2.6. Preparation of probiotics-loaded tablets

This was done according to the method described by Alebiowu and Itiola (2007) with slight modification. Formulations 1 – 8 (F1-F8) were prepared with the polymers in different ratios and the required active pharmaceutical ingredients (API) dose by mixing thoroughly in a mortar as shown in Table 1.

DOI: 10.51975/23380205som
Journal of the Nigerian Society of Chemical Engineers, 38(2), 2023

Table 1: Formulation of 450 mg Probiotic Powder

Excipients	F1	F2	F3	F4	F5	F6	F7	F8
API	4.5	4.5	4.5	4.5	4.5	4.5	4.5	4.5
Chitosan	225	225	225	225	270	270	270	270
Corn-Starch	166.5	121.5	76.5	144	121.5	76.5	54	99
Lactose	45	90	135	67.5	45	90	112.5	67.5
Magnessium stearate	4.5	4.5	4.5	4.5	4.5	4.5	4.5	4.5
Talc	4.5	4.5	4.5	4.5	4.5	4.5	4.5	4.5

F1-F8 are formulations 1-8, API-active pharmaceutical ingredient

3. RESULTS AND DISCUSSION

3.1. Physical and morphological characteristics of extracted chitosan

Figures 1 - 3 shows X-ray diffraction spectra, elemental weight composition, scanning electron microscope (SEM) images of extracted chitosan respectively. Figure 4a and 4b shows the FTIR spectra of both extracted and conventional chitosan respectively. The morphological properties of excipients have been reported to be affected by the particle engineering process (Adeoye and Alebiowu, 2013). Figure 2 revealed the elemental composition of the samples. It allowed a quick guess that the sample analysed was rich or essentially made up of calcium silicate ($CaSiO_3$). Calcim silicate has been demonstrated to have no adverse effects in short-term toxicity study in rats (Liu *et al*., 2011)

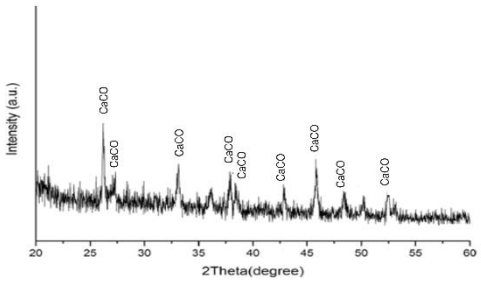

.

Figure 1: X-ray Diffraction of Chitosan

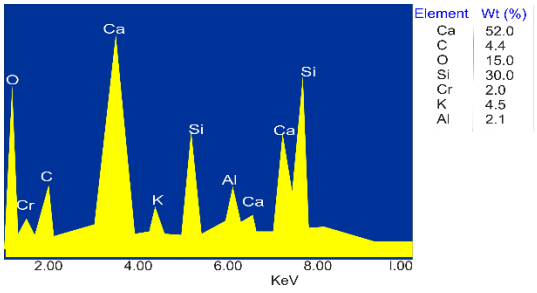

Figure 2: Elemental Weight of Chitosan

It also revealed that the sample analysed is free from heavy metal contamination, having undergone further purification to remove chromium contained in its composition, and is therefore safe for human health. The revealed chitosan particles appeared to be dense, with particles near the surface having distinguishable shapes. Spheres, ovals, and short cylinders are the most visible shapes. As illustrated in Figure 3, all of the shapes have a smooth appearance. The absence of sharp edges indicates a useful property necessary for smooth blood vessel transport as contained in US Pharmacopeia guidelines. In transportation, a smooth surface suggests low wear and friction. This implies that there wiould be less wear and degradation, which is common with drug-loaded micro-particles when delivering active pharmaceutical ingredient to ailing locations. Another advantage derivable from the smoothness of the micro-particles surface is reduced systemic circulation time to forestall premature drug release, having recognized that micro-particles tend to arrive their tumor-destination with little stress and at a shorter time under active tumor targeting scheme (Liu *et al*., 2011).

Spectra of the chitosan produced have no much characteristic different from the spectra of the chitosan standard as shown in Figures 4a and 4b respectively. The increase in adsorption effectiveness is due to the bending vibrations of functional groups such as C=O (H bound) and N–H (1 amide). The results are in agreement with the work of Puvvada *et al*., (2012) and Zvezdova, (2010). In case of conventional, broad bands observed at 3441.01 and 2974.23 cm^{-1} are due to O-H stretching

vibrations whereas a band at 1240 cm^{-1} is due to O-H bending vibration. The bands in the region 1404.18–1311.59 cm^{-1} are attributed to C-H stretching vibrations, while the one observed at 2927.94 cm^{-1} is due to C-H stretching vibrations. The bands at 1662.64 and 1554.63 cm^{-1} are due to stretching vibrations of aromatic structure C=C. In case of chitosan produced, a broad band at 3442 cm^{-1}, with a larger intensity compared to standard, is due to the presence of more crosslinked hydroxyl groups.

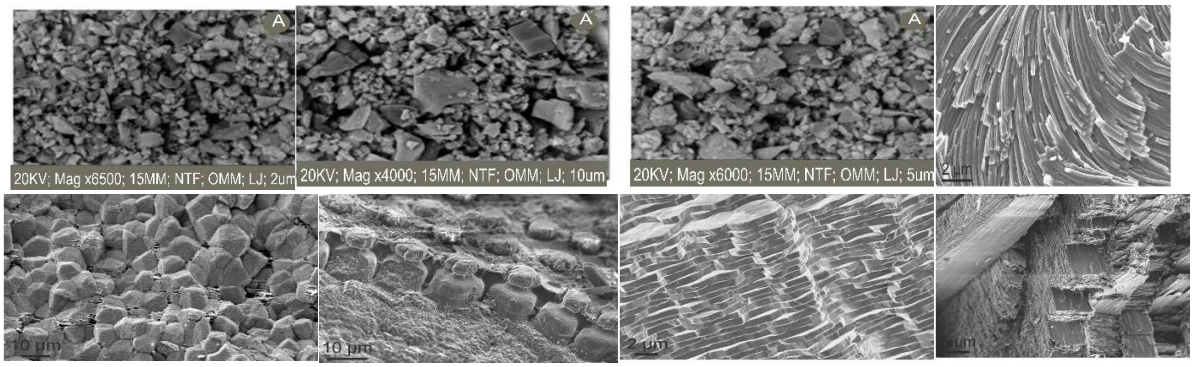

Figure 3: Scanning Electron Microscopy (SEM) Images of Chitosan at Different Magnitude

Intense bands that appeared at 2926.82 and 2517.41 cm^{-1} are due to aliphatic C-H stretching vibrations. The bands at 1798.72 and 1427.63 cm^{-1} are assigned to C-H bending vibrations. The bands appearing at 872.86 cm^{-1} are due to the presence ring stretching (NH_2 Amines groups). The new band 707.82 denote cis = C–H out-of-plane bending. In all, FT-IR confirms the crosslinking reaction.

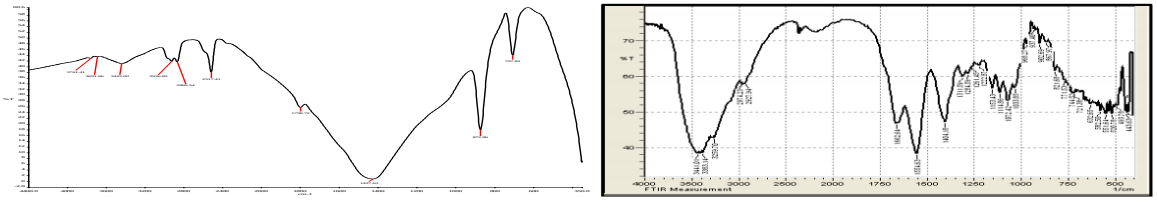

Figure 4a:FTIR specra of extracted chitosan Figure 4b: FTIR spectra of chitosan standard

3.2. Fundamental and Derived Properties of The Excipients

1. Densities of the excipients

The density of powders affects their behaviour during use and have been used in the characterization of some derived properties of powder system such as Hausner's ratio, Carr's index, porosity, packing fraction among others. Particle density has an impact on the packing behaviour of materials during tableting, notably during the initial compression phase, which is also known as the elasto-plastic flow phase (Okunola and Odeku, 2009). The results in Table 2 showed that the novel excipients' bulk density and tapped densities in formulation 1 - 8 were higher than native excipients. The higher values of bulk and tapped densities of chitosan could have probably have influenced the increase in values found in novel excipient. More increase in values were noticed when the concentration of chitosan in the excipients' formulation was increased. This is advantageous in engineering design aspect of tablet manufacturing because the fill volume of the die is reduced at higher bulk density value (Okunola and Odeku, 2009). Improved consolidated bulk density is advantageous in tableting because it minimizes die load volume and enhances flow rates, all of which contribute to improved tablet homogeneity (Ogunjimi and Alebiowu, 2013; Okunola and Odeku, 2009). When compared to native excipients, this means that the novel excipients developed would form tablets at a higher compression force of 1.8N

2. Derived flow properties

The excipients' flow attributes were assessed employing these important flow features i.e. Hausner's ratio (HR), Carr's index (CI), bulkiness, packing percentage, angle of repose and angle of internal friction (AIF) as their values shown in Table 3. Quantifying the resistance of the powder mass to flow, the angle of repose gives an indicator of the inter-particulate frictional forces working within the powder system (Adeoye and Alebiowu, 2013). Free flow is indicated by an angle of 30° or less, while poor flow is indicated by an angle of 40° or more (Huh and Scriven, 1971). The particle size

distribution has an effect on the angle of repose, which normally increases as particle size decreases. For solid dose technology, values below around 30° are generally thought to be suitable (Adeoye and Alebiowu, 2013).

The novel excipients, as shown by the angle of repose ranged from 26.06° to 36.32°, have better flow qualities than the native excipients, which ranged from 29.34° to 32.89° as shown in the Table 3, corresponding to excipient in formulations 2 (F2) and 8(F8) respectively. It can be said that formulations 2, 3, 4, 5 and 7 have good flow properties while formulations 1, 6 and 8 have fair flow properties. A Hausner's ratio (HR) of less than 1.2 indicates acceptable powder flowability, but HRs of 1.5 or higher indicate poor powder flowability (Hausner, 1967).

Table 2: Density Properties of the Excipients

Excipient	True density (g/ml)	Bulk density (g/cm^3)	Tapped density (g/cm^3)	Bulk volume (cm^3)	Tapped volume (cm^3)
Chitosan	2.760	0.989	1.353	30.314	22.17
Corn starch	1.734	0.53	0.614	56.556	48.864
Lactose	2.420	0.729	0.961	41.173	31.219
F1	2.302	0.881	1.105	33.934	27.147
F2	2.470	0.934	1.184	32.124	25.337
F3	2.439	0.947	1.239	31.671	24.206
F4	2.336	0.908	1.163	33.029	25.79
F5	2.404	0.947	1.228	31.671	24.432
F6	2.473	0.975	1.275	30.766	23.527
F7	2.507	1.036	1.326	28.957	22.622
F8	2.439	0.961	1.275	31.219	23.527

Table 3: Flow Properties of the Excipient

Excipient	Hausner's ratio	Carr's index (%)	Bulkiness (cm^3/g)	Packing fraction	Porosity	Angle of repose	Angle of internal friction
Chitosan	1.367	26.859	1.011	0.358	0.642	32.89	49.02
Corn starch	1.158	13.681	1.887	0.306	0.694	29.34	57.57
Lactose	1.318	24.142	1.372	0.301	0.699	31.38	57.36
F1	1.254	20.272	1.135	0.383	0.617	34.71	44.82
F2	1.268	21.115	1.071	0.394	0.606	26.06	42.99
F3	1.308	23.567	1.056	0.388	0.612	32.99	43.99
F4	1.281	21.926	1.101	0.389	0.611	28.91	42.78
F5	1.297	22.883	1.056	0.394	0.606	31.24	42.99
F6	1.308	23.529	1.026	0.394	0.606	34.13	42.99
F7	1.28	21.87	1.965	0.413	0.587	31.29	38.84
F8	1.327	24.627	1.041	0.394	0.606	36.32	42.99

The values of HR showed that both the native and the novel excipients have good flow. The HR is the proportion of bulk densities that have been tapped to those that have been aerated. The HR's values for formulation 8 was 1.327, which was very high. Formulations 1, 2, 4, 5, and 7 had Hausners' ratios of 1.254, 1.268, 1.281, 1.297, and 1.280, respectively, demonstrating a better flow than the original state. Carr's index is an assessment of the compressive strength of a powder and an intuitive determinant of the fluidity of a substance. The higher the value, the more firmed the

powder is, signifying that there isn't enough flow. Carr's indexes of 16 to 25% indicate excellent flow characteristics but levels beyond 25% indicate cohesiveness or poor flow performance (Carr, 1965). All the novel excipients had carr's index values lower than those of chitosan and lactose. The values obtained ranges from 20.272 to 24.627 corresponding to excipients in formulations 1 and 8 respectively. Chitosan

had the highest values with CI of 26.859 and HR of 1.367 indicating poor compressibility but a fair flow. Corn-starch and lactose on the other hand had lower CI values of 13.681 and 24.142 respectively while their HR are 1.158 and 1.318, which implies good compressibility and better flow. The synergy brought about by these complementary effects might be the reason for good compressibility and flows found in the novel excipient. This shows that mixing chitosan with corn-starch and lactose could aid in the creation of excipients with improved flow properties, which would be more effective in direct compression.

It has been argued that the degree of internal friction, rather than the angle of repose is a better indicator of flow arrangement due to the limited repeatability of the angle formed by the powders. This accumulates to a high angle and then drops to a comparatively deep angle (Neather, 2016). Varthalis and Pilpel (1976) proved that the angle of internal friction is one of the fundamental flow characteristics of the bulk solids which characterize the failure properties of the particle assemblage under load. Each particle roughness is present in powder flow, and this cross friction has been proven to have a significant consequence on powder packing. (Goh *et al*., 2018).

From Table 3, the ranking for angle of internal friction is Cs > Ls > Ch > F1 > F3 > F2, F5, F6, F8 > F7. The estimates of the angle of internal friction demonstrated that the novel excipients produced had substantially improved flow characteristics in comparison to single original excipients. A higher value of the angle of internal friction denotes greater cohesiveness of the particle and the creation of bridges and arches in the powder, both of which restrict flow (Adeoye and Alebiowu, 2013; Juneja *et al*., 2014). The observations imply that elevating particular quantities of chitosan in the excipient could assist to minimize patches of unwanted air in tablets, which can induce capping and/or lamination of the tablets, particularly while using in direct compression of tablets. This is in agreement with the work of Niranjan, (2013) who studied the sliding wear behaviour in composite mixture and concluded that increase in cohesiveness of particles can be the result of higher values of angle of internal frictions.

3.3 Packing and Cohesive Properties of the Novel Excipients

Compactibility refers to a material's ability to form compact tablets with acceptable tensile strength when subjected to densification. As the porosity of a compact decreases, its tensile strength increases (Sun, 2006). The Kawakita's model in Equation 4 reflects the amount of shrinkage in a powder bed to the tapping pressure. The model could be used to comprehend powder redevelopment, based on the established linearity relationship. The Kawakita coefficient 'a' denotes the powder bed's minimal porosity prior to application of load, which is related to its compressibility. The powder is packed thicker the initial time it was fed into the cylinder, if the value of 'a' is low. The value of 'b' is the inverted assessment of cohesiveness calculated from the plot's intercept. The higher the powder's 'a' value, the better the compressibility, which is important for direct tablet compression. The Plots of N/C against the number of taps for native excipients, F1-F4 and F1-F8 respectively, were done to determine the values of a, i.e. the volume reduction after tapping as percentages derived from straight line gradient as shown in Table 4. The rank order of "a" is F6>F4>F3>F8>F7>F2>F1. Since tapping did not result in a significant improvement in packing, the low values in some formulations indicate that the powders were sufficiently packed prior to tapping. The result presented in Table 4 showed that chitosan had the highest values. Tapping reduces voids in powders with a low value of ‘‘a" by removing air from the build platform without changing the particle structure or shape (Adeoye and Alebiowu, 2013).

3.4

3.5 Consolidation Index and Rate of Consolidation

The correlations between both the log of density variations and the log frequency of taps as shown in Equation 6 were respectively used to derive the consolidation index and rate of consolidation for native excipients, F1-F4 and for F5-F8. Both the rate of consolidation, K (an indicator of the efficiency of packing powder), and the consolidation index, C (a reflection of the influence of packing on flow) are both improved when the amount of chitosan or corn-starch in the novel excipient was increased. The finding could be linked to the combination's influence, which culminated in less unevenly shaped particles with a lower fraction of corn-starch or lactose, making particle reorganization simpler and resulting in a greater consolidation index. Reduced quantities of corn-starch starch or lactose in the novel excipients may have caused particle dimension reconfiguration, lessening the cohesive solid–solid association and reducing the consolidation rate, K. Because powder flow entails frictional contact between individual particles as well as a reduction in the Van der Waals forces’s influence on cohesion, this inevitably means that flowability is increased, resulting in an improvement in the consolidation index. The degree of

splitting and fracture at particle interaction locations, as well as the amplitude and severity of forces of attraction among connecting particles, all impact the flow feature of a powder mixture (Ogunjimi and Alebiowu, 2013). The rank order for C is Ch > F7 > F3 > F8 > F5 > F4 > F2 > F1 and F6 > L > Cs, as seen in Table 4.

The highest C value was found in chitosan, denoting that it has an increased cohesiveness and the capacity to infuse excellent mechanical properties in dosage forms, while the lowest were found in corn-starch. A lower lactose value also implies that native excipients are more cohesive and that corn-starch particles are more likely to reorganize and fill vacant spaces after tapping. When particles are tapped or vibrated, the rate of consolidation provides an indication of how quickly they pack together. Cs>L>F6>Cs>F4>F5>F1>F2 and F8>F3>F7 are the rank order for consolidation rates.

Table 4: Compaction Properties of Powders and Processed Excipient

Excipient Formulation	Compressibility (a)	Cohesiveness (b)	Consolidation Rate (K)	Consolidation Index (CI)
Chitosan	0.530	0.033	0.570	-1.204
Corn-starch	0.525	0.013	1.671	-4.178
Lactose	0.494	0.032	0.812	-1.887
F1	0.390	0.036	0.584	-1.466
F2	0.396	0.035	0.578	-1.410
F3	0.469	0.035	0.566	-1.281
F4	0.471	0.033	0.614	-1.403
F5	0.462	0.032	0.586	-1.345
F6	0.537	0.023	0.675	-1.466
F7	0.450	0.030	0.559	-1.268
F8	0.463	0.031	0.578	-1.322

4. CONCLUSION

In this study, the combined effect of different proportion naturally extracted chitosan, industrial grade corn-starch and lactose for probiotics excipient development was investigated. Singular and interaction effects of influencing parameters were also studied on the flow and compaction properties of excipients formulated. Our results showed from the estimates of the all micromeritics properties that the functional novel excipients developed had substantially better flow and compaction properties as well as improved consolidation characteristic when the amount of chitosan or corn-starch in the novel excipient was increased. Pressure plays the most significant impact in reducing the frictional contact between individual particles as well as the Van der Waals forces's influence on cohesion during tapping, leading to increase in flowability and subsequent improvement in the consolidation index**.** If the extracted chitosan could meet all US Pharmacopoeia specifications (such as limits of inorganic impurities and specific tests), then the novel excipients of chitosan, corn-starch and lactose could be suitable for use as less expensive alternatives to imported directly compressible excipients for probiotic tablet. Obtained results could serve as an eye-opener for relevant stakeholders by providing them relevant information required to evaluate and harness local biopolymer available for excipients development.

REFERENCES

Adeoye, O. and Alebiowu, G. (2013). Flow, packing and compaction properties of novel coprocessed multifunctional directly compressible excipients prepared from tapioca starch and mannitol. *Pharmaceutical Development and Technology, 19*(8), pp. 901-910.

Alebiowu, G. and Itiola, O. A. (2003). The influence of pregelatinized starches disintegrants on interacting variables that act on disintegrant properties. *Pharmaceutical Technology*, 27, pp 28-31

Antunes, F., Andrade, F., Araújo, F., Ferreira, D., and Sarmento, B. (2013). Establishment of a triple co-culture in vitro cell models to study intestinal absorption of peptide drugs. *European Journal of Pharmaceutics and Biopharmaceutics, 83*(3), pp. 427-435.

Builders, P. F., and Arhewoh, M. I. (2016). Pharmaceutical applications of native starch in conventional drug delivery. *Starch-Stärke, 68*(9-10), pp. 864-873.

Carr, R. L. (1965). Evaluating flow properties of solids. Chemical Engineering Journal, pp. 72: 163-

Goh, H. P., Heng, P. W. S., and Liew, C. V. (2018). Comparative evaluation of powder flow parameters with reference to particle size and shape. *International Journal of Pharmaceutics, 547*(1-2), pp.133-141.

Huh, C., and Scriven, L. E. (1971). Hydrodynamic model of steady movement of a solid/liquid/fluid contact line. *Journal of Colloid and Interface Science, 35*(1), pp. 85-101.

Hausner H. H. (1967). Friction conditions in a mass of metal powder. Internationa Journal Powder Metall, 3: pp. 7-13.

Juneja, P., Kaur, B., Odeku, O. A., and Singh, I. (2014). Development of Corn Starch-Neusilin UFL2 conjugate as tablet superdisintegrant: Formulation and evaluation of fast disintegrating tablets. *Journal of Drug Delivery, 2014*.

Kawakita, K., and Lüdde, K.-H. (1971). Some considerations on powder compression equations. *Powder Technology, 4*(2), pp. 61-68.

Leonida, M., Ispas-Szabo, P., and Mateescu, M. A. (2018). Self-stabilized chitosan and its complexes with carboxymethyl starch as excipients in drug delivery. *Bioactive materials, 3*(3), pp. 334-340.

Liu, T., Li, L., Teng, X., Huang, X., Liu, H., Chen, D., and Tang, F. (2011). Single and repeated dose toxicity of mesoporous hollow silica nanoparticles in intravenously exposed mice. *Biomaterials, 32*(6), pp. 1657-1668.

Neather, A. C. (2016). Experimental investigations of granular matter flow regimes leading to insight into lahar flow dynamics: a Ph.D thesis presented in partial fulfilment of the requirements for the degree of Doctor of Philosophy in Earth Science at Massey University, Manawatū, New Zealand. Massey University.

Niranjan, P. (2013). *Formulation and Invitro Evaluation of Sustained Release Matrix Tablets of Ibuprofen.* Adhiparasakthi College of Pharmacy, Melmaruvathur, Tamil Nadu, India.

Ogunjimi, A. T., and Alebiowu, G. (2013). Flow and consolidation properties of neem gum coprocessed with two pharmaceutical excipients. *Powder technology, 246*, pp. 187-192.

Okunola, A., and Odeku, O. (2009). Compressional Characteristic and Tabeting properties of Starches obtained from four dioscora species. *Famacia,* 57, pp. 756-769.

Puvvada, Y. S., Vankayalapati, S., and Sukhavasi, S. (2012). Extraction of chitin from chitosan from exoskeleton of shrimp for application in the pharmaceutical industry. *International Current Pharmaceutical Journal,* 1(9), pp. 258-263.

Varthalis, S., and Pilpel, N. (1976). Anomalies in some properties of powder mixtures. *Journal of Pharmacy and Pharmacology, 28*(5), pp. 415-419.

Zvezdova, D. (2010). Synthesis and characterization of chitosan from marine sources in Black Sea. *Научни Трудове На Русенския Университет, 49*(9), pp. 65-69

DOI: 10.51975/23380206som
Journal of the Nigerian Society of Chemical Engineers, 38(2), 2023

SOLVENT EXTRACTION OF ACETIC ACID FROM AQUEOUS MEDIA USING TRIOCTYL PHOSPHINE OXIDE (TOPO) – BASED SOLVENT SYSTEMS

***Sanda, O.[1,2], Ehinmitola, E. O.[1], Fakinle, B. S.[2] and Taiwo, E. A.[1]**

[1]*Department of Chemical Engineering, Obafemi Awolowo University, Ile-Ife, Nigeria*
[2]*Department of Chemical, Landmark University, Omu-Aran, Kwara state, Nigeria*

[1,2*] *osanda@oauife.edu.ng,* [1] *fehinmi@oauife.edu.ng,* [2]*fakinle.bamidele@lmu.edu.ng,* [1] *etaiwo@oauife.edu.ng*

[*]Corresponding author

ABSTRACT

Acetic acid is a very important commodity chemical with several applications in the chemical and food industry. Although acetic acid can be produced readily via fermentation processes, various factors such as low yield, the presence of secondary fermentation products and the rather complex separation requirements make the production high quality acetic acid via the fermentation route rather expensive. This study examined the reactive extraction of acetic acid from aqueous media using trioctyl phosphine oxide (TOPO) with n – hexane, toluene, methyl isobutyl ketone (MIBK) and methyl ethyl ketone (MEK) as diluents. Effect of various parameters such as phase ratios, and concentration of TOPO in the diluents on the degree of extraction of acetic acid were studied and the results obtained showed that while MEK on its own gave a higher extraction yield than MIBK, a reversal in trends was observed on adding TOPO to these solvents with the MIBK – TOPO system having a greater degree extraction, compared to the MEK – TOPO system. The extractions performed using n-hexane and toluene as diluents gave higher extraction yields with toluene. The degree of effectiveness of the diluents in the extraction of acetic acid from aqueous media is MIBK > MEK > Toluene > n – hexane.

Keywords: *Acetic acid, MIBK, MEK, Reactive Extraction, TOPO.*

1. INTRODUCTION

Frequently, chemical engineers and organic chemists must separate organic compounds of interest from a mixture of compounds, often derived from natural sources or product of synthetic reactions. One method commonly used to separate such mixture of compounds is known as solvent extraction or liquid-liquid extraction (Cox and Rydberg, 2004; Wasewar, 2012; Ingle *et al.*, 2017; Sas *et al*., 2018; Alves De Oliveira *et al.*, 2020). In separation and purification technology, liquid-liquid extraction plays an important role and has been successfully applied in the isolation of organic compounds such as lactic acid (Udachan and Sahoo, 2014; Komesu *et al.,* 2017; Li *et al*., 2021), citric acid (Araújo *et al*., 2017), itaconic acid (Kreyenschulte *et al*. 2018), and other valuable organic acids from fermentation broths. Another very important organic acid which can be recovered from fermentation media using this method is acetic acid.

Acetic acid is a commodity chemical with several applications in the food and chemical industry. Acetic acid is used in several industrial sectors such as chemical, pharmaceutical, textile, polymer and paints, food and beverages, with a substantial proportion of the global production being used in the production of cellulose acetate (Candido *et al*., 2017) and vinyl acetate monomer (VAM) which is used in the production of a wide range of polymers and resins for paints, adhesives, films, and a myriad of other industrial and consumer applications (Das *et al*., 2009; Li *et al*., 2022). Acetic acid also finds uses in the food industry as food additive (code E260) as an acidulant and as a condiment (Derossi *et al*., 2011; Awuchi *et al*., 2020).

Acetic acid is produced industrially synthetically via the cabonylation of methanol (Haynes, 2006; Kalck *et al*., 2020), oxidation of acetaldehyde (Han *et al*., 2019) or by fermentative oxidation of ethanol (Gullo *et al*., 2014). Unfortunately, the disadvantage of fermentation is that it produces rather dilute solutions of acetic acid due to the inhibitory nature of the acid to the fermentation microorganisms (Lin and Tanaka, 2006). In addition, the fermentation broth always contains many impurities including cell biomass, other organic acids, and unconsumed nutrients (Zi *et al*., 2013; Zentou *et al.,*

2021). Recovery and purification of acetic acid from dilute media requires many steps and unit operations, which consequently contribute to high cost of production.

Reactive extraction has been one of the attractive methods for the recovery of carboxylic acids and has been studied by several researchers Some extractants that have been investigated include tri-n-octylamine (Uslu, 2009; Inyang and Lokhat, 2020), tributyl phosphate (Djas and Henczka, 2018) and trioctyl phosphine oxide (Djas and Henczka, 2018) as well as neutral extractants with oxygen-containing polar groups (Djas and Henczka, 2018; Pandey and Kumar, 2018; Mungma *et al*., 2019). This work studied the extraction of acetic acid with methyl isobutyl ketone (MIBK), methyl ethyl ketone (MEK), trioctyl phosphine oxide (TOPO) and their blends. The objective is to examine the influence of different variables such as phase ratio, initial feed concentration and nature of organic extractant on the extraction of acetic acid.

1.1 Reactive Solvent extraction of carboxylic acids

The reactive extraction of a carboxylic acid (HA) with an extractant (E) gives a reaction complex, which remains in the organic phase (Mukherjee and Munshi, 2020):

$$HA + n\bar{E} \rightleftharpoons \overline{(HA)(E)_n} \quad (1)$$

Where HA represents the unassociated part of the acid present in the aqueous phase and the overbar represents the species in the organic phase. From equation (1), the equilibrium extraction constant k_{ex} can be written:

$$k_{ex} = \frac{\left[\overline{(HA)(E)_n}\right]}{[HA][\bar{E}]^n} \quad (2)$$

Where the square brackets are the concentrations of the respective species. The distribution coefficient of acetic acid in the aqueous and organic phases (K_D) is defined by:

$$K_D = \frac{\overline{[HA]}}{[HA]} \quad (3)$$

where [HA] and $\overline{[HA]}$ are the concentrations of the acid in the aqueous and organic phases, respectively. It is noteworthy that here, $\left[\overline{(HA)(E)_n}\right]$ and $\overline{[HA]}$ represent the same quantity. Thus, equation (2) becomes:

$$k_{ex} = \frac{K_D}{[\bar{E}]^n} \quad (4)$$

The value of the extraction constant can be determined from a plot of log (K_D) against log $[\bar{E}]$ where (4) is written in a linear form:

$$\log k_D = \log k_{ex} + n \log[\bar{E}] \quad (5)$$

2. MATERIALS AND METHODS (OR METHODOLOGY)

Methyl isobutyl ketone (MIBK), methyl ethyl ketone (MEK), n – hexane and toluene were obtained from BDH chemicals while tri-n-octyl phosphine oxide (TOPO) was obtained from Sigma-Aldrich. All solvents used as organic phase or extractant were of analytical grade and were used without further purification. Glacial acetic acid (Merck) was used to prepare the various concentrations used in the study. All experiments were performed at 300 ± 2 K. For the purpose of the experiment, isothermal condition was assumed.

Aqueous acetic acid solution was prepared by dissolving glacial acetic acid in distilled water until the desired concentration was achieved, with the highest concentration used in this study being 16.9 g/L (or, 0.28 mol/L). The initial concentration of acetic acid in the aqueous phase was determined by titration against 0.1 M NaOH using phenolphthalein as indicator. The extraction and stripping experiments were carried with 20cm^3 of the aqueous phase shaken with specified volumes of the organic solvents in stoppered 250 ml glass flasks on a tabletop mechanical shaker at 300 rpm for 20 min, after which the mixtures were poured into 250 ml separating funnels and allowed to settle for 3 h for complete phase separation. The quantity of acetic acid left in the aqueous phase was determined by titration with 0.1 M NaOH solution, while the acid content of the organic phase was obtained by material balance. The process was repeated for 2, 3, 4 and 5 successive extractions using equal volume of aqueous and organic phases in each case for batch extraction in stages and varying volume of solvent for single batch extraction. This procedure was repeated for the various solvent blends used.

The level of extraction for each solvent system was expressed in terms of the percentage extraction which is defined as (Inyang and Lokhat, 2020):

$$\text{Percentage Extraction } (\%E) = \left(\frac{V_o C_o - V_{eq} C_{eq}}{V_o C_o}\right) \times 100 \quad (6)$$

Where V_o and V_{eq} are the initial and equilibrium volumes of the aqueous phase, respectively. In addition, C_o and C_{eq} are the initial and equilibrium concentrations of acetic acid in the aqueous phase, respectively.

3. RESULTS AND DISCUSSION

3.1 Acetic acid extraction with MIBK and MEK

A comparison of the solvent extraction of acetic acid was made for both MIBK and MEK for single batch and crosscurrent extractions and the result obtained (Tables 1 and 2) shows MEK to be a better extractant than MIBK. The general trend in the degree of extraction can be improved on using stage-wise crosscurrent extraction systems, compared to single extraction batches with the volume of the organic phase (V_o) increased as shown in Table 2. The equilibrium curves for the extraction of acetic acid using MIBK, MEK or their 1:1 blend (Figure 1) also showed MEK to be the better extractant.

Table 1: Single Batch Extraction of Acetic Acid into MEK and MIBK (C_o = 0.28 Mol/L)

	%E		
Phase Ratio (V_o:V_A)	MIBK	MEK	1:1 blend of MIBK and MEK
1:1	31.80	41.61	36.16
2:1	48.41	64.02	57.18
3:1	59.07	77.70	67.67
4:1	65.43	85.46	76.44
5:1	71.14	89.14	79.86

V_o = volume of organic phase. *V_A = volume of aqueous phase.*

Table 2: Batch-wise Extraction of Acetic Acid into MEK and MIBK (V_o :V_A = 1:1) (C_o = 0.28 Mol/L)

	%E		
No. of batches	MIBK	MEK	1:1 blend of MIBK and MEK
1	31.80	41.61	36.16
2	55.42	71.55	70.32
3	70.26	88.63	81.63
4	80.74	95.64	88.63
5	87.34	98.23	93.88

V_o = volume of organic phase. *V_A = volume of aqueous phase.*

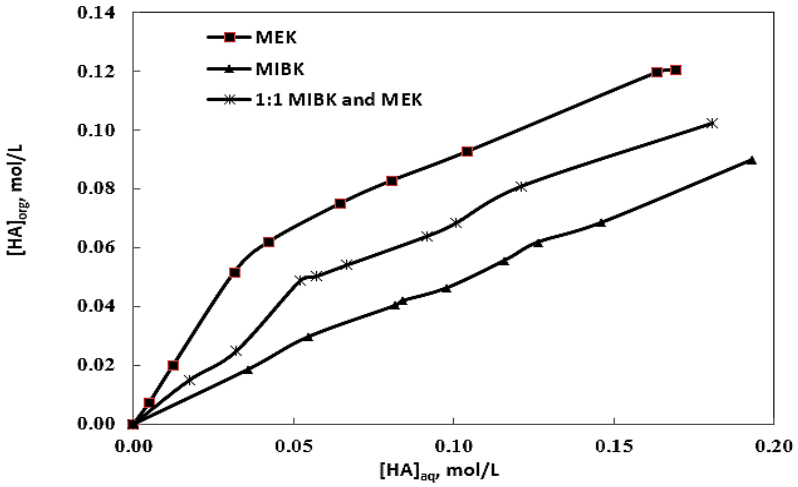

Figure 1: Distribution of acetic acid between phases for MIBK and MEK

3.2 Effect of adding a second extractant

The addition of small amounts of a second extractant (TOPO) to the organic phases gave an even greater separation for acetic acid as shown by the equilibrium plots in Figure 2. The highest percentage extraction for an extractant containing 1 % v/v TOPO in MIBK was found to be 74.15 % for a phase ratio of 5:1, compared to pure MIBK which gave a 71.14% recovery for the same phase ratio (Table 1). Also, a 1% (v/v) TOPO–MIBK solvent blend gave 88.57% recovery of acetic acid, compared to pure MIBK which gave 87.34 % for the same number of extraction batches as shown in Tables 3 and 4. Thus, the interaction between TOPO and MIBK is synergetic with respect to the extraction of

acetic acid from aqueous media. The addition of TOPO to MEK however had an antagonistic effect on the extraction of acetic acid as shown in Figure 3. The highest percentage extraction for a solvent system containing 1% TOPO in MEK was found to be 84.60 % for a phase ratio of 5:1 and 96.81 % for five extraction batches as shown in Tables 3 and 4.

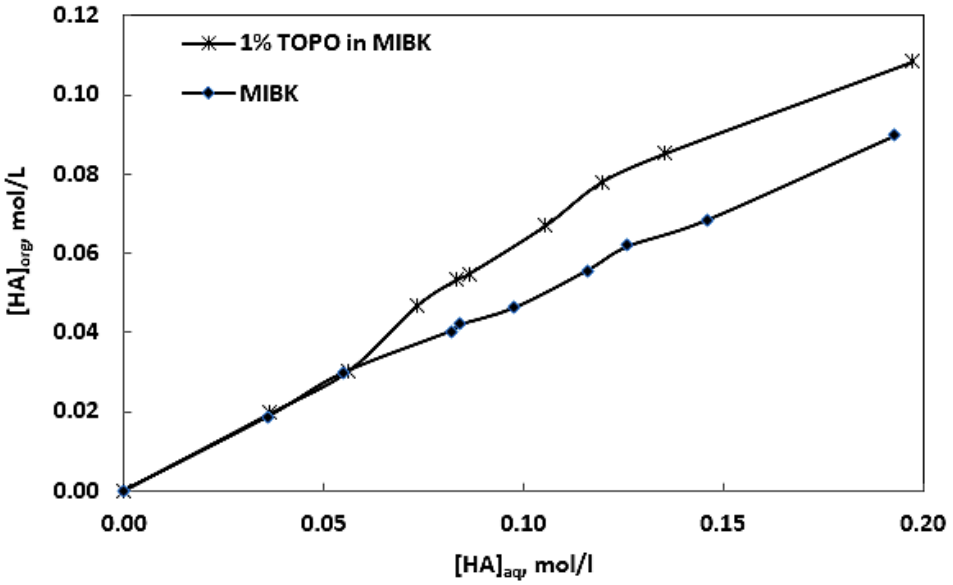

Figure 2: Distribution of acetic acid between phases using 1 % TOPO in MIBK as extractant

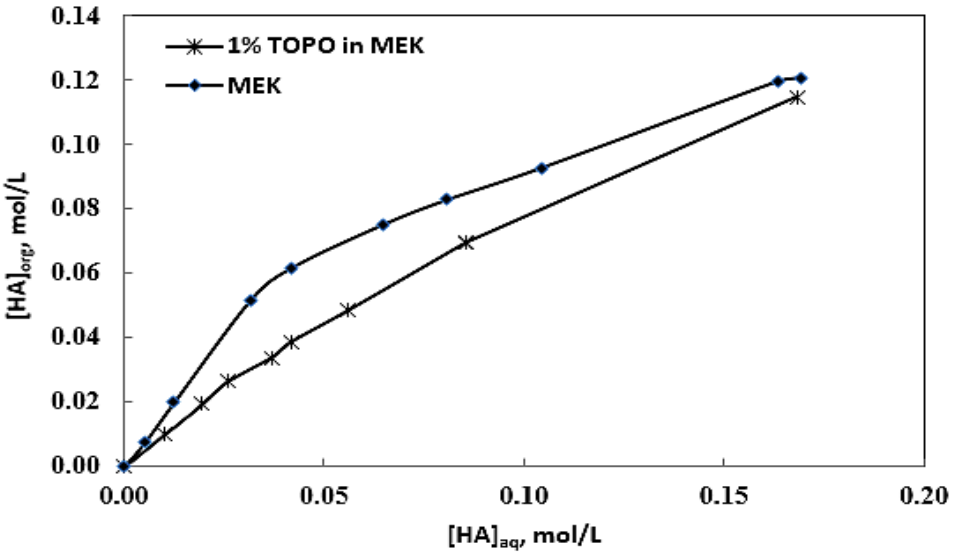

Figure 3: Distribution of acetic acid between phases using 1 % TOPO in MEK as extractant

Table 3: Single Batch Extractions of Acetic Acid with 1% TOPO in MEK and MIBK

	%E	
Phase Ratio (V_o:V_A)	1% TOPO in MIBK	1% TOPO in MEK
1:1	35.46	40.52
2:1	52.12	61.11
3:1	62.78	72.22
4:1	69.43	78.68
5:1	74.15	84.60

DOI: 10.51975/23380206som
Journal of the Nigerian Society of Chemical Engineers, 38(2), 2023

Table 4: Batch-wise Extraction of Acetic Acid 1% TOPO in MEK and MIBK (V_o :V_A = 1:1)

No. of batches	%E	
	1% TOPO in MIBK	1% TOPO in MEK
1	35.46	40.52
2	60.95	70.01
3	72.88	86.44
4	82.46	93.63
5	88.57	96.84

To further examine the extraction of acetic acid using TOPO, two additional solvents were introduced, which are n-hexane (an aliphatic hydrocarbon) and toluene (an aromatic solvent). Figure 4 illustrates the behavior of a 1 percent (w/v) solution of TOPO in n-hexane and toluene. From Figure 4, there use of toluene gave an increased extraction yield for acetic acid, when compared to n- hexane. These results are similar to those reported by Wasewar *et al*. (2011) and Inyang and Lokhat (2020).

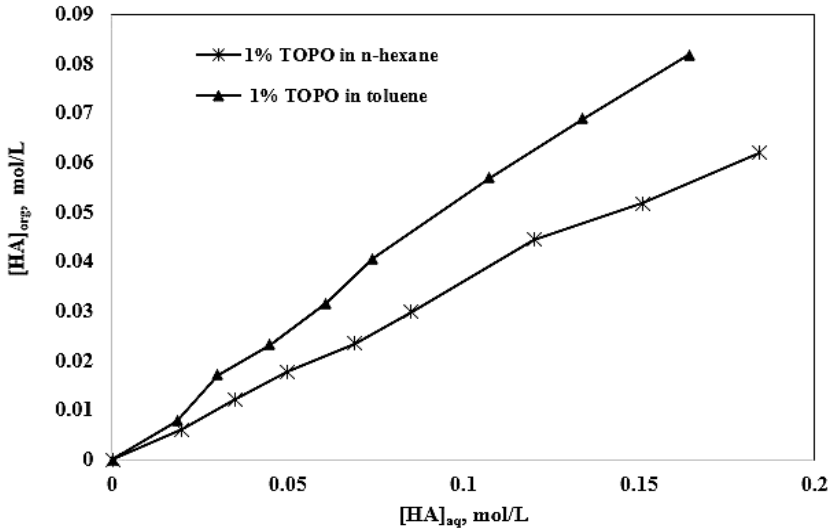

Figure 4: Distribution of acetic acid between phases using 1 % TOPO using toluene and n-hexane as extractants (V_O:V_A = 1:1)

Figure 5 shows the effect of increasing the concentration of TOPO on the acetic acid extraction yield. The concentration of TOPO in the solvents were varied from 0.02 and 0.30 mol/L while the initial aqueous phase concentration of the acetic acid was kept constant at 0.28 mol/L. From Figure 5, it can be inferred that the use of active diluents such as MIBK and MEK gave higher extraction yields with TOPO, compared with what was extracted using inert such as n – hexane and toluene. This is in agreement with the results obtained by Pal and Keshav (2014), and Sprakel and Schuur (2019). The use of an aromatic diluent such as toluene gave higher extraction yields than those obtained using an aliphatic diluent such as n – hexane.

The plot of the distribution coefficient against the concentration of TOPO (Figure 5) was fitted to equation (4) to obtain the equilibrium extraction constant k_{ex} and the results obtained are presented in Table 5. The number of TOPO molecules per molecule of acetic acid extracted was found to decrease in the order MIBK < MEK < toluene < n – hexane and the extraction constant also follows that trend. This trend is similar to the one reported by Wasewar and Shende (2011) in the extraction of caproic acid using Aliquat 336, and Udachan and Sahoo (2014) for the extraction of lactic acid using trioctyl amine.

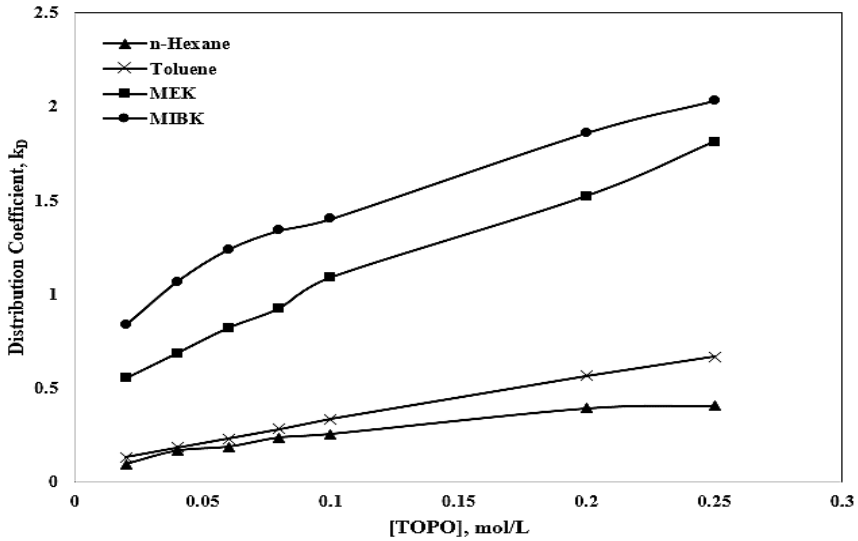

Figure 5: Effect of TOPO concentration on the extraction of acetic acid from aqueous media

Table 5: Extraction equilibrium parameters for each of the solvent systems

Diluent	Extraction constant (K_{ex})	n	R^2
n- Hexane	0.954	0.57	0.9851
Toluene	1.579	0.66	0.9896
MEK	3.237	0.48	0.9829
MIBK	3.268	0.34	0.9964

4. CONCLUSION

The extraction of acetic acid using trioctyl phosphine oxide in inert diluents (n – hexane and toluene) and active diluents (MEK and MIBK) were studied at room temperature and the following conclusions were made. MIBK and MEK on their own are good extractants for acetic acid with recovery for a phase ratio of 1:1 being 31.80% for MIBK and 41.61% for MEK, indicating that MEK is a better extractant for acetic acid from aqueous media, compared to MIBK. While synergistic extraction was observed on addition of small amounts of TOPO to MIBK, the addition of similar quantities of TOPO to MEK had an antagonistic effect, with the extraction yield dropping to 40.52 %. Although the recovery of acetic acid using TOPO in the inert diluents increased with increasing concentration of TOPO, higher solvent loading was observed when MEK and MIBK were used, with MIBK being better diluent than MEK. The degree of effectiveness of the diluents in the extraction of acetic acid from aqueous media is MIBK > MEK > Toluene > n – hexane.

ACKNOWLEDGENTS

The authors would like to acknowledge the technical staff and the project students of the Department of Chemical Engineering, Obafemi Awolowo University for the various roles played in the course of the research.

REFERENCES

Alves De Oliveira, R., Alexandri, M., Komesu, A., Venus, J., Vaz Rossell, C. E., and Maciel Filho, R. (2020). Current advances in separation and purification of second-generation lactic acid. *Separation and Purification Reviews*, *49*(2), pp. 159-175.

Araújo, E. M. R., Coelho, F. E. B., Balarini, J. C., Miranda, T. L. S., and Salum, A. (2017). Solvent extraction of citric acid with different organic phases. *Advances in Chemical Engineering and Science*, *7*(03), p.304.

Awuchi, C. G., Twinomuhwezi, H., Igwe, V. S., and Amagwula, I. O. (2020). Food Additives and Food Preservatives for Domestic and Industrial Food Applications. *Journal of Animal Health*, *2*(1), pp. 1-16.

Candido, R. G., Godoy, G. G., and Goncalves, A. R. (2017). Characterization and application of cellulose acetate synthesized from sugarcane bagasse. *Carbohydrate polymers*, *167*, pp. 280-289.

Cox, M., and Rydberg, J. (2004). Introduction to solvent extraction. In *Solvent Extraction Principles and Practice, Revised and Expanded* (pp. 13-36). CRC Press.

Das, C. K., Kumar, S., and Rath, T. (2009). 17 Vinyl Polymer Applications and Special Uses. *Handbook of Vinyl Polymers*, p. 541.

Derossi, A., Fiore, A. G., De Pilli, T., and Severini, C. (2011). A review on acidifying treatments for vegetable canned food. *Critical reviews in food science and nutrition*, *51*(10), pp. 955-964.

Djas, M., and Henczka, M. (2018). Reactive extraction of carboxylic acids using organic solvents and supercritical fluids: A review. *Separation and Purification Technology*, *201*, pp. 106-119.

Gullo, M., Verzelloni, E., and Canonico, M. (2014). Aerobic submerged fermentation by acetic acid bacteria for vinegar production: Process and biotechnological aspects. *Process Biochemistry*, *49*(10), pp. 1571-1579.

Han, S., Shin, K., Henkelman, G., and Mullins, C. B. (2019). Selective oxidation of acetaldehyde to acetic acid on Pd–Au bimetallic model catalysts. *ACS Catalysis*, *9*(5), pp. 4360-4368.

Haynes, A. (2006). Acetic acid synthesis by catalytic carbonylation of methanol. *Catalytic Carbonylation Reactions*, pp. 179-205.

Ingle, K. P., Deshmukh, A. G., Padole, D. A., Dudhare, M. S., Moharil, M. P., and Khelurkar, V. C. (2017). Phytochemicals: Extraction methods, identification and detection of bioactive compounds from plant extracts. *Journal of Pharmacognosy and Phytochemistry*, *6*(1), pp. 32-36.

Inyang, V., and Lokhat, D. (2020). Reactive extraction of malic acid using trioctylamine in 1–decanol: equilibrium studies by response surface methodology using Box Behnken optimization technique. *Scientific reports*, *10*(1), pp. 1-10.

Jones, B., Linnen, M., Tande, B., and Seames, W. (2015). The production of vinyl acetate monomer as a co-product from the non-catalytic cracking of soybean oil. *Processes*, *3*(3), pp. 619-633.

Kalck, P., Le Berre, C., and Serp, P. (2020). Recent advances in the methanol carbonylation reaction into acetic acid. *Coordination Chemistry Reviews*, *402*, 213078.

Komesu, A., Maciel, M. R. W., and Maciel Filho, R. (2017). Separation and purification technologies for lactic acid–A brief review. *BioResources*, *12*(3), pp. 6885-6901.

Kreyenschulte, D., Heyman, B., Eggert, A., Maßmann, T., Kalvelage, C., Kossack, R. and Büchs, J. (2018). In situ reactive extraction of itaconic acid during fermentation of *Aspergillus terreus*. *Biochemical Engineering Journal*, *135*, pp. 133-141.

Li, C., Gao, M., Zhu, W., Wang, N., Ma, X., Wu, C., and Wang, Q. (2021). Recent advances in the separation and purification of lactic acid from fermentation broth. *Process Biochemistry*, *104*, pp. 142-151.

Li, Z., Wang, K., Luo, X., and Xu, X. (2022). Optimization and simulation of vinyl acetate process based on Aspen Plus. In *International Conference on Optoelectronic Materials and Devices (ICOMD 2021)* (Vol. 12164, pp. 420-425). SPIE.

Lin, Y., and Tanaka, S. (2006). Ethanol fermentation from biomass resources: current state and prospects. *Applied microbiology and biotechnology*, *69*(6), pp. 627-642.

Mukherjee, S., and Munshi, B. (2020). Experimental and theoretical analysis of reactive extraction of caproic acid by using TBP in green diluents. *Chemical Engineering and Processing-Process Intensification*, *153*, 107926.

Mungma, N., Kienberger, M., and Siebenhofer, M. (2019). Reactive extraction of lactic acid, formic acid and acetic acid from aqueous solutions with tri-n-octylamine/1-octanol/n-undecane. *ChemEngineering*, *3*(2), pp. 43 – 51

Pal, D., and Keshav, A. (2014). Extraction equilibria of pyruvic acid using tri-n-butyl phosphate: Influence of diluents. *Journal of Chemical and Engineering Data*, *59*(9), pp. 2709 – 2716.

Pandey, S., and Kumar, S. (2018). Reactive extraction of gallic acid using aminic and phosphoric extractants dissolved in different diluents: effect of solvent's polarity and column design. *Industrial and Engineering Chemistry Research*, *57*(8), pp. 2976-2987.

Sas, O. G., Domínguez, I., González, B., and Domínguez, Á. (2018). Liquid-liquid extraction of phenolic compounds from water using ionic liquids: Literature review and new experimental data using [C2mim]

FSI. *Journal of environmental management*, *228*, pp. 475 – 482.

Sprakel, L. M. J., and Schuur, B. (2019). Solvent developments for liquid-liquid extraction of carboxylic acids in perspective. *Separation and purification technology*, *211*, pp. 935 – 957.

Udachan, I. S., and Sahoo, A. K. (2014). A study of parameters affecting the solvent extraction of lactic acid from fermentation broth. *Brazilian Journal of Chemical Engineering*, *31*, pp. 821 – 827.

Uslu, H. (2009). Reactive extraction of formic acid by using tri octyl amine (TOA). *Separation science and technology*, *44*(8), pp. 1784–1798.

Wasewar, K. L. (2012). Reactive extraction: an intensifying approach for carboxylic acid separation. *International Journal of Chemical Engineering and Applications*, *3*(4), pp. 249 – 258

Wasewar, K. L., and Shende, D. Z. (2011). Equilibrium for the reactive extraction of caproic acid using tri-n-butyl phosphate in methyl isobutyl ketone and xylene. *Journal of Chemical and Engineering Data*, *56*(8), pp. 3318 – 3322.

Wasewar, K. L., Shende, D., and Keshav, A. (2011). Reactive extraction of itaconic acid using quaternary amine Aliquat 336 in ethyl acetate, toluene, hexane, and kerosene. *Industrial and engineering chemistry research*, *50*(2), pp. 1003 – 1011.

Zentou, H., Zainal Abidin, Z., Yunus, R., Awang Biak, D. R., Abdullah Issa, M., and Yahaya Pudza, M. (2021). A new model of alcoholic fermentation under a byproduct inhibitory effect. *ACS omega*, *6*(6), pp. 4137-4146.

Zhang, X., Li, J., Kang, L., and Zhu, M. (2022). Theoretical study on the synthesis of vinyl acetate from acetylene and acetic acid over nonmetallic catalysts with different carbon-nitrogen ratios. *Molecular Catalysis*, *524*, 112299.

Zi, L. H., Liu, C. G., Xin, C. B., and Bai, F. W. (2013). Stillage backset and its impact on ethanol fermentation by the flocculating yeast. *Process Biochemistry*, *48*(5-6), pp. 753-758.

DOI: 10.51975/23380207som
Journal of the Nigerian Society of Chemical Engineers, 38(2), 2023

THREE-BOX SEQUENTIAL MODELLING OF THE EMISSION, DECAY AND TRANSPORTATION OF VOLATILE ORGANIC COMPOUNDS IN BEAUTY SHOPS

Atanda, S.A. [*], Adeniran, J.A., Adewoye, T. L.[1]
[1]*Department of Chemical Engineering, University of Ilorin, Nigeria*
[1*] sarat.morenikeji@gmail.com, [2] adeniran.ja@unilorin.edu.ng, [3] adewoye.tl@unilorin.edu.ng
[*]Corresponding author

ABSTRACT

The concentration of Volatile Organic Compounds (VOCs) in indoor environments such as beauty shops where numerous essential oil and scented products are used depends on their emission rate, decay and transportation. Consequently, a better understanding of the dynamic behaviour of this pollutant in the indoor environment improves estimates of human exposure to indoor air pollutants. Single-zone-based models are easy to simulate but are inadequate for predicting exposure in indoor spaces where the source of the pollutant is near. In this study, a three sequential box model which accounts for the mass transfer process in the air, emission from indoor sources, decay and transportation was developed with the assumption of perfect mixing. The dsolve package in MATLAB R2019a software was used to solve model equations. Finally, the results of the study revealed that as the VOCs concentration in the box that contains the emission source decreases the concentration in other boxes increases and has a correlation coefficient of 0.9401 with the measured value. Hence, a suitable control strategy can be developed to reduce VOCs concentration in indoor environments.

Keywords: *Indoor air quality, sequential box model, VOCs, MATLAB and validation.*

1. INTRODUCTION

Numerous researches and campaigns have been carried out across the globe to quantify, model the dynamic behaviour and determine health risks associated with exposure to Volatile Organic Compounds (VOCs) in the indoor environment. Beauty shops uses a lot of cosmetic products such as hair spray, hair dyes, shampoo, creams, lotions, mascara, perfumes, relaxers and many more which contain VOCs (Baghani *et al*., 2018). Exposure to VOCs in indoor environment where people spend more than 80% of their time (Cetin & Sevik, 2016; Höllbacher, Ters, Rieder-Gradinger, & Srebotnik, 2017; Huang *et al*., 2016; Hussain, He, Mohamad, & Tao, 2015; Liagkouridis, Cousins, & Cousins, 2014; Paciência, Madureira, Rufo, Moreira, & Fernandes, 2016) where its concentration is higher have direct impacts on human health (Attia, Swasy, Ateia, Alexis, & Whitehead, 2019; Katsoyiannis, Leva, & Kotzias, 2008; Paciência *et al*., 2016) and the environment (Hussain *et al*., 2015; Liagkouridis *et al*., 2014; Zhu, Shena, & Luo, 2020). Every year, there are about 4.2 million deaths as a result of ambient air pollution and 3.8 million deaths as a result of indoor air pollution (WHO, 2021). Given the dangers posed by VOCs both to human health and to the environment, strict regulations have been put in place to regulate VOCs by developed countries (Zhu *et al*., 2020). Effective control of the level of VOCs in indoor environment require the development of a robust model that describes the dynamic behavior of the pollutant in the indoor air.

Models account for sources of pollutants, the amounts of pollutants emitted, chemical reaction transformations, different meteorological conditions, topographical features and other factors that affect dispersion of pollutants **(**Babusiaux, 2003). Such models can be used for calculating pollutant concentrations at any given point and for experiments simulations. An air quality model can be simple or complex depending on the assumptions used in formulating them. There are two main types of VOCs models available in literature: physical (analytical) and empirical models.

Physical model is a mass transfer-based model which takes into account the inflow, outflow, deposition and emission sources of the pollutant (Hu, Zhang, Wang, & Little, 2007). Physical model when validated can predict VOC emission for a wide range of conditions using known physical parameters (Hu *et al*., 2007). Physical model can be formulated by considering the system as either one box or multibox (sequential box). One box model as shown in Figure 2.1 considers the whole space as a masks the three-dimensional variability in exposure and underestimates source proximate exposure intensity

(Oladokun & Lin, 2019). One box model presented in Equation 2.1 is suitable in cases where we have a complete mixing within the whole room or indoor space, uniform source emission and a long time frame modelling (Akintola & Sonibare, 2022; Li & Niu, 2007; Oladokun & Lin, 2019; Ryan, Splengler, & Halfpenny, 1988; Wei, Mandin, & Ramalho, 2018).

A multibox box model consists of multiple or sequential boxes as presented in Figure 1.2 which can be arranged horizontally or vertically to exhibit the characteristics of the whole system (Oladokun & Lin, 2019). The sequential box model gives option for the limitations associated with one-box models because it takes into account with preferred direction of flow and the different sources of the pollutant within each box (Ryan *et al*., 1988). Multibox model as illustrated in Equation 2.2 gives adequate information for pollutant dispersals when compared with full-scale experiments (Oladokun & Lin, 2019) and can be used in the design of predictive controllers. It consists of multiple (sequential) boxes that contain the features of a one-box model; hence, the contaminant in each box is assumed to be well-mixed. Also, each box interacts with the box next to it. Jensen *et al*. (2018) compared one-box, two-box and three-box model for aerosol dispersion, the three box model gave better estimate of the concentrations and the timing of the peaks for fluctuating concentrations. To the best of my knowledge there is no study that modeled the dynamic behavior of VOCs in beauty shops. This study focuses on the three box modeling of VOCs in indoor environment.

2. MATERIAL AND METHODS

2.1 Model Development

An unsteady state diffusion of VOCs in a typical beauty shop in Nigeria was considered in this research. Most beauty shops consist of different sections which include hair styling, manicure, massage, makeup many more. The beauty shop was divided into three boxes of equal volumes as presented in Figure 2.1 where d_1, d_2, and d_3

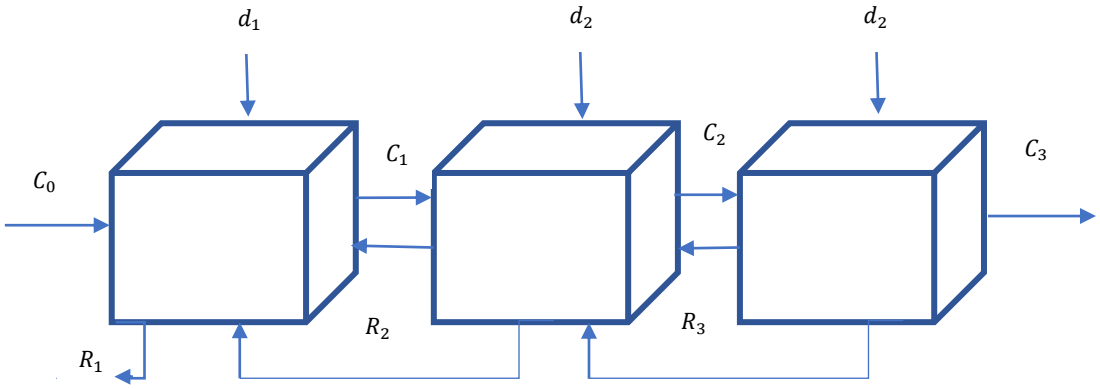

Figure 1: schematic representation of Three-box model

The following assumptions were made in the model development:

1. The boxes have equal volumes $V_1 = V_2 = V_3$
2. No interaction between the boxes that are far apart; that is there is only interaction between boxes that are beside each other.
3. Deposition in each of the boxes is considered to be negligible due to the volatile nature of the pollutant
4. Flow rate in the boxes are uniform
5. Emission of the VOC in the indoor environment is from box 1

From the first principle the differential equation which governs the generation and decay of VOCs, based on mass balance consideration as shown in Equation 1

$$\text{Rate of change pollutant} = \text{inflow from outdoor} - \text{outflow to outdoor} - \text{deposition rate} + \text{emission rate} + \text{infiltration from adjacent box} - \text{return} \quad (1)$$

The rate of change of concentration of VOCs in box 1, 2 and 3 are represented by Equations 2, 3 and 4, respectively.

$$V_1 \frac{dC_1}{dt} = C_0F_0 - C_1F_1 + e_1 - d_1 - R \quad (2)$$

$$V_2 \frac{dC_2}{dt} = C_1F_1 - C_2F_2 + e_2 - d_2 - R \quad (3)$$

$$V_3 \frac{dC_3}{dt} = C_2F_2 - C_3F_3 + e_3 - d_3 - R \quad (4)$$

Where
C_0=initial concentration of VOCs in box 1
$C_1, C_2\ and\ C_3$= concentration of VOCs leaving box 1, 2 and 3 respectively
$V_1, V_2\ and\ V_3$=volume of the box 1, 2 and 3 respectively
F_0=flowrate into the box 1 from outdoor air
$F_1, F_2\ and\ F_3$ =flowrate out of the box 1, 2 and 3, respectively
$d_1, d_2\ and\ d_3$=deposition rate in box 1, 2 and 3
R=return
e_1=emission from box 1, 2 and 3

The emission rate of VOCs in the indoor environment from the surface source to the gas phase is given by Equation 5

$$E_i = h_m A(C_s - C_i) \quad (5)$$

Where E_i is the emission from the box but for simplicity it was that the pollutant was emitted in the first box only. h_m is the specific source /air mass transfer coefficient which can be estimated with Equation 6-9. D_a represents the diffusion coefficient (m^2/s)

$$h_m = \frac{D_a}{l} \times Sh \quad (6)$$

$$Sh = 0.664 Sc^{1/3} Re^{1/2} \quad (7)$$

Where $Sc = (\frac{\mu}{\rho D_a})$ (8)

$$Re = \frac{\rho u l}{\mu} \quad (9)$$

L(m) is the length, and μ kg/ms is the dynamic viscosity of the air (Wei *et al*., 2018). The values of this parameters used in the simulation

VOCs convert spontaneously to secondary pollutants in the presence of light. we can assume that most of the emitted Semi Volatile Organic Compounds (SVOC) will sorb onto available surfaces that will act as secondary continuous sources. This chemical reaction may significantly reduce the concentration of VOCs and increase the concentration of the reaction product (Wei, Mandin, & Ramalho, 2017). Only the surface sources were considered in the model and some of the VOCs lost as a result of chemical reaction for this case was taken to be first order. The rate of disappearance of VOCs is given by Equation 10 and the rate constant was calculated from concentration data obtained in the experiment described in the next subsection.

$$R = KC_i \quad (10)$$

Considering all the parameters the general Equation becomes Equation 11

$$V_i \frac{dC_i}{dt} = C_iF_i - C_{i+1}F_{i+1} - h_m A(C_s - C_i) - KC_i \quad (11)$$

2.2 Experimental Procedure

An unhabited room (2.72 × 2.82 × 2.00) m^3 with an air conditioning unit was chosen as the experimental room because it has no major indoor and outdoor pollution generating sources except the aerosols being released from the hair spraying products. Five bestselling brands of hair spray products were used separately to carry out the experiment. Measurements were taken in the experimental room under atmospheric conditions. The hair sprays were sprayed at the centre of the room at the height of 1.5 m above the ground and the samplers were placed 40 cm away from where it is sprayed the total VOCs were measured with an insitu MultiRAE gas monitor (Model PGM50-5P) with detection limit of 0-2,000 ppm measurement of VOCs with 0.1 ppm resolution Instantaneous readings were taken initially when it was sprayed, 15 min, 1 hr, and 3hrs after spraying.

3.0 RESULTS AND DISCUSSION

3.1 MATLAB Solution of the Three-box Model

The solution to the sequential box model proposed in this study computes the spatial variation of the concentration with a time of the sequential box model using the *dsolve* (solver) package for simultaneous ordinary differential equation in MATLAB 2019a environment. The model solution was obtained for 1h and 24 h for three scenarios where the source of pollution is in one box, or two boxes and all the three boxes simulations were presented in Figures 2 and 3, respectively. The first scenario consists of three cases that are when the pollutant is either in boxes 1, 2 or 3, three cases were also considered for the second scenario which includes the pollutant emission source in boxes 1 and 2, 2 and 3 and 1 and 3. In all scenarios considered the profile of the box that contained the pollutant source showed a correlation with the experimental values obtained.

Scenario 1

Case 1: when the emission source is in box 1

The change in concentration with time when the source of the pollutant is from the first box only is presented in Figures 4.1 and 4.2 following an hour and 24 h from the

start of the VOCs emission under room temperature and pressure. It was observed from Figure 4.1that the highest concentration of the VOCs was $5.6 \times 10^5 \mu g/m^3$ and was obtained at box 1 where the VOC emission source is located. The concentration continued to decrease for about 20 mins to a value of $5.0 \times 10^5 \mu g/m^3$while boxes 2 and 3 showed a sharp rise in concentration before they begin to decrease as a result of ventilation. It was found that the concentration of the VOCs in box 2 is higher than what was obtained in box 3 because it was closer to the emission source of the VOCs. The concentration in box 2 and 3 were higher than what was obtained in box 1 between 10 to 20 mins indicating that with dispersion and photocatalytic oxidation of VOCs the concentration of areas closer to the source decreases while that farther away from the source increase as reported by Davardsoot and Kahfooroushan (2018). The concentration of VOCs became stable with time in each of the boxes.

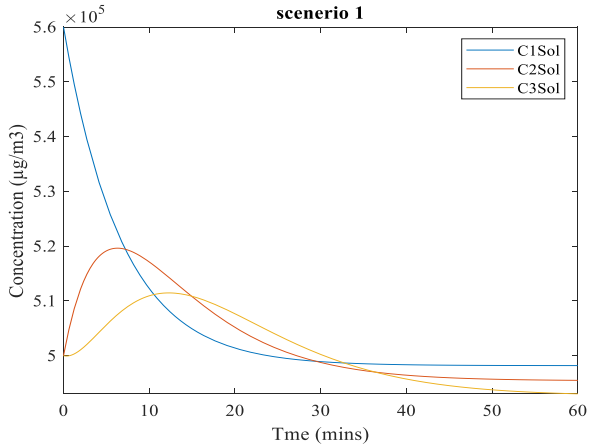

Figure 2: Predicted concentration up to 1h

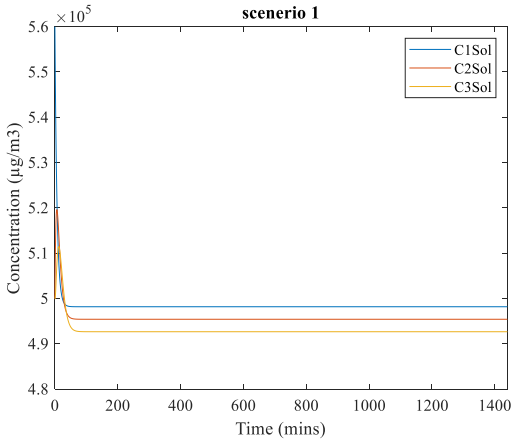

Figure 3: Predicted concentration up to 24h

Case 2: when the pollutant emission source is in box 2

When the emission source was in the second box only the result obtained for the simulation was shown in Figures 4 and 5 following an hour and 24 hours from the start of the VOCs emission under atmospheric conditions. As observed in case 1 the highest concentration was obtained in box 2 as shown in Figures 6 and 7 The concentration value declined for about 15 mins while box 3 showed a sharp rise in concentration before they begin to decrease due to ventilation. The concentration VOC on the other hand in Box1 showed only a slight difference, this can be attributed to the preferred direction of wind flow (Ryan *et al*., 1988) and photocatalytic degradation of the VOCs in that box.

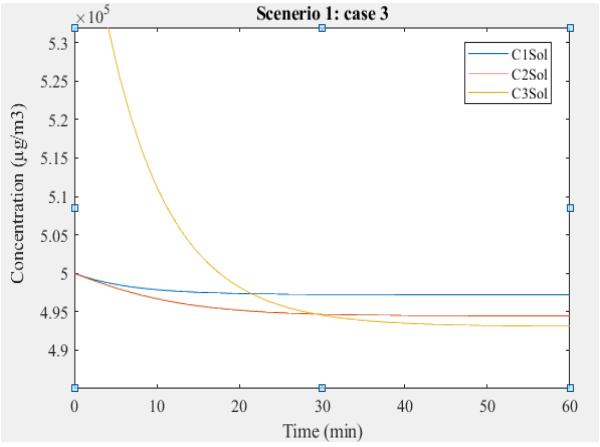

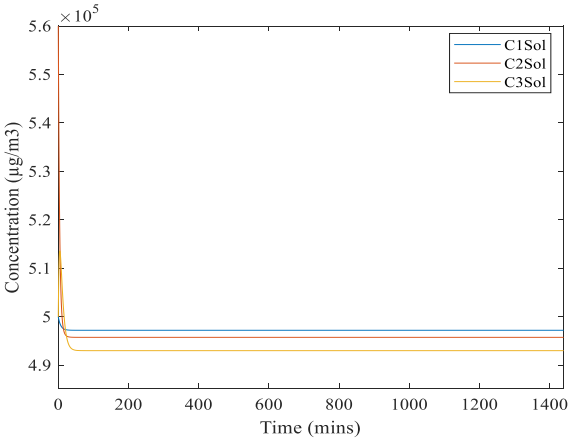

Figure 4: Predicted concentration up to 1hr Figure 5: Predicted concentration up to 24h

Case 3: when the pollutant source is in box 3

Figures 6 and 7 showed when the source of pollutant in box 3 it was observed that box 3 showed a decrease in

concentration while boxes 1 and 2 did not show a significant difference in concentration which can also be attributed to the direction of air. It can be deduced from this result that The dispersion of VOCs has a strong relationship with the ventilation and airflow because it is the only means of mixing the VOCs in confined spaces apart from convection. The result obtained from this study agrees with the findings of Jensen *et al*. (2018).

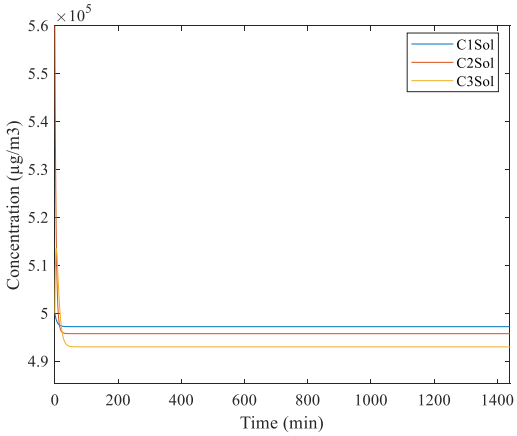

Figure 6: Predicted concentration for 1h

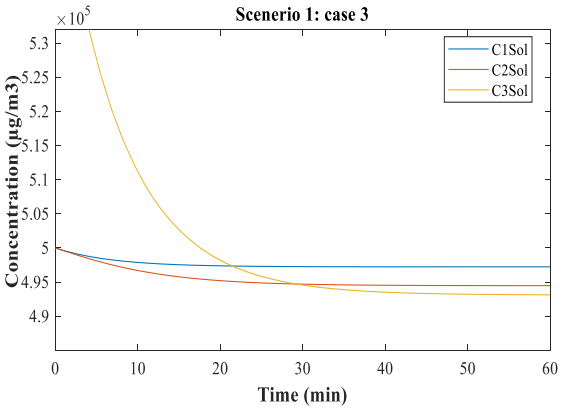

Figure 7: Predicted concentration for 24h

Scenario 2 (emission source is from two boxes)

The solution obtained when the source of the pollutant is in boxes 1 and 2 is presented in Figures 4.7 and 4.8. the concentration of VOCs decreased until it attained a steady state at about 25 mins. A sharp rise was observed in box 3 until there was a decrease in the concentration.

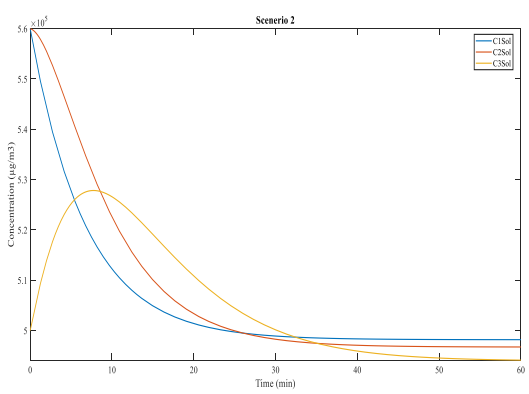

Figure 8: Predicted concentration up to 1h

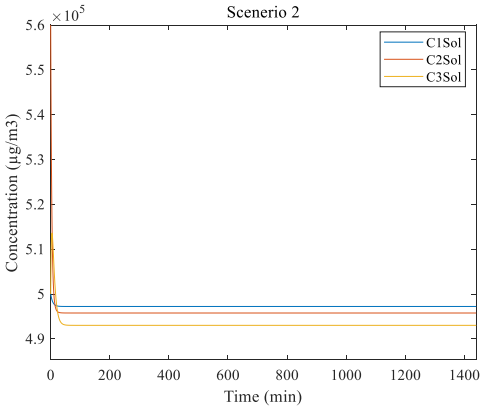

Figure 9: Predicted concentration up to 24h

Scenario 3 emission source is from three boxes

The concentration of VOCs as shown in Figure 4.10 and 4.11 obtained in scenario 3 decreased slowly in boxes 1 and 2 up to 10 mins before attaining a steady state. There was a sharp decrease in box 3 on the other hand which can be attributed to its closeness to a ventilation source.

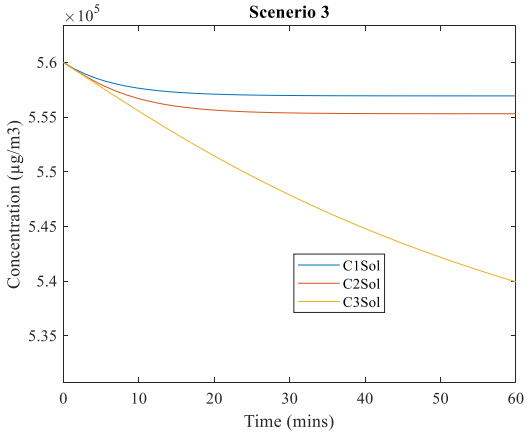

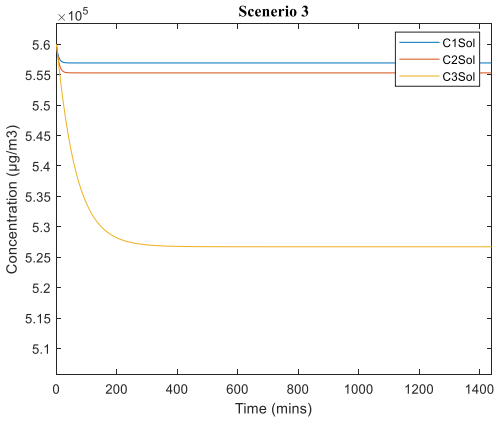

Figure 10: Predicted concentration up to 1h **Figure 11: Predicted concentration up to 24h**

The measured concentration from the experiment and predicted concentrations from the model developed are shown in Figure 12. The Pearson's correlation coefficient (R^2) was obtained to be 0.9401 indicating a strong association between the VOCs concentration measured and predicted concentration. The concentration profile to what was obtained for all scenarios is similar to what was obtained in the experiment which conform with what was obtained by Jensen *et al*. (2018). It can be deduced that the predicted concentration from the three boxes agrees with the measured concentration from the experimental room. The performance of the three-box model may be ascribed to exchange velocity and other dynamical parameters (Dai, Cai, Zhong, & MacKenzie, 2021). An increase in the number of local concentration gradients gives a better description of the flux balance in the multi-box model and better modelling results.

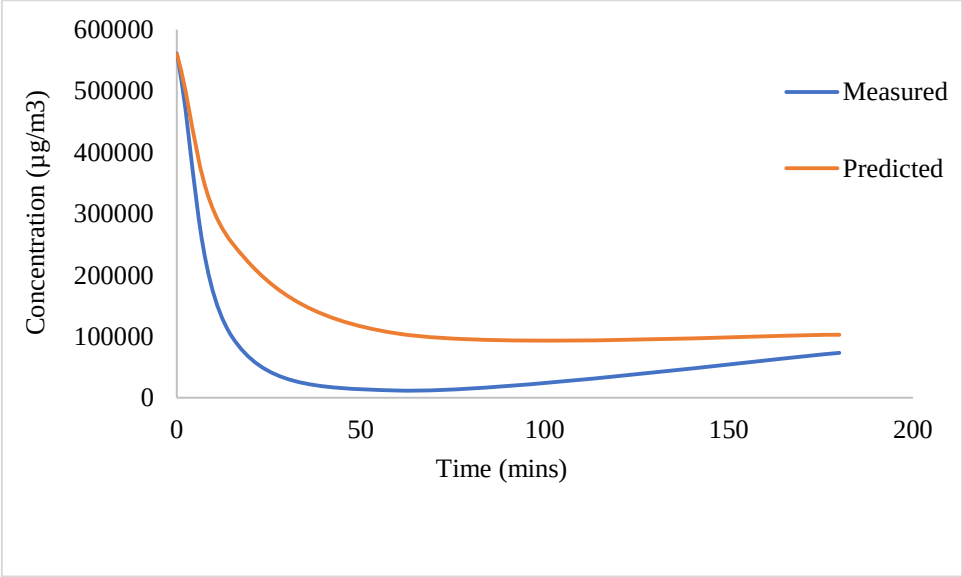

Figure 12: Measured and predicted concentration of VOCs

4. CONCLUSION

Sequential box models can be used to quantify the effect of air pollutants on human health and design/propose a suitable control strategy. Ordinary Differential Equations with a solution of concentrations varying with time can give an insight into the dynamic behaviour of VOCs in an indoor environment. These model equations developed contain either emission or reaction term or both terms using the mass balance approach. The *dsolve* solver in Matlab 2019a gave a result which has the same profile as the experimental results obtained in the experimental room considered in this study in obtaining numerical solutions when studying the dynamic behaviour of VOCs in confined spaces. The concentrations of air pollutants decrease with time in the box that contains the emission source and remains constant at a point when a steady state is attained. The boxes that did not contain the emission showed a rise and then reduced gradually until a steady state is

attained. The dispersion of the VOCs was through a preferred direction of flow. Further study should be carried out on the influence of different ventilation modes

REFERENCES

Akintola, O., & Sonibare, J. (2022). Advection-diffusion model for indoor-outdoor exchange of air pollutants from electric power generators servicing buildings. *Cogent Engineering, 9*(1), 2076321.

Attia, M., Swasy, M., Ateia, M., Alexis, F., & Whitehead, D. (2019). Periodic mesoporous organosilica nanomaterials for rapid capture of VOCs. *communication*, 1-3.

Babusiaux, D. (2003). Allocation of the CO2 and Pollutant Emissions of a Refinery to Petroleum Finished Products. *Oil & Gas Science and Technology, 58*(6), 685-695.

Baghani, A. N., Rostami, R., Arfaeinia, H., Hazrati, S., Fazlzadeh, M., & Delikhoon, M. (2018). BTEX in indoor air of beauty salons: risk assessment, levels and factors influencing their concentrations. *Ecotoxicology and Environmental Safety, 159*, 102-108.

Cetin, M., & Sevik, H. (2016). Measuring the impact of selected plants on indoor co_2 concentrations. *Polish Journal of Environmental Studies, 25*(3), 973-979.

Dai, Y., Cai, X., Zhong, J., & MacKenzie, A. R. (2021). Modelling chemistry and transport in urban street canyons: Comparing offline multi-box models with large-eddy simulation. *Atmospheric Environment, 264*, 118709.

Davardsoot, F., & Kahfooroushan, D. (2018). Modelling the dispersion of Volatile Organic Compounds in indoor environment. *chemical engineering and technology*, 1-22.

Höllbacher, E., Ters, T., Rieder-Gradinger, C., & Srebotnik, E. (2017). Emissions of indoor air pollutants from six user scenarios in a model room. *Atmospheric Environment, 150*, 389-394.

Hu, H. P., Zhang, Y. P., Wang, X. K., & Little, J. C. (2007). An analytical mass transfer model for predicting VOC emissions from multi-layered building materials with convective surfaces on both sides. *International Journal of Heat and Mass Transfer, 50* 2069–2077.

Huang, Y., Hang, S. S., Lu, Y., Niu, R., Xu, L., Cao, J., & Lee, S. (2016). Removal of Indoor Volatile Organic Compounds via Photocatalytic Oxidation: A Short Review and Prospect. *molecules, 21*(56), 1-20.

Hussain, M., He, Y.-L., Mohamad, A. A., & Tao, W.-Q. (2015). A new hybrid algorithm for numerical simulation of VOC emissions using single-layer and multilayer approaches *Taylor and Francis, 67*, 211-229.

Jensen, A. C., Dal Maso, M., Koivisto, A. J., Belut, E., Meyer-Plath, A., Van Tongeren, M., . . . Toftum, J. (2018). Comparison of geometrical layouts for a multi-box aerosol model from a single-chamber dispersion study. *Environments, 5*(5), 52.

Katsoyiannis, A., Leva, P., & Kotzias, D. (2008). VOCs and carbonyl emmision from carpets: A comparative study using four types of environmental chambers. *Journal of hardardous material, 152*, 671-675.

Li, F., & Niu, J. (2007). Control of volatile organic compounds indoors—development of an integrated mass-transfer-based model and its application. *Atmospheric Environment, 41*(11), 2344-2354.

Liagkouridis, L., Cousins, I. T., & Cousins, A. P. (2014). Emmisions and fate of brominated flame retardant in indoor environment: A critical review of modelling approaches. *Elsevier*, 1-20.

Oladokun, M., & Lin, Z. (2019). Dynamic sequential box modelling of inhalation exposure potential in multibed patient ward: Validation and baseline case studies. *Building and Environment, 161*(106241), 1-14.

Paciência, I., Madureira, J., Rufo, J., Moreira, A., & Fernandes, E. d. O. (2016). A Systematic Review of Evidence and Implications of Spatial and Seasonal Variations of Volatile Organic Compounds (VOC) in Indoor Human Environments *Journal of toxicology and environmental Health*, 1-15.

Ryan, B., Splengler, J., & Halfpenny, P. (1988). Sequential box model for indoor air quality: application to airliner cabin quality *Atmospheric Environment, 22*(6), 1031-1038.

Wei, W., Mandin, C., & Ramalho, O. (2017). Reactivity of semivolatile organic compounds with hydroxyl radicals, nitrate radicals, and ozone in indoor air. *International Journal of Chemical Kinetics, 49*(7), 506-521.

Wei, W., Mandin, C., & Ramalho, O. (2018). Influence of indoor environmental factors on mass transfer parameters and concentrations of semi-volatile organic compounds. *Chemosphere, 195*, 223-235.

WHO. (2021). Air pollution. Retrieved from https://www.who.int/health-topics/air-pollution#tab=tab_1

Zhu, L., Shena, D., & Luo, K. (2020). A critical review on VOCs adsorption by different porous materials: Species, mechanisms and modification methods *Journal of Hazardous Materials, 389*(122102), 1-23.

DOI: 10.51975/23380208som
Journal of the Nigerian Society of Chemical Engineers, 38(2), 2023

REDUCTION OF COD FROM TANNERY WASTEWATER USING CNTS MODIFIED *ALBIZIA LEBBECK* PODS

***Adewoye, T. L. [1,4], Omari, S.[1], Atanda, S. A. [1], Ogunleye, O. O.[2], Salawudeen, T.O.[2], Abdulkareem, A. S.[3,4] and Mustapha, S. I.[1]**

[1] *Department of Chemical Engineering, University of Ilorin, PMB 1515 Ilorin, Kwara Nigeria*
[2] *Department of Chemical Engineering, Ladoke Akintola University, PMB 4000 Ogbomoso, Oyo State*
[3]*Department of Chemical Engineering, Federal University of Technology, PMB 65 Minna, Niger State, Nigeria*
[4] *Nanotechnology Research Group, Africa Centre of Excellence for Mycotoxin &Food Safety, Federal University of Technology, PMB 65 Minna, Niger State, Nigeria*
[1,4]adewoye.tl@unilorin.edu.ng,[1]salimaaomari@gmail.com, [1*]sarat.morenikeji@gmail.com, [2] ooogunleye@lautech.edu.ng, [2]tosalawudeen@lautech.edu.ng, [3,4]kasaka2003@futminna.edu.ng, [1]mustapha.si@unilorin.edu.ng

[*]Sarat Ayodele ATANDA

ABSTRACT

Tannery effluent, which contains a large quantity of organic and inorganic contaminants has a detrimental effect on health and the environment when discharged directly into the water bodies. The adsorption potential of unmodified and modified carbonized Albizia Lebbeck pods for the reduction of chemical oxygen demand (COD) in tannery wastewater was investigated in this study. Albizia Lebbeck pods were carbonized and modified with purified carbon nanotubes (CNTs) to produce carbonized Albizia Lebbeck (ALC) and modified Albizia lebbeck (MALC) adsorbents. The developed adsorbents were characterized by Brunauer–Emmett-Teller (BET), high-resolution scanning electron microscopy (HRSEM), energy dispersive X-ray spectrometry (EDS) and X-ray diffraction (XRD). The batch adsorption process was conducted to investigate the effect of, pH, contact time, adsorbent dosage and temperature on the uptake of COD from tannery wastewater onto the adsorbents. The BET surface area of the ALC and MALC were 638 and 616 m^2/g, respectively. HRSEM revealed that the adsorbents have good morphology while the XRD showed that the adsorbents are highly crystalline. The maximum adsorption efficiency of MALC and ALC are 95 and 93%, respectively. It can be deduced that modification of carbonized Albizia Lebbeck (ALC) with CNT slightly improved the adsorption potential of the ALC adsorbent.

Keywords: *Tannery, Wastewater, COD, Adsorption and Albizia lebbeck*
.

1. INTRODUCTION

Water is a significant natural resource used for drinking and other purposes in our daily lives hence, the need for the availability of pure water (Haseena, Malik, Javed, Arshad, & Asif, 2017). About 80% of the world's population is facing threats from polluted water (Owa, 2013). Leather tanning involves the use of a large quantity of water and chemicals which result in the generation of toxic effluent which poses a threat to the nearby ecosystem and humans (Barman, Juel, & Hashem, 2016; Muhammad, Rakhshan, Ikhtiar, & Asma, 2015). The wastewater generated by tanning industries is usually dark brown and contains microorganisms, heavy metals, organic pollutants, and toxic chemicals which vary based on the chemicals used in the tanning process (Durai & Rajasimman, 2011). Tannery wastewater is characterized by its salinity, conductivity, high chemical oxygen demand (COD), high biological oxygen demand (BOD), inorganic matters, suspended solids (SS), total dissolved solids (TDS), heavy metals and organic pollutants which are recognized as a serious environmental threat due to high chemical levels. COD is the total measurement of all chemicals in the water that can be oxidized and the high COD concentrations in wastewater are toxic to biological life and will affect the aquatic environment such as aquatic plants and fishes (Nayl *et al*., 2017), it is therefore important to treat the effluents from the tannery industry before discharging them into the environment.

A large number of researchers used conventional methods for the reduction of COD from wastewater

(Ademiluyi, Amadi, & Amakama, 2009; Badalians Gholikandi, Baneshi, Dehghanifard, Salehi, & Yari, 2010; Mustapha *et al*., 2019). Out of all the methods, the adsorption technique is simple, has low cost and reduces the generation of secondary pollutants (Olufemi, 2018). Different adsorbents have been used for adsorption which includes activated carbon (Ademiluyi *et al*., 2009), silica gel (Yan & Wang, 2018), zeolite (Badalians Gholikandi *et al*., 2010) and lots more. The major shortcoming in using some of these adsorbents is the cost of production (Gawande & Kaware, 2016), hence, there is a need to use an alternative material such as an adsorbent derived from agricultural waste for the reduction of COD from tannery water.

Agricultural waste is an alternative because they are inexpensive, abundant in nature, and readily available waste material from the waste industry (Dai *et al*., 2018). Some of the agricultural waste material that has been explored includes Rice husk (Mohamed & Alfalous, 2020), Sugarcane bagasse (Karnitz Jr *et al*., 2007), Wheat bran (Özer, 2007) and maize cob (Opeolu, 2009). However, these agricultural wastes have limitations as their unmodified forms have low adsorption capacities, it is, therefore, necessary to modify them before they are used as adsorbents. Carbon Nanotubes (CNTs) have been reported to have wide specific surface areas, hollow and layered structures which make them a perfect adsorption material for wastewater treatment (Kumar & Saravanan, 2018; Moosa, Ridha, M., & Abdullha, 2015). The application of CNTs is limited by their cost, nevertheless, it can be employed to modify the agricultural waste adsorbent to improve the adsorption efficiency.

This work focuses on the use of purified CNTs modified *Albizia Lebbeck* pod to efficiently reduce COD from tannery wastewater. The objectives of this research are; to purify carbon nanotubes (MWCNTs), and modify carbonized *Albizia Lebbeck* pods with the purified MWCNTs.

2. MATERIAL AND METHODS

2.1 Collection of Samples

The *Albizia Lebbeck* seed pods used in this study were collected from Mimosa trees around the Oke-Odo area, Ilorin, Kwara State. The seeds were removed from the pods and the pods were washed with distilled water to remove dust and other adhering impurities after which the washed pods were air-dried. The tannery wastewater sample was collected from a tannery in Zaria, Kaduna State. The water sample was collected in a sealed sterile plastic container and then placed in a refrigerator at 4°C for further use.

2.2 Characterization of Tannery Wastewater Sample

The pH, turbidity, COD, BOD, colour, heavy metals, TDS and conductivity of the wastewater sample were determined. The COD and BOD were carried out using standard procedures (Nayl *et al*., 2017). The pH was determined using a pH meter. Turbidity, TDS, and conductivity were determined using the Turbidity meter, TDS meter and Conductivity meter, respectively.

2.3 COD Analysis

About 5 ml each of $K_2Cr_2O_7$ was added to the wastewater sample and distilled water in a conical flask in triplicate. The six flasks were kept in a boiling water bath (100°C) for an hour and then allowed to cool. Potassium iodide (5 ml) was added to all six flasks and then 10 ml of H_2SO_4. The contents of each flask were titrated with 0.1(M) $Na_2S_2O_4$ until it turns yellow. After which, 1 ml of starch solution was added to all the flasks until the solution turned blue. The sample obtained was then titrated with 0.1 (M) sodium thiosulphate endpoint until the blue colour disappeared. The COD was calculated with Equation 1.

$$COD = \frac{(A-B)*N*8000}{S} \qquad 1$$

Where; COD represents COD in the sample in mg/litre, B is the volume in ml of the titrant used for the sample, A is the volume in ml of titrant used as blank, S represents the volume of the water sample and N is the normality of sodium thiosulphate.

2.4 Purification of CNT

The procured CNT was purified to remove residual metals and other impurities absorbed in the CNTs (Egbosiuba, 2022). The CNT was purified with a mixture of acetic acid and sulphuric acid in the ratio of 3:1 (V/V); 100 mg of CNTs was poured into the prepared mixture and the sample was then placed in a sonicator for 3 h at 30°C. After which the mixture was brought out and washed with distilled water till a pH of 7 was attained. It was then filtered and oven-dried at 110°C. The obtained purified CNT (A.N CNT) was stored in an airtight, sterile sample bottle for further use.

2.5 Preparation, Modification and Characterization of *Albizia Lebbeck* adsorbent

The obtained *Albizia Lebbeck* sample was ground into powder, sieved using a sieve size of 225 µm, and washed again with distilled water until the colourless filtrate was attained to remove any traces of absorbed salt (Ullah *et al*., 2019). The residue gotten from the filtration was then dried in an oven at 105°C for 8 h (Ibrahim & Umar, 2016). The dried

sample was calcined in a muffle furnace at 550 ºC for 3 h to obtain carbonized *Albizia Lebbeck* pods (ALC)

For the modified adsorbent, ALC sample (5.0 g) was dispersed in 250 ml of ethanol solution and sonicated for 10 mins, then 0.05 g of purified MWCNTs (1% weight) was added into the mixture and it was further sonicated for 20 mins (Parlayici, Eskizeybek, Avcı, & Pehlivan, 2015). It was then filtered and placed in an oven to dry at 80℃ for 3 h. The obtained (sample MALC) was then placed in a desiccator for the adsorption experiment. The obtained samples were characterized for their surface morphologies/composition, surface area, functional group and crystallinity using Zeiss Auriga HRSEM, NOVA 4200e surface area and pore size analyser, PerkinElmer FTIR spectrometer and XRD spectrometer.

2.6 Batch Adsorption Experiments

Batch adsorption studies were conducted to examine the effect of contact time, temperature, adsorbent dosage and pH on the reduction of COD using modified *Albizia Lebbeck* carbon (MALC) and unmodified *Albizia Lebbeck* carbon (ALC). 100 ml of the wastewater sample was taken into 250 ml Erlenmeyer flasks in several places. The kinetics of the adsorption experiment was studied at different time intervals (5-30 min) using 0.5 g of adsorbents. Different doses of adsorbents ranging from 0.5 – 0.9 g were separately mixed with 100 ml of wastewater sample put into 250 ml Erlenmeyer. The effect of temperature was investigated at different temperatures ranging from 30-50℃. The effect of pH was also studied by varying the pH of the water sample (4-12) either with 0.1 M NaOH or 0.1M H_2SO_4. The mixture was shaken constantly using a water bath shaker at 150 rpm. The mixture obtained was filtered and the residual concentration of the COD content was then analyzed and the reduction efficiencies were determined using Equation (2).

$$\% \text{ removal} = \frac{C_0 - C_e}{C_0} \times 100 \qquad 2$$

Where, C_0 and C_e (mg/l) are the concentration of COD present in the tannery wastewater sample at the initial stage and equilibrium, respectively. The equilibrium amount (Q_e) of COD removed per mass of adsorbent was evaluated using equation 3.

$$Q_e = \frac{(C_0 - C_e)V}{W} \times 100 \qquad 3$$

Where; Qe (mg/g) is the amount of metal ions adsorbed per unit mass of adsorbent at equilibrium. V(l) is the volume of the solution and W(g) is the mass of the adsorbent used.

2.6.1 Adsorption isotherm model

The equilibrium relationship between the adsorbate concentration in the solution and on the surface of the adsorbent at a specified condition is described through adsorption isotherm models. Langmuir, Freundlich and Temkin isotherm models were used to describe the equilibrium characteristic of both adsorbents in this adsorption study.

3. RESULTS AND DISCUSSION

3.1 Characterization of Wastewater Sample

Analysis was carried out on the tannery wastewater (TW) to determine its BOD, COD, pH, conductivity, TDS and heavy metals using a standard method. The results showed that BOD, Zinc, Copper, Manganese, Iron and pH were within the permissible limits set by Federal Environmental Protection (FEPA), on the other hand, COD (1200 mg/l), TDS (10400 mg/l) and Lead (0.2 mg/l) were above the permissible limit for the discharge of wastewater into surface water. The results obtained were similar to the results reported (Hossain *et al., 2019)* for tannery wastewater. High COD values of the effluent may indicate the high organic pollution potential of the effluent (Hossain *et al*., 2019). Hence, this research is concentrated on reducing the concentration of COD as their high concentration in the effluent impacts lives negatively when discharged into surface water without treatment.

3.2 Characterization of the Adsorbents

Purified CNTs (A.N CNT), calcined *Albizia Lebbeck* pods (ALC) and the modified calcined *Albizia Lebbeck* pods (MALC) were characterized for the surface area using BET analysis and the result is presented in Table S1. The result revealed that the adsorbents had a large area of 799, 638 and 616 m^2/g for A.NCNT, ALC and MALC, respectively which indicates a high adsorption capacity (Okeola, Odebunmi, & Ameen, 2012). The result obtained was similar to what was reported by Liu, Sun, Xu, Qu, and Qu (2020). The average pore size of the adsorbents were in the range of 6.181-6.247 nm which appears to be mesoporous (2-50 nm). It was also observed that the surface area of MALC was a bit lower than that of ALC. This observation may be a result of the formation functional group on the surface of MALC due to the incorporation of the CNT.

A High-Resolution scanning electron microscope was used to study the morphology/composition of the adsorbents and the results are presented in Figure 1. The HRSEM images showed a densely wormlike structure of CNTs and the tubes could be seen in Figure 1a. The HRSEM results for ALC are shown in Figure 1b, and it is seen to have an irregular sheet-like morphology which is similar to the HRSEM results of the activated *Albizia Lebbeck* reported by Ullah *et al*. (2019).

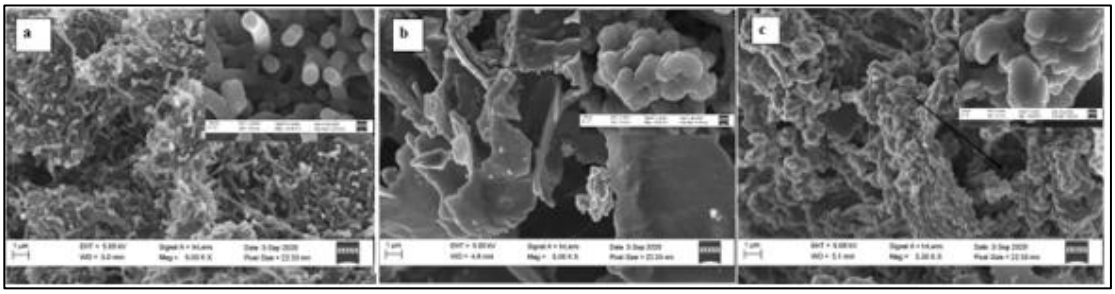

Figure 1: HRSEM images for (a) A.N CNT (b) ALC (c) MALC

The HRSEM results obtained for MALC (Figure 1c) showed irregular aggregate morphology with large pore openings (arrow) which may be a result of the modification. This irregular texture may be responsible for the observed improved stability and reduction efficiency of the MALC adsorbent presented in the subsequent section.

The Energy Dispersive X-ray Spectroscopy (EDX) results presented in Figure 2 showed that carbon is dominantly present in the three adsorbents. A.N CNT is seen to contain some other elements which could be remnants of its impurities. There was a slight increase in the Carbon weight in MALC which could be attributed to the modification with A.N CNT. The results also revealed that ALC and MALC adsorbents have oxygen-containing functional groups which may act as active sites for the adsorption of COD.

X-ray Diffraction (XRD) studies show variations in the crystallinity of the adsorbents and Figure 3 depicts the XRD spectra for the ALC and MALC adsorbents.

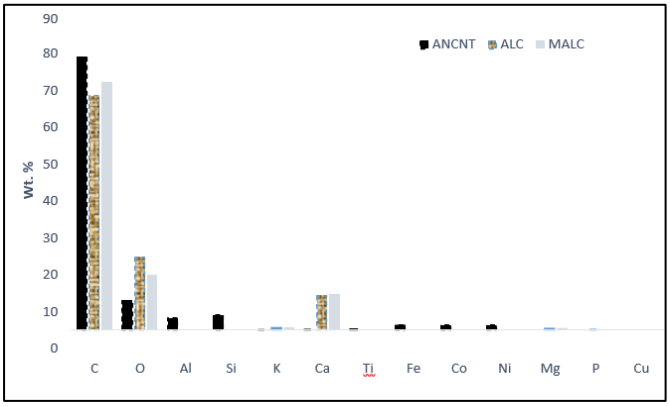

Figure 2: EDX results for A.N CNT, ALC and MALC

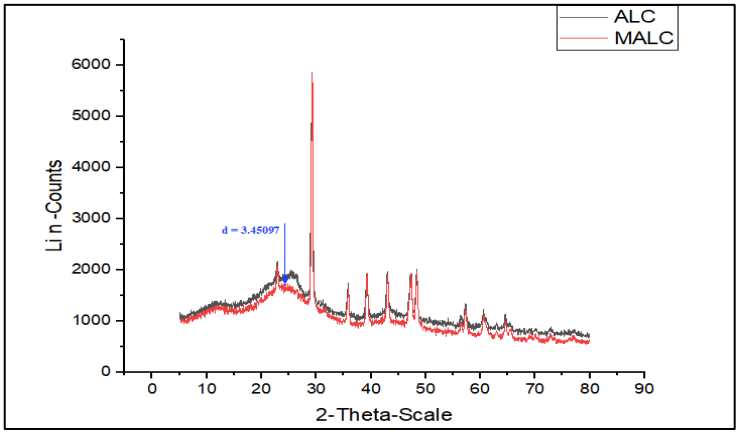

Figure 3: XRD spectra of ALC and MALC

It was observed that well-defined peaks of both adsorbents around 2θ of 29.5 (002) show the crystalline nature of the developed adsorbents. The intensity of the peak CNTs around 2θ of 29.5 (002) planes was higher in the modified adsorbent than the unmodified adsorbent and, the d-spacing of 3.45097 corresponding to CNT observed in the XRD spectral of MALC adsorbent confirmed that A.N CNT was well incorporated into the matrix of MALC adsorbent which is in agreement with the HRSEM result (Das *et al*.,2014).

3.3 Batch Experiment Studies

The effect of adsorption process parameters such as pH, contact time, adsorbent dosage and solution temperature on the efficiency of ALC and MALC adsorbents for the reduction of COD from tannery wastewater was investigated and the results are depicted in Figure 4. The effect of pH on the adsorption of COD was studied by carrying out the adsorption process at different pH values under constant adsorbent dosage (0.5g) and contact time (20 min). It was observed from Figure 4a that as pH increases, the reduction efficiency of COD increased for both adsorbents and maximum reduction was achieved at a pH of about 6 corresponding to 86 and 88% for ALC and MALC, respectively. Generally, at a low pH, the positively charged H^+ ions are high and they tend to bind to the adsorbents by electrostatic adsorption of both H^+ and oxygen and have a strong affinity for each other to take up the binding sites. However, when the pH was increased beyond 6, the removal rate of COD decreased as a result of the abundance of OH- ions, using higher hindrance to diffusion of organics contributing to COD.

The effect of time was studied in the range of 5-30 min using 0.5 g of adsorbents at 30°C. The results obtained from the studies showed that the sorption efficiency of the two adsorbents was instantaneous as more than 70% of COD was adsorbed at the initial stage, an indication that the two adsorbents have very good potential for the reduction of COD from Tannery wastewater. The sorption efficiency increased considerably with time and at approximately 20 mins, equilibrium was reached as a further increase in time caused a decrease in the reduction of COD. The maximum reduction efficiencies were 85 and 87% for ALC and MALC, respectively. The decrease in reduction efficiency observed in Figure 4b may be due to the filling of pores of adsorbents with water molecules (Parlayici *et al*., 2015). Hence, the retention time of 20 mins was chosen as the optimum time in this study. In addition, MALC showed a slightly higher maximum adsorption efficiency and better stability compared to ALC under the same batch adsorption conditions. The enhanced stability and adsorption efficiency may be due to the improved morphology of the MALC as shown in Figure 1(c).

The effect of ALC and M.ALC dosage on the percentage reduction of COD was studied at 30°C for 20 min. The adsorbent dosage was varied from 0.5 - 0.9g/100 ml as shown in Figure 4b. It was observed that the reduction efficiency increased with increasing adsorbent dose until the optimum dosage of 0.8 g/100 ml for MALC and 0.7 g/100 ml for ALC corresponding to 95 and 93%, respectively. The increase in the reduction efficiency may be ascribed to the increase in the functional groups and the total surface area of the adsorbents due to the increase in dosage, and hence, more active sites on the adsorbents were available for the adsorption of COD from the wastewater (Jain, Garg, & Kadirvelu, 2010). The decrease in removal efficiency observed with further increase in dosage (Figure 4c) was probably due to the aggregation of adsorbent as adsorbent dosage increases and therefore, the accessible adsorption sites might decrease as well due to the adsorption density (Edet & Ifelebuegu, 2020). Comparing both adsorbents, it could be seen that both adsorbents showed good performances with MALC adsorbents having a slightly higher COD reduction efficiency. the improved morphology of the MALC as shown in Figure 1(c).

The temperature has strong effects on the intermolecular forces between the adsorbate and adsorbent particles. From Figure 4d, it is seen that the rate of reduction of COD decreases as the temperature increases for both adsorbents which indicated that the adsorption is exothermic (Edet & Ifelebuegu, 2020). The decrease in adsorption capacity is due to the fact that at low temperatures, the kinetic energy of the particle is low and the intermolecular attractive forces are strong, hence, the molecules of the adsorbate are easily and strongly attracted to the surface of the adsorbent which gives a higher adsorption efficiency and vice versa.

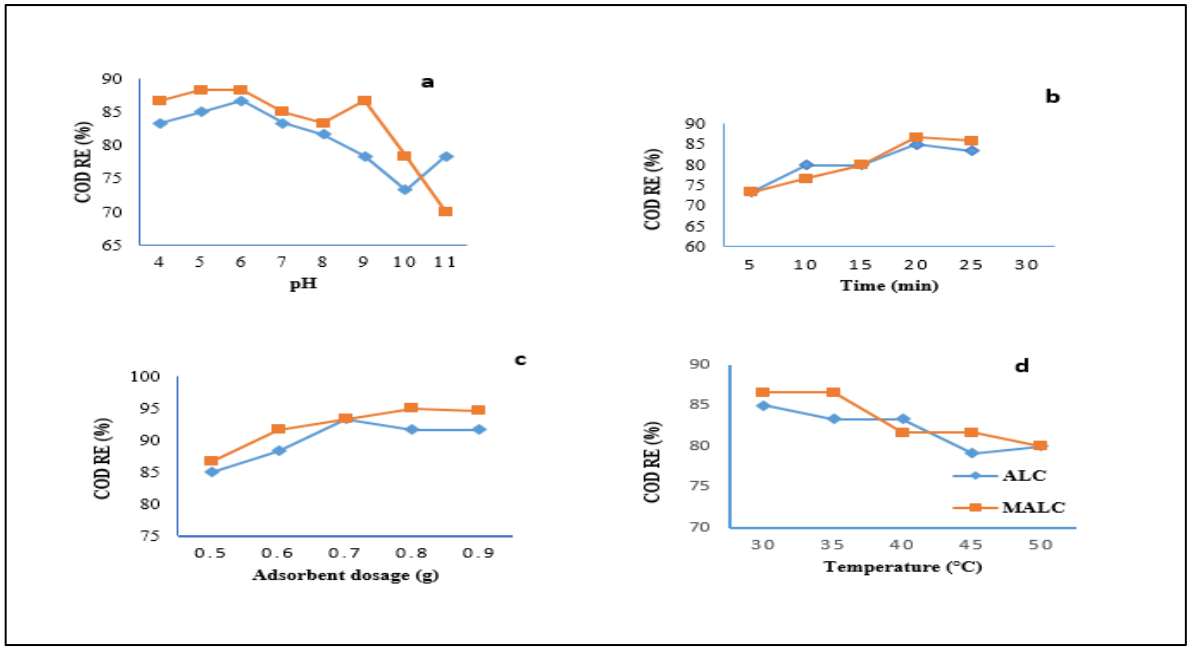

Figure 4: Effect of (a) pH (b) contact time (c) adsorbent dosage and (d) Temperature on the reduction efficiency of COD using ALC and MALC.

3.4 Adsorption Isotherms

The relation between COD adsorption capacities (Q_e) with ALC and MALC and the residual amounts (Ce) of COD at equilibrium was analyzed with different isotherm models at a constant temperature. Linear plots of Langmuir, Freundlich and Temkin are shown in Figures S3, S4 and S4 and the goodness-of-fit of the isotherms was accessed by R^2. Table S3 shows that Langmuir had the best R^2 (0.8957 for ALC and 0.9364 for MALC) values for the reduction of COD for both adsorbents which indicated a physical sorption mechanism (physisorption) (Edet & Ifelebuegu, 2020).

4. CONCLUSION

This study presented the preparation and modification of carbonized *Albizia Lebbeck* pods (ALC) as adsorbents for the reduction of COD in tannery wastewater. The results obtained revealed that the

properties of the ALC adsorbent were enhanced after the modification. The pore structure and surface area of the ALC were altered after modification with purified MWCNTs. HRSEM image of the MALC adsorbent revealed visible large pore openings resulting from the modification with MWCNTs. The XRD results confirmed that MALC showed a better crystallinity after the modification. The studies demonstrated that activated carbon prepared from *Albizia Lebbeck* can be used as an effective, low cost and natural adsorbent for the adsorption of COD from tannery wastewater. However, MALC showed slightly better efficiency removal, probably due to its modification with purified CNT. In addition, MALC showed better stability, morphology and crystallinity. The results of the batch experiments showed that the adsorption process was dependent on adsorbent dose, contact time, solution pH, and temperature.

REFERENCES

Ademiluyi, F., Amadi, S., & Amakama, N. J. (2009). Adsorption and Treatment of Organic Contaminants using Activated Carbon from Waste Nigerian Bamboo. *Journal of Applied Sciences and Environmental Management, 13*(3).

Badalians Gholikandi, G., Baneshi, M. M., Dehghanifard, E., Salehi, S., & Yari, A. R. (2010). Natural zeolites application as sustainable adsorbent for heavy metals removal from drinking water. *Iranian Journal of toxicology, 3*(3), 302-310.

Barman, B. C., Juel, M. A. I., & Hashem, M. A. (2016). *Tannery Wastewater Treatment by Simple Coagulation-Filtration Process Using Low Cost Coagulants.* Paper presented at the International Conference on Mechanical, Industrial and Energy Engineering.

Dai, Y., Sun, Q., Wang, W., Lu, L., Liu, M., Li, J., . . . Xu, J. (2018). Utilizations of agricultural waste as adsorbent for the removal of contaminants: A review. *Chemosphere, 211*, 235-253.

Durai, G., & Rajasimman, M. (2011). Biological treatment of tannery wastewater-a review. *Journal of Environmental science and Technology, 4*(1), 1-17.

Edet, U. A., & Ifelebuegu, A. O. (2020). Kinetics, isotherms, and thermodynamic modeling of the adsorption of phosphates from model wastewater using recycled brick waste. *Processes, 8*(6), 665.

Egbosiuba, T. (2022). Incorporation of zero-valent silver and polyvinyl acetate on the surface matrix of carbon nanotubes for the adsorption of mercury and chromium from industrial wastewater. *Nigerian Journal of Technology, 41*(1), 158–168-158–168.

Gawande, P. R., & Kaware, J. P. (2016). Preparation and activation of activated carbon from waste materials-a review. *International Journal for Research in Applied Science and Engineering Technology, 4*(12), 1-4.

Haseena, M., Malik, M. F., Javed, A., Arshad, S., & Asif, N. (2017). Water pollution and human health. *Health, 1*(3), 16-19.

Ibrahim, M., & Umar, A. (2016). Adsorption thermodynamics of some basic dyes uptake from aqueous solution using Albizia lebbeck shells. *Chemsearch Journal, 7*(1), 43-51.

Jain, M., Garg, V. K., & Kadirvelu, K. (2010). Adsorption of hexavalent chromium from aqueous medium onto carbonaceous adsorbents prepared from waste biomass. *Journal of environmental management, 91*, 949–957.

Karnitz Jr, O., Gurgel, L. V. A., De Melo, J. C. P., Botaro, V. R., Melo, T. M. S., de Freitas Gil, R. P., & Gil, L. F. (2007). Adsorption of heavy metal ion from aqueous single metal solution by chemically modified sugarcane bagasse. *Bioresource Technology, 98*(6), 1291-1297.

Kumar, P. S., & Saravanan, A. (2018). Environmental Detoxification Using Carbonaceous Composites. *Carbonaceous Composite Materials, 42*, 205-230.

Liu, Z., Sun, Y., Xu, X., Qu, J., & Qu, B. (2020). Adsorption of Hg (II) in an aqueous solution by activated carbon prepared from rice husk using KOH activation. *ACS omega, 5*(45), 29231-29242.

Mohamed, F., & Alfalous, K. (2020). The effectiveness of activated silica derived from rice husk in coagulation process compared with inorganic coagulants for wastewater treatment. *The Egyptian Journal of Aquatic Research, 46*(2), 131-136.

Moosa, M., A., , Ridha, A. A., M., A., & Abdullha, I. N. (2015). Chromium Ions Removal from Wastewater Using Carbon Nanotubes Chromium Ions Removal from Wastewater Using Carbon Nanotubes. (March). *Research gate*, 1-7.

Muhammad, A., Rakhshan, K., Ikhtiar, K., & Asma, S. (2015). Effect of Heavy Metals from Tannery Effluent on the Soil and Groundwater using Multivariate Analysis in District Sheikhupura, Pakistan. 1-10.

Mustapha, S., Ndamitso, M., Abdulkareem, A., Tijani, J., Mohammed, A., & Shuaib, D. (2019). Potential of using kaolin as a natural adsorbent for the removal of pollutants from tannery wastewater. *Heliyon, 5*(11), e02923.

Nayl, A. E. A., Elkhashab, R. A., Malah, T. E., Yakout, S. M., El-Khateeb, M. A., Ali, M. M. S., & Ali, H. M. (2017). Adsorption studies on the removal of COD and BOD from treated sewage using activated carbon prepared from date palm waste. *Environment Science Pollution Resources*, 1-10.

Okeola, O., Odebunmi, E., & Ameen, O. (2012). Comparison of sorption capacity and surface area of activated carbon prepared from Jatropha curcas fruit pericarp and seed coat. *Bulletin of the Chemical Society of Ethiopia, 26*(2).

Olufemi, A. S. (2018). Agricultural Waste Adsorbents for Heavy Metals Removal from Wastewater Agricultural Waste Adsorbents for Heavy Metals Removal from Wastewater., 1-7.

Opeolu, B. O. (2009). Utilization of maize (Zea mays) cob as an adsorbent for lead (II) removal from aqueous solutions and industrial effluents. *African Journal of Biotechnology, 8*(8).

Owa, F. (2013). Water pollution: sources, effects, control and management. Department of Integrated Science, Federal College of Education, Okene, Kogi State, Nigeria. *Mediterr J Soc Sci MCSER Publishing, Rome-Italy, 4*(8).

Özer, A. (2007). Removal of Pb (II) ions from aqueous solutions by sulphuric acid-treated wheat bran. *Journal of Hazardous Materials, 141*(3), 753-761.

Parlayici, S., Eskizeybek, V., Avcı, A., & Pehlivan, E. (2015). Removal of chromium (VI) using activated carbon-supported-functionalized carbon nanotubes. *Journal of Nanostructure in Chemistry, 5*(3), 255-263.

Ullah, M., Nazir, R., Khan, M., Khan, W., Shah, M., Afridi, S. G., & Zada, A. (2019). The effective removal of heavy metals from water by activated carbon adsorbents of Albizia lebbeck and Melia azedarach seed shells. *Soil and Water Research, 15*(1), 30-37.

Yan, K., & Wang, Q. (2018). *Adsorption characteristics of the silica gels as adsorbent for gasoline vapors removal.* Paper presented at the IOP Conference Series: Earth and Environmental Science.

JOURNAL OF THE NIGERIAN SOCIETY OF CHEMICAL ENGINEERS INSTRUCTION TO AUTHORS

1. TYPES OF PUBLICATION

The Journal of the Nigerian Society of Chemical Engineers will publish articles on the original research on the science and technology of Chemical Engineering. Preference will be given to articles on new processes or innovative adaptation of existing processes. Critical reviews on current topics of Chemical Engineering are encouraged and may be solicited by the Editorial Board. The following types of articles will be considered for publication:

a. Full length **articles or review papers**.
b. **Communication** – a preliminary report on research findings.
c. **Note** – a short paper describing a research finding not sufficiently completed to warrant a full article.
d. **Letter to the Editor** – comments or remarks by readers and/or authors on previously published materials.

The authors are entirely responsible for the accuracy of data and statements. It is also the responsibility of authors to seek ethical clearance and written permission from persons or agencies concerned, whenever copyrighted material is used.

For now the journal is published twice in a year, March/April and September/October.

2. MANUSCRIPT REQUIREMENTS

a. The **Manuscript** should be written in clear and concise English and typed (single column) in Microsoft Word using double spacing on A4-size paper, Times New Romans font and 12 point. A full length article or review should not exceed 15 pages. Margin should be Normal (i.e. 2.54cm for Top, Bottom, Left & Right margins).
b. The **Manuscript** should be prepared in the following format: Abstract, Introduction, Materials and Methods, Results, Discussion, Conclusion, Acknowledgements, and References..
c. The **Manuscript** must contain the full names, address and emails of the authors. In the case of multiple authorship, the person to whom correspondence should be addressed must be indicated with functional email address. As an examples, authors' names should be in this format:
   Momoh, S. O., Adisa, A. A. and **Abubakar, A. S.**
   If the addresses of authors are different, use the following format:
   ***Momoh, S. O.[1], Adisa, A. A.[2]** and **Abubakar, A. S.[3]**
   Use star * to indicate the corresponding author.
d. **Symbols** should conform to America Standard Association. An abridged set of acceptable symbols is available in the fourth edition of Perry's Chemical Engineering Handbook. Greek letters, subscripts and superscripts should be carefully typed. A list of all symbols used in the paper should be included after the main text as **Nomenclature**.
e. All **Units** must be in the SI units (kg, m, s, N, etc).
f. The **Abstract** should be in English and should not be more than 200 words. The Abstract should state briefly the purpose of the research, methodology, results, major findings and major conclusions. Abstracts are not required for Communications, Notes or Letters.
g. **Citation** must be in the Harvard Format i.e. (Author, Date). Examples are (Smith, 1990) or (Jones et al, 2011). (Kemp, 2000) demonstrated that …..; (Mbuk, 1985; Boma, 1999; Sani, 2000) if more than two authors. (Telma, 2001a), (Telma, 2001b); etc if the citation have the same author and year of publication.

For more information on Harvard Referencing: Guide visit http://www.citethisforme.com/harvard-referencing

h. **References** must also be in the Harvard Format i.e. (Author, Date, Title, Publication Information). References are listed in alphabetical order. Examples are shown below:
   Haghi, A. K. and Ghanadzadeh, H. (2005). A Study of Thermal Drying Process. *Indian Journal of Chemical Technology*, Vol. 12, November 2005, pp. 654-663
   Kemp, I.C., Fyhr, C. B., Laurent, S., Roques, M. A., Groenewold, C. E., Tsotsas, E., Sereno, A. A., Bonazzi, C. B., Bimbernet, J. J. and Kind M.(2001). Methods for Processing Experimental Drying Kinetic Data. *Drying Technology,* 19: 15-34.
i. **Tables** should contain a minimum of descriptive materials. Tables should be numbered serially throughout the manuscript in Arabic numerals (1, 2, 3, etc), and should be placed at the referenced point with captions (centralised) placed at the top of the table.
j. **Figures**, charts, graphs and all illustrations should be placed at the referenced point, numbered serially throughout the manuscript in Arabic numerals (1, 2, 3, etc) and incorporated in the text. Caption for Figures should be placed at the bottom of the Figure (centralised). Lettering set or symbols should be used for all labels on the figures, graphs, charts, photographs even when drawn in colours. (Note that

figures drawn in colours may be unreadable if printed in black and white).

k. **Equations** should be typed using MS Word Equation Editor and should be centred and numbered serially throughout the manuscript (in Arabic numeral) at the right margin.
l. Wherever possible, **Fractions** should be shown using the oblique slash. E.g. x/y
m. **Footnotes** should not be incorporated in the text.
n. **Acknowledgements** should appear at the end of the paper, before the list of references.

3. SUBMISSION OF MANUSCRIPTS

Manuscripts should be submitted by sending a Microsoft Word document (taking into account the Manuscript Requirements described in section 2 above) to the following email address: nschejournal@yahoo.com and copy stevmomoh@yahoo.com**.**

All correspondences are directed to the Editor-in-Chief using the submission emails addresses: nschejournal@yahoo.com and copy stevmomoh@yahoo.com. Meanwhile the online submission of articles on the journal website will soon be ready.

Authors should note that:

a. All authors listed in the manuscript have significantly contributed to the research.
b. All authors are obliged to provide retractions or corrections of mistakes.
c. All references cited are listed and financial support acknowledged.
d. It is forbidden to publish same research in more than one journal.

The fee charged for paper review and publication will be borne by the authors as follows:

a. Manuscript Review charges = N6,500 payable by both Members and Non-Member. Overseas is $30.00.
b. Publication Charges = N10,000 payable by Non-Members and Members who are not financially up-to-date. Overseas is $40.00.
c. Members would only get one (1) Journal free and buy the other if they so wish.
d. Corresponding Author whose paper is published on a particular edition would get one (1) free copy on behalf of all the co-authors. Other co-authors will buy if they so wish.

All fees are paid after the paper had been accepted for publication. These charges may be reviewed from time to time by the Governing Board of Directors of the Society.

4. ACCEPTED PAPERS

On acceptance, authors will be required to submit a copy of their manuscripts using Microsoft Word by emails to nschejournal@yahoo.com and copy stevmomoh@yahoo.com.

The following additional information should be observed for accepted papers: (i) Typed in Microsoft Word using 1.15 spacing on A4-size paper, Times New Romans font and 10 point; (ii) Margin should be 2.54cm for Top & Bottom; 2.20cm for Left & Right margins; (iii) The abstract should be one column document while the body of the manuscript should be double columns with 0.5cm gutter spacing except some tables and figures that may have to go in for one column document.

5. PUBLICATION

Full NSChE Journal edition in hard copy will be published twice annually – March/April Edition and September/October Edition.

6. REPRINT

Reprints are available on request at a moderate fee per page. Orders must be placed before the paper appears in Print.

7. READER'S INFORMATION

The papers are wholly the view of their author(s) and therefore the publisher and the editors bear no responsibility for such views.

8. SUBSCRIPTION INFORMATION

The subscription price per volume is as follows:

a. Individual Reader - N3,000.00
b. Institutions, Libraries, etc.- N5,000.00
c. Overseas Subscription - $100.00

Request for information or subscription should be sent to the Editor-in-Chief through the following emails addresses: nschejournal@yahoo.com and copy stevmomoh@yahoo.com.

9. COPYRIGHT NOTICE

By submitting your manuscript to the Journal, you have agreed that the copyright of the published material belongs to the journal.

10. PRIVACY STATEMENT

The names and email addresses entered in this journal site will be used exclusively for the stated purposes of this journal and will not be made available for any other purpose or to any other party.